INFORMATION TO USERS

This manuscript has been reproduced from the microfilm master. UMI films the text directly from the original or copy submitted. Thus, some thesis and dissertation copies are in typewriter face, while others may be from any type of computer printer.

The quality of this reproduction is dependent upon the quality of the copy submitted. Broken or indistinct print, colored or poor quality illustrations and photographs, print bleedthrough, substandard margins, and improper alignment can adversely affect reproduction.

In the unlikely event that the author did not send UMI a complete manuscript and there are missing pages, these will be noted. Also, if unauthorized copyright material had to be removed, a note will indicate the deletion.

Oversize materials (e.g., maps, drawings, charts) are reproduced by sectioning the original, beginning at the upper left-hand corner and continuing from left to right in equal sections with small overlaps.

ProQuest Information and Learning
300 North Zeeb Road, Ann Arbor, MI 48106-1346 USA
800-521-0600

DISSERTATION

PHOTOELECTROCHEMICAL ETCHING AND DYE SENSITIZATION OF BRIDGMAN GROWN SINGLE CRYSTAL SnS_2 PHOTOANODES

Submitted by

Laura Inman Sharp

Department of Chemistry

In partial fulfillment of the requirements

For the Degree of Doctor of Philosophy

Colorado State University

Fort Collins, Colorado

Fall 2002

UMI Number: 3075383

UMI Microform 3075383

ProQuest Information and Learning Company
300 North Zeeb Road
P.O. Box 1346
Ann Arbor, MI 48106-1346

COLORADO STATE UNIVERSITY

October 21, 2002

WE HEREBY RECOMMEND THAT THE DISSERTATION PREPARED UNDER OUR SUPERVISION BY LAURA INMAN SHARP ENTITLED PHOTOELECTROCHEMICAL ETCHING AND DYE SENSITIZATION OF BRIDGMAN GROWN SINGLE CRYSTAL SnS_2 PHOTOANODES BE ACCEPTED AS FULFILLING IN PART THE REQUIREMENTS FOR THE DEGREE OF DOCTOR OF PHILOSOPHY.

Committee on Graduate Work

Adviser

Department Head

ABSTRACT OF DISSERTATION

PHOTOELECTROCHEMICAL ETCHING AND DYE SENSITIZATION OF BRIDGMAN GROWN SINGLE CRYSTAL SnS_2 PHOTOANODES

The growth of n-type single crystal SnS_2 with various carrier concentrations and different dopant elements has been accomplished. The electronic properties of these crystals were determined through Hall and Mott-Schottky measurements. These measurements showed that the carrier concentration was uniform throughout the middle section of the crystals. Analysis of the photocurrent data revealed that a direct correlation exists between the carrier concentration, the minority carrier concentration and the band-gap incident photon to current efficiency (IPCE).

Dye sensitization of SnS_2 with methylene blue (MB^+), azure B (AZB^+), oxazine (OX^+) and cresyl violet (CV^+) has been studied. Higher dye sensitized IPCE's for MB^+ and CV^+ were obtained near step edges and defects on the crystal surface due to intercalation of dye molecules into exfoliated areas of the crystal. Langmuir analysis of the MB^+ adsorption data on a smooth surface indicated that the dye molecules were lying flat on the surface. Photoxidation studies with

MB^+ and CV^+ showed that these dyes exhibited both different excited state properties and distinct adsorption behavior with CV^+ displaying significantly faster rates of adsorption and desorption. Analysis of the MB^+, AZB^+, CV^+ and OX^+ IPCE's showed that the IPCE values for these dyes were unaffected by the SnS_2 carrier concentration. Impedance measurements and quantum measurements from both photoaction spectra and photocurrent-voltage curves indicated that recombination appeared to influence the dye sensitization process. The identity of the recombination centers was probed by thiol addition and annealing SnS_2 crystals in S vapor to change the S content of the surface.

Photoelectrochemical (PEC) studies showed that an increased IPCE was associated with roughening the SnS_2 surface. An optimum degree of PEC etching for SnS_2 electrodes was observed in regards to the dye sensitized IPCE, the band gap IPCE and their ratio. The relationship between the MB^+ sensitized IPCE and the extent of photoetching showed a dependence on the SnS_2 carrier concentration. Analysis of the MB^+ adsorption isotherm showed that PEC etching also appeared to influence the binding strength of the dye as the heat of adsorption was slightly greater for MB^+ on photoetched versus unetched SnS_2.

Laura Inman Sharp
Department of Chemistry
Colorado State University
Fort Collins, CO 80523
Fall 2002

ACKNOWLEDGMENTS

I would like to acknowledge the members of the Parkinson group and my adviser Dr. Parkinson, for their help throughout my graduate career. All the CSU faculty who aided my research, in particular Chuck Martin and Peter Dorhout. Special thanks to Nancy Levinger and Ellen Fisher for their personal encouragement and professional insights. A BIG thank you to all my friends, I wouldn't have made it without you! I also need to thank my mother for the many hours she spent chasing Emma while I was working on my dissertation and both my parents for their unending support. Finally, François for his patience and understanding.

DEDICATION

To my dad and his father.

TABLE OF CONTENTS

LIST OF TABLES

LIST OF FIGURES

CHAPTER 1

Principles of Semiconductor Photoelectrochemistry

INTRODUCTION

Scientific efforts in solar energy conversion have grown as the world's supply of cheap fuel has diminished. Using the sun as an alternative energy resource has the added benefit of producing no side products unlike automobile engines and coal-fired power plants that generate oxides of sulfur and nitrogen in great abundance. In nature, photosynthesis is the process by which sunlight is converted to energy. Although the theoretical efficiency of plants is 6.6%, the typical conversion efficiencies are only 0.3-3% depending on the vegetation.[1] Photovoltaic devices produced to convert solar energy into electrical energy have higher conversion efficiencies; silicon solar cells are 20-24% and tandem GaInP/GaAs cells achieve roughly 30% conversion efficiency. Recent advances in photoelectrochemical cells have led to solar energy conversion efficiencies of greater than 10% for cells comprised of ruthenium complexes adsorbed to high surface area nanocrystalline TiO_2 films.[2] These cells, developed by Grätzel and coworkers[3] in 1988, are based on the dye sensitization process and are less expensive to produce than photovoltaic cells.

The field of photoelectrochemistry was discovered in 1839 by Edmund Becquerel.[4] He observed the photovoltaic effect when electricity was generated upon illuminating an AgCl electrode in an electrochemical cell. Over a century passed before further achievements were made in photoelectrochemistry. In 1954, Brattain and Garrett at Bell Laboratories showed that chemical reactions at a Ge electrode could be affected by controlling the semiconducting properties of the electrode or by exposing it to light.[5] This work was followed up by photoelectrochemical studies on materials such as Si, CdS, ZnS, CdSe, ZnSe, ZnTe, GaAs, GaP, ZnO, $KTaO_3$, Ta_2O_5, $SrTiO_3$ and TiO_2.[6-13] From these studies a fundamental understanding of the semiconductor-electrolyte interface was established. This led to the discovery that photoelectrochemical energy conversion cells have the ability to convert solar radiation to either electricity or chemical fuel in the form of redox products. These cells rely on a semiconductor electrode that absorbs light. It is the semiconductor-liquid interface, however, that enables solar energy conversion to be possible.

In the early 1970s practical applications of semiconductor photoeffects were realized by Fujishima and Honda.[14,15] They electrolyzed H_2O to H_2 and O_2 in an electrochemical cell with two electrodes, one Pt and one TiO_2 that was irradiated with UV light. The photoelectrolysis of water converted energy in sunlight to stored chemical energy. Because this discovery coincided with public awareness of the world oil crisis in 1973, there were increased efforts to produce an alternative energy source.

Scientists soon discovered that no known semiconductor material provided all the necessary properties to produce efficient photoelectrolysis of water in solar energy conversion. Large band gap semiconductors were initially employed as they had the benefit of being more stable to corrosion than small band gap semiconductors. However, an ideal semiconductor should have an optimum band gap for light absorption of 1.5 to 2.0 eV, a conduction band edge that is more negative than the reduction potential of H_2O, a valence band edge that is more positive than the oxidation potential of H_2O, rapid charge transfer kinetics at the semiconductor-electrolyte interface, and resistance to corrosion.[16] Because these requirements are difficult to fulfill, the electrolysis of water has not been exploited industrially.

Other systems designed for solar energy conversion at this time were electrochemical photovoltaic cells. Instead of splitting water, electrons were driven through an external circuit, converting optical energy to electrical energy. One adaptation of this system was the incorporation of a dye molecule adsorbed to the semiconductor surface to increase spectral sensitivity and material stability.

Recent advances in photoelectrochemical solar energy conversion have been realized with porous nanocrystalline films. Hodes and coworkers[17] were able to electrodeposit and chemically deposit CdS and CdSe nanoparticles on conductive glass, while Grätzel and coworkers[2] have developed a technique of coating similar surfaces with anatase TiO_2 nanoparticles. Alternatively, single

crystal dichalcogenides that are photoetched have micron sized pores and demonstrate high quantum efficiency.[18] These systems can be studied to further understand the fundamental processes of electron transfer at the semiconductor-electrolyte interface as well as to gain a more complete understanding of solar energy conversion.

The remainder of this chapter provides the reader with a basic knowledge of semiconductor photoelectrochemistry. First, there will be a brief description of band theory and semiconducting materials. Second, electron transfer and dye sensitization processes will be discussed. The chapter ends with a brief history of the field of dye sensitization leading to its current state.

Band Theory. Semiconductor materials are comprised of bands that are created by the overlap of a large number of atomic orbitals that combine to form a virtually continuous band of closely spaced orbitals. The highest occupied (valence) band is separated from the lowest unoccupied (conduction) band by a distinct energy gap (E_g) commonly referred to as the band gap. This differs from metals that do not have an energy gap separating the highest occupied and lowest unoccupied energy levels. The chemical nature of the valence and conduction bands are typically attributed to the orbitals of which they are comprised. The "common anion rule"[19] predicts that for semiconductors, the valence band consists primarily of atomic orbitals from lattice anions while the conduction band is from lattice cations.

Semiconductor materials are further characterized by their conductivity

that increases with increasing temperature. Contrasting behavior exists for metals that exhibit a decrease in conductivity with increasing temperature. The correlation between conductivity and temperature observed for semiconductors is predicted by the Fermi-Dirac distribution:

$$f(E) = \left\{1 + \exp\left[\frac{(E - E_F)}{kT}\right]\right\}^{-1} \qquad (1.1)$$

where $f(E)$ gives the fraction of allowed levels with energy E, and the Fermi level, E_F, is the energy level where the probability of finding an electron is one half.

The conductivity of semiconductors increases when either negative charge carriers are generated in the conduction band or positive charge carriers in the valence band. This occurs as a result of three process: thermal excitation, photoexcitation, or doping. Thermal excitation affects only semiconductors with small band gaps as the average thermal energy at room temperature is only 0.026 eV (~kT) and band gaps commonly range from 0.3 to 3 eV. Photoexcitation occurs when the semiconductor absorbs light equal to or greater than the band gap while doping relates to the introduction of new energy levels in the band gap of the semiconductor.

Of the three processes mentioned, doping allows the conductivity of a semiconductor to be increased by altering the physical properties of the material. This is achieved by introducing elements with a greater number of charge carriers (holes or electrons) relative to the semiconductor lattice. Dopants are

chosen such that shallow impurity bands form near either the conduction band or valence band edge. These bands are oxidized in n-type semiconductors, generating electrons in the conduction band, and reduced in p-type semiconductors, creating holes in the valence band. The deeper the impurity levels, the more difficult they are to oxidize or reduce and the less conductive the semiconductor.

In addition, doping affects the energy of the Fermi level, raising it with n-dopants and lowering it with p-dopants. Intrinsic semiconductors, that have not been intentionally doped, have carrier concentrations in the range of 10^{10} - 10^{13} cm^{-3}. Doped semiconductors, on the other hand, have carrier concentrations between 10^{13}-10^{18} cm^{-3} and therefore are more conductive.

A complete characterization of semiconducting materials requires electrical properties, such as conductivity and doping density, as well as optical properties to be measured. Optical properties are derived from energy band diagrams and dictate the values of both the absorption coefficient and the band gap of the semiconductor. The absorption coefficient per unit length α is given by:

$$\alpha \equiv (4\pi k)/\lambda \qquad (1.2)$$

where k is the absorption constant and λ the wavelength of interest.[20] These values are affected by whether the electronic band to band transition is optically and spin allowed (direct) or optically forbidden (indirect). Semiconductors with direct transitions have large absorption coefficients (~10^{4}-10^{5} cm^{-1}) near their

band edge while indirect transitions are typically weaker absorbers ($\alpha \approx 10^2\ cm^{-1}$). Thus, the optical penetration depth is much greater for semiconductors with indirect transitions and thicker samples must be utilized to maximize incident light absorption.

The second primary feature defining optical properties is the band gap of the semiconductor or the absorption threshold. Because semiconductors can absorb all photons of energy equal to or greater than their band gap, the absorption threshold is the energy level above which all photons are absorbed. Figure 1.1 diagrams the power distribution of the solar spectrum vs. photon wavelength. Referring to this diagram, semiconductors with band gaps less than or equal to 1 eV are ideal for maximum solar energy conversion as they can absorb 80% of the sunlight. However, because the photovoltage generated from a solar cell is proportional to the band gap of the semiconductor used, small band gap materials are relatively ineffective at converting sunlight to electrical power. Large band gap materials are equally inefficient as they can only harvest light that is greater than or equal to their threshold energy which eliminates a major portions of the solar spectrum. As will be seen later, various methods have been devised to address this disparity.

Semiconducting Materials. When discussing electron transfer and dye sensitization processes it is important to consider the various crystal structures of semiconducting materials as they influence semiconductor characteristics. Semiconductor materials comprise a large group of inorganic solids. The most

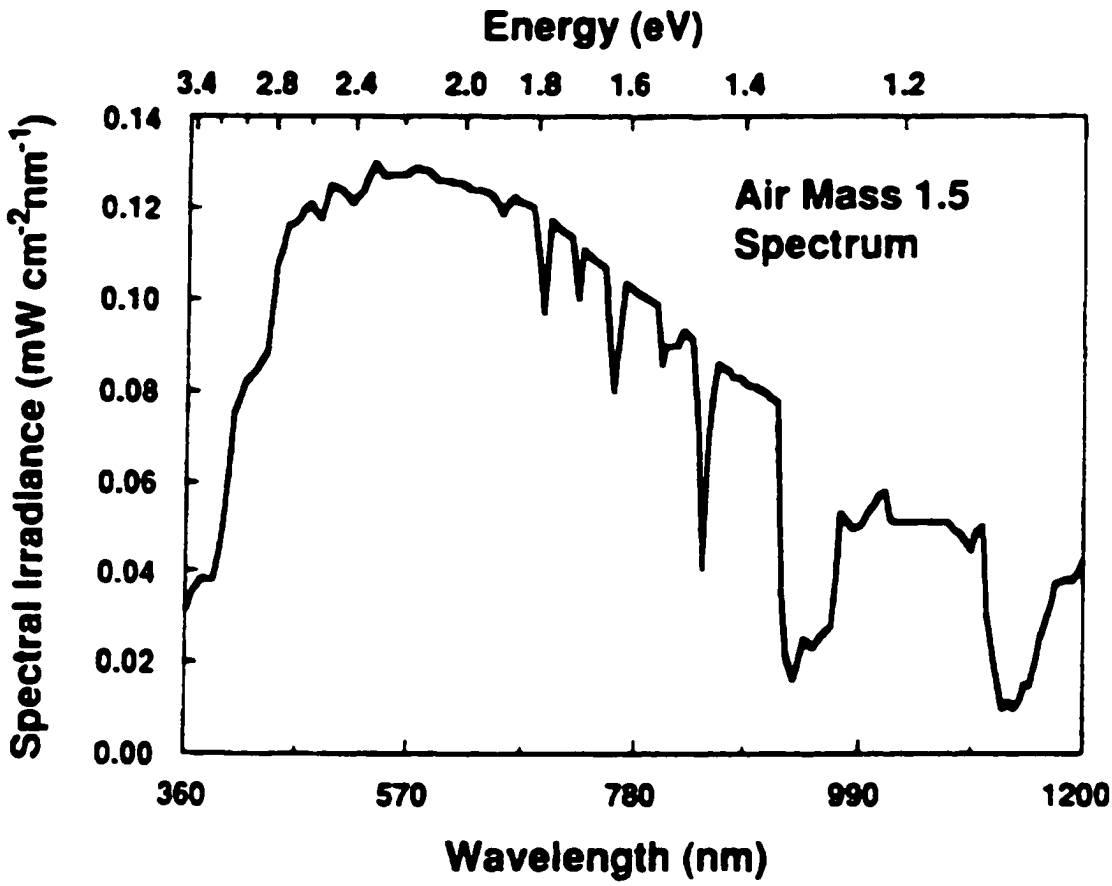

Figure 1.1. Solar spectral irradiance adapted from reference 22.

common crystals structures are cubic diamond, zinc blende, and wurtzite. These three structures belong to a group of materials known as the adamantine solids. All the structures in this group have four valence electrons per atom. Two major classes of semiconductors that do not fall into this group are the metal oxides and metal dichalcogenides. Many members of this later class of semiconductors adopt a layered structure with metal atoms "sandwiched" between two layers of chalcogenides. Consecutive "sandwich" layers are held together by van der Waal forces.

From the previous discussion it is apparent that characterizing electrical and optical properties of semiconductors is essential to studying semiconductor processes. Both the band gap and absorption coefficient can be determined from UV-Vis spectroscopy measurements. Conductivity and doping density can be calculated from Hall measurements. Mott-Schottky studies yield doping density and the flat band potential, which is defined in the following section, through the Mott-Schottky relationship:

$$\frac{1}{C_{SC}^2} = \frac{2(V_M - V_{FB})}{\varepsilon\varepsilon_0 q N_D A^2} \tag{1.3}$$

where C_{SC} is the capacitance, A the area, N_D the doping density, ε the dielectric constant, ε_0 permittivity and V_{FB} and V_M the flat band and applied potential, respectively. The thickness of the depletion layer (W), a parameter that will be discussed in the following section, can be derived from the capacitance as $W=\varepsilon_0 \varepsilon/C_{sc}$. In order for meaningful numbers to be obtained, Mott-Schottky

plots, the inverse capacitance squared ($1/C^2$) vs potential (V) must be linear and frequency independent. Finally, other techniques such as current-potential curves and photovoltage measurements reveal information on the flat band potential and band edges. However, these last two techniques are less reliable due to band edge movement and recombination effects.

Semiconductor Electrolyte Junction. Investigating electron transfer reactions at the semiconductor-electrolyte interface is essential to the study of dye sensitization. A fundamental understanding of interfacial energetics is required to analyze the electron transfer reactions in photoelectrochemical systems. Electron transfer at the semiconductor-electrolyte interface can be compared to similar processes at the metal-electrolyte interface. A major difference is that electron transfer can occur from (or into) two different energy levels; either from the conduction or valence band to the electrolyte or from the electrolyte into either band. While this process occurs only from (or into) a single energy level in metal electrodes because there is no band gap.

The basic model for electron transfer at semiconductor electrodes is based on the Gerischer model.[21] This model is depicted in Figure 1.2 showing electron energy distribution for n-type and p-type semiconductors. In the diagram E_{CB}, E_{VB} and E_F are the energies of the conduction band, valence band and the Fermi level, respectively. Figure 1.2 shows both semiconductors at their flat band potential. This is the unique potential for which the potential drop between the surface and the bulk of the electrode is zero; there is no electric field in the

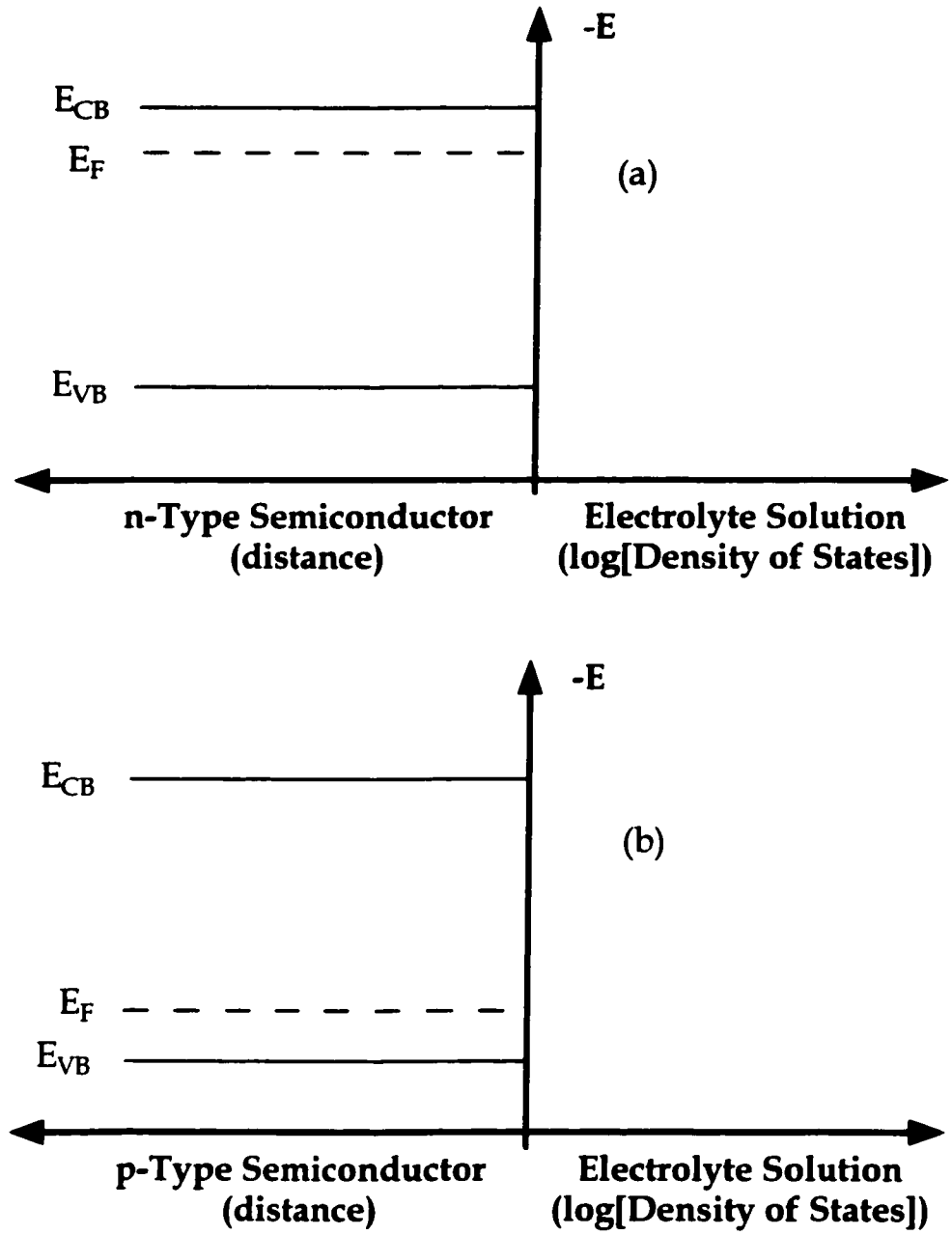

Figure 1.2. Semiconductor energy vs. position diagrams. The y-axis is energy in eVs with electron energy up and hole energy down. The x-axis is the log[Density of States] in the positive direction and distance in the negative direction. E_{CB}, E_{VB} and E_F are the energies of the conduction band, valence band and the Fermi level, respectively. (a) n-type semiconductor and (b) p-type semiconductor both at the flat band potential.

semiconductor.

In this model, an equilibrium state is reached upon contact of the semiconductor with an electrolyte solution containing a redox species. Prior to this stage, the E_{VB}, E_{CB} and E_F are constant throughout the semiconductor both at the surface and in the bulk. Once the semiconductor encounters the electrolyte solution, charge flow occurs between the solid and liquid phase in order to reach equilibrium. The direction of the charge flow depends on the relative ordering of the chemical potential of the redox species in solution and the Fermi level of the semiconductor. For example, in Figure 1.3 an n-type semiconductor is in contact with a redox couple having a standard electromotive force (emf) for its half reaction, E°, more positive than the semiconductor potential (E_F); thus, electron flow occurs from the semiconductor to the solution. Charges flow until the electrochemical potentials of the semiconductor and the redox couple are equal, when the system reaches thermodynamic equilibrium. This creates a depletion of electrons at the surface of the semiconductor that is depicted by curved or "bent" energy levels for the conduction band, valence band, and Fermi level, hence the term band bending. Due to the depletion of negative charges at the surface of the semiconductor, an electric field is generated in this region with the maximum electric field strength located at the semiconductor-electrolyte interface. This corresponds to negative electric potentials as the electric potential is equal to the negative integral of the electric field strength.[22] Another way of describing the band bending in Figure 1.3 is that the upward bend indicates the

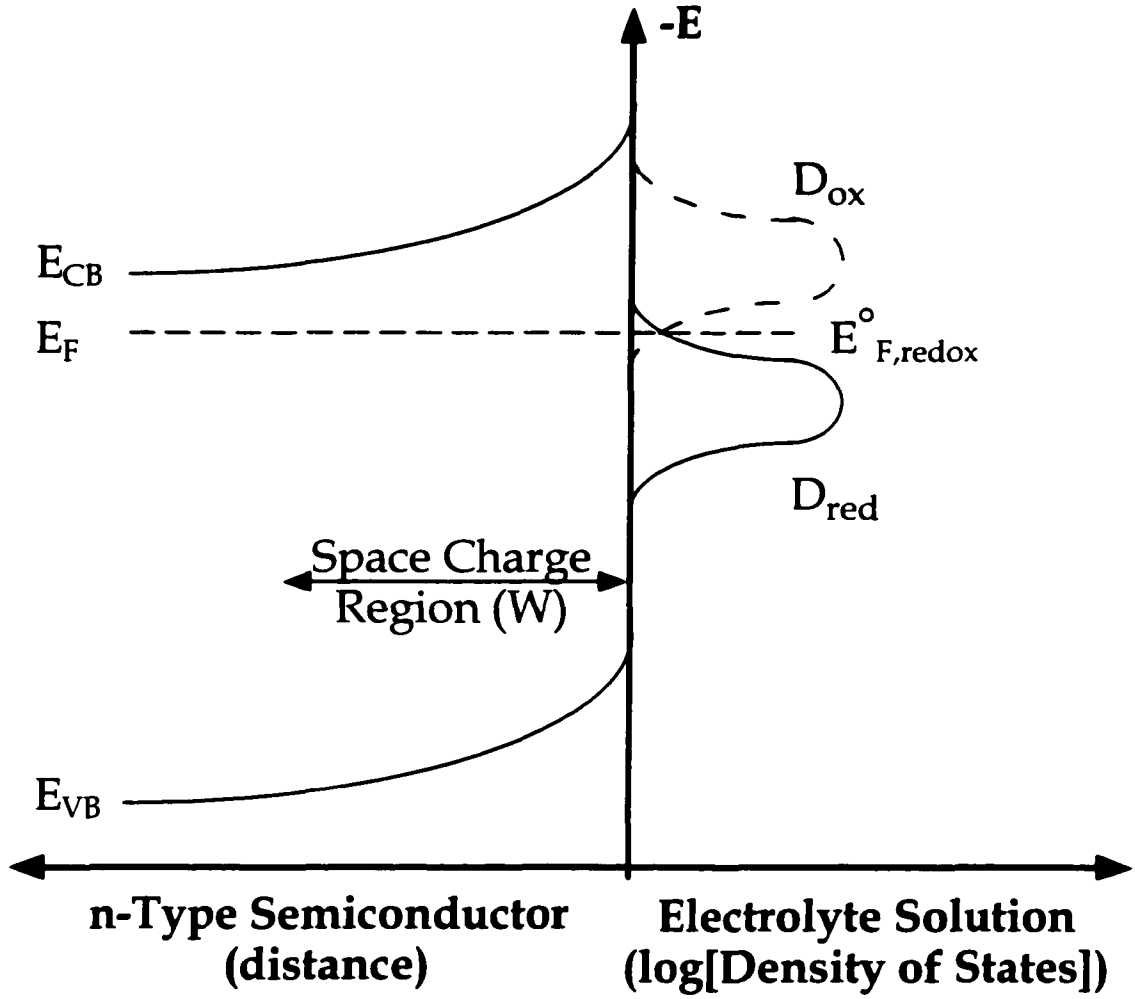

Figure 1.3. An n-type semiconductor electrode in an electrolyte solution at equilibrium in the dark. Where D_{ox} is the energy distribution for oxidized redox molecules, D_{red} is the energy distribution for reduced redox molecules and $E^{\circ}_{F,\ redox}$ is the solution redox potential.

potential barrier that an electron in the conduction band must overcome to escape into the solution.

When a semiconductor electrode is placed in contact with an electrolyte solution an electrical double layer is formed on the solution side and an electric field is generated at the semiconductor surface. Upon the introduction of a redox species in solution, both the Fermi level in the semiconductor and the solution redox potential, E^*, could move in order for the system to reach equilibrium. However, as seen in Figure 1.3, band bending is seen only on the semiconductor side of the interface. This is due to the difference in capacitance between the electrolyte solution (C_{dl}) and the semiconductor (C_{sc}). Since the density of electronic states in the solution is greater than in the semiconductor, it follows that C_{dl} is greater than C_{sc}. Because capacitance in series adds as the reciprocal, the semiconductor that has the smaller capacitance also has the major portion of the potential drop occur near its surface. This is apparent from Equation 1.4:

$$\frac{1}{C_{Total}} = \frac{1}{C_{sc}} + \frac{1}{C_{dl}} \tag{1.4}$$

Therefore, the greater potential drop occurs across the semiconductor as portrayed in Figure 1.3.

The generation of an electric field at the semiconductor surface allows charge separation to be possible and, as such, is of the utmost importance in energy conversion processes. Because the depth of the depletion or space charge region (W), as indicated in Figure 1.3, depends upon the doping density (N_D for

an n-type semiconductor), the magnitude of the electric field gradient can be controlled by modification of the doping level. An increase in the doping density corresponds to a decrease in the width of the depletion region.

Electron transfer events occur at this semiconductor-electrolyte interface that is described by the Gerischer model. The theory of electron transfer reactions is based on the Frank Condon principle. Therefore, the assumption is that electron transfer occurs rapidly compared to the time scale for molecular motion. Figure 1.4 describes four separate cases for electron transfer processes in the dark at both p- and n-type semiconductors. Current flow is induced in all cases by applying an external bias to the semiconductor electrodes. As a reminder, majority carriers are electrons for n-type semiconductors and holes for p-type semiconductors. In Figure 1.4 (a and d) the semiconductor electrodes are under a forward bias that reduces the band bending and increases the transfer of majority carriers. Under forward bias, the Fermi level shifts to more negative potentials for n-type semiconductors and to more positive potentials for p-type semiconductors. When semiconductor electrodes are under reverse bias, Figure 1.4 (b and c), the band bending increases and there is a reduction in the majority carriers available for charge transfer.

Two key factors influencing charge transfer reactions are orbital overlap between the redox species and the bands of the semiconductor, and the applied bias. The equation relating current and voltage for a non-illuminated semiconductor electrolyte junction is as follows:

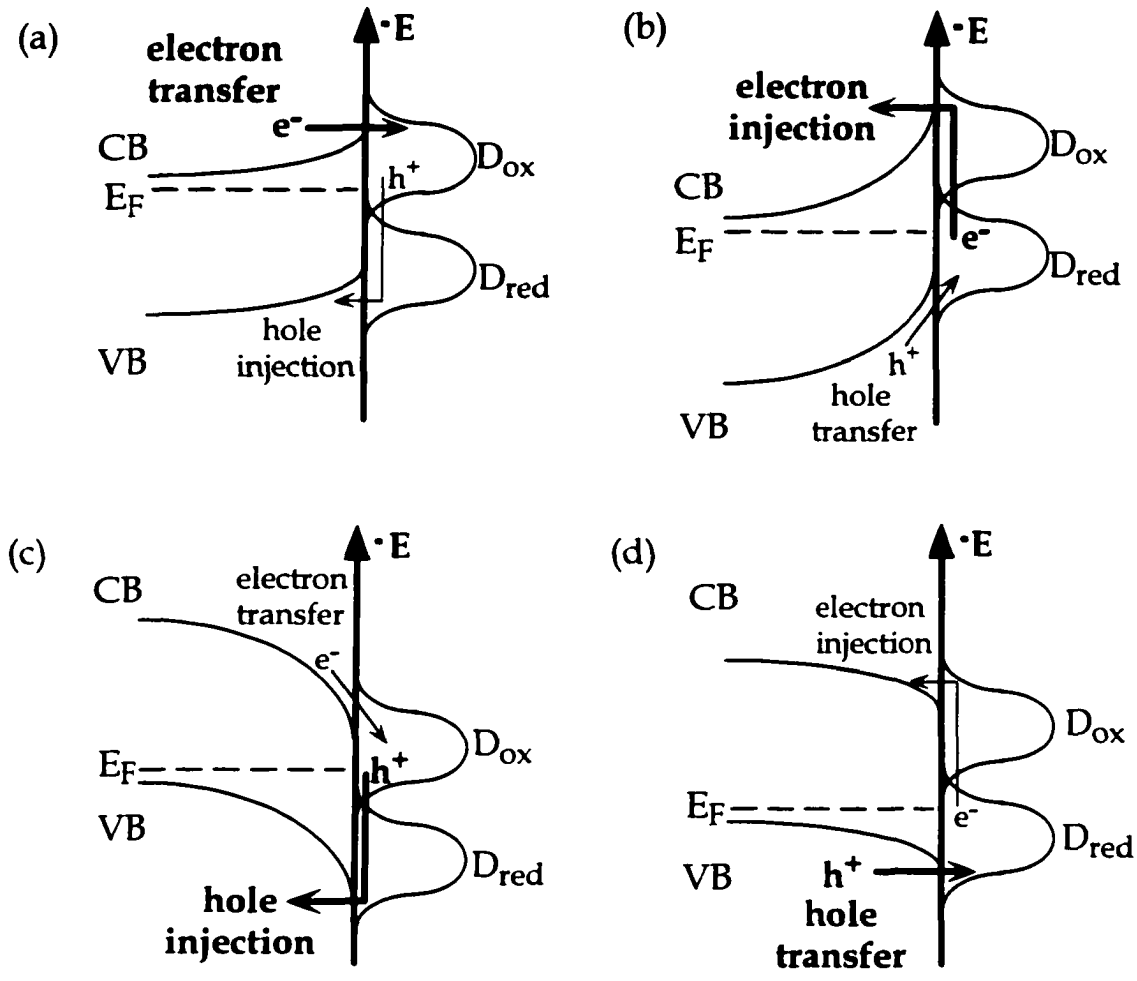

Figure 1.4. n-type (a) reduction, forward bias and (b) oxidation, reverse bias. p-type (c) reduction, reverse bias and (d) oxidation, forward bias. Arrows show majority (in bold) and minority carriers.

$$I = -I_0\left[\exp\left(-\frac{qV}{kT}\right) - 1\right] \tag{1.5}$$

where I_0 is the equilibrium exchange current, q is the charge of an electron, k the Boltzmann constant, T the temperature and V the applied voltage. In addition, the output current, I, is affected by the overlap of the semiconductor bands and the redox orbitals. Charge transfers involving large band gap semiconductors are usually dominated by the band, conduction or valence, that overlaps with the redox species orbitals, while small band gap semiconductors are not under such constraints.

When the semiconductor-electrolyte interface is under illumination, a different situation arises, as illustrated in Figure 1.5. Electron-hole pairs are generated in the space charge region and the current flow at the semiconductor electrolyte interface is dominated by photogenerated minority carriers (I_{PH}). The current is given by:

$$I = I_{PH} - I_0\left[\exp\left(-\frac{qV}{kT}\right) - 1\right] \tag{1.6}$$

An anodic current flows for n-type semiconductors as minority carriers (holes) oxidize the reduced form of the redox species. The reverse scenario exists for p-type semiconductors. If an external bias were applied to the semiconductor electrode, there would be similar effects as discussed earlier and depicted in Figure 1.4.

Other important aspects of illumination are the dependence of photovoltage and photocurrent on the absorption threshold. These provide

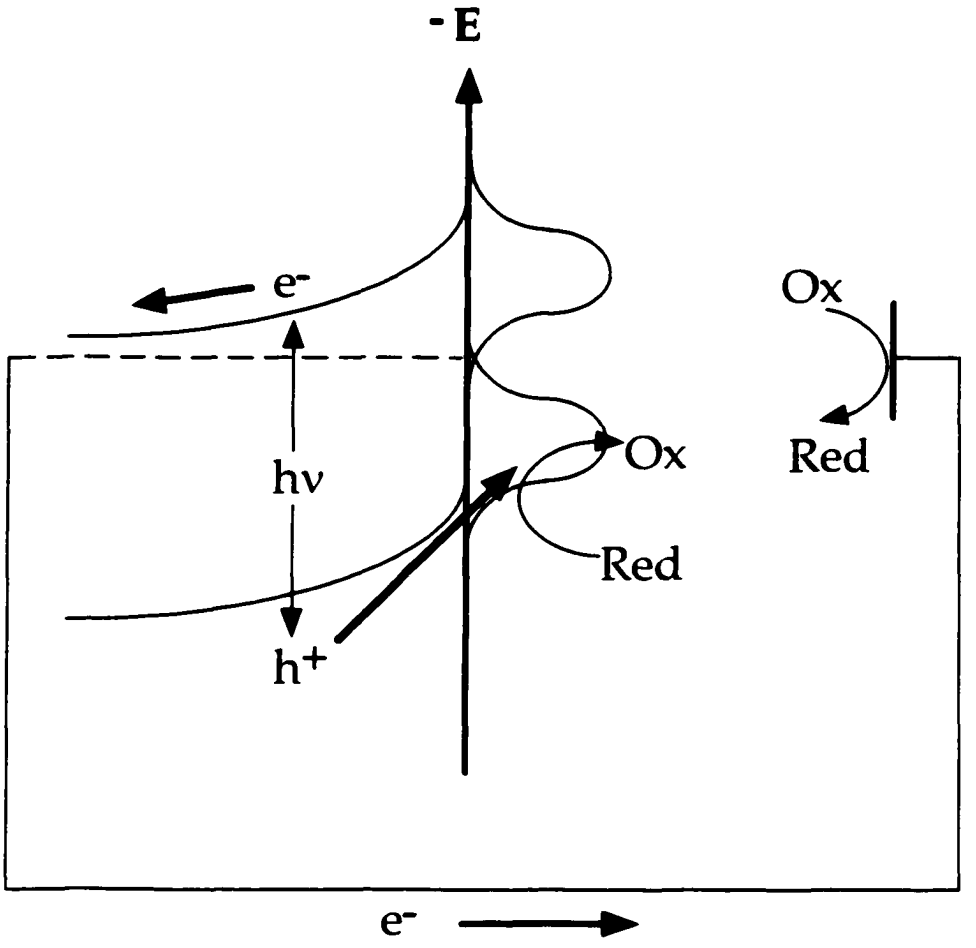

Figure 1.5. Photoinduced electron transfer at a n-type semiconductor. Photoexcitation is represented by the term hν.

direct information on the characteristics of the optical transition. Illuminated current voltage curves also give information on the nature of the interfacial energetics and the kinetics of charge transfer.[23]

The conversion efficiency of illuminated photoelectrochemical cells is obtained by calculating the ratio of the maximum power output, P_{OUT}, to the incident radiant power, P_{IN}. Current-voltage curves are measured to determine the maximum power output. These curves provide data on the open circuit voltage (V_{OC}), the short circuit current density (I_{SC}) and the maximum power output point (IV_{MAX}). The maximum power output is then the product of $(I_{SC}V_{OC})f$, where f is the fill factor ($IV_{MAX}/I_{SC}V_{OC}$), a term used to relate the IV curve to the maximum power rectangle or P_{OUT}. Thus, the conversion efficiency is given by Equation 1.7:

$$\text{Efficiency (\%)} = \frac{(I_{SC}V_{OC})f}{P_{IN}} \times 100 \qquad (1.7)$$

Conversion efficiency calculations determine the overall efficiency of the solar energy conversion device.

Two primary processes that reduce the conversion efficiency are photocorrosion, and bulk or surface recombination. Photocorrosion is caused by the accumulation of minority carriers at the semiconductor-electrolyte junction which then break surface bonds. Recombination occurs when the electron hole pair generated by illumination recombines. This latter phenomenon can occur directly or through an intermediate energy level in the bulk or at the surface of

the semiconductor.[16] These "surface states" are thought to occur because of dangling bonds and defects at the surface. They often lead to Fermi level pinning where the energy level remains at the energy of the surface state regardless of changes in the redox species, E°, or the applied potential. Surface states act as an electron source or sink and, in general, lead to a decrease in the control over the interfacial energetics.

While recombination decreases the power output, photocorrosion eventually dissolves the entire semiconductor. Photocorrosion occurs when a semiconductor electrode, in contact with an electrolyte solution, is illuminated with radiation greater than the band gap. This generates electron-hole pairs and, with charge separation, excess charges (minority carriers) accumulate at the surface where they can react, breaking chemical bonds. This occurs for n-type semiconductors when excess holes in the valence band accumulate at the surface and oxidize surface bonds. The n-type semiconductors appear to be more susceptible to photocorrosion than the p-type as their minority carriers, holes, are more reactive with respect to surface bonds. Another variable that affects photocorrosion is the electrolyte solution; aqueous solutions seem to be more reactive than organic solutions as water can act as an electron acceptor or donor. The addition of a redox couple to the solution can diminish the effects of photocorrosion but thermodynamic calculations by Gerischer[24] reveal that every semiconductor is susceptible to photocorrosion to some degree. There are several strategies to avoid or diminish the affects of photocorrosion. They

include dye sensitization, which generates electrons in the conduction band without creating holes in the valence band,using nonaqueous electrolytes and adsorbing or bonding a redox species to the semiconductor surface. It is also possible to isolate the semiconductor surface from the electrolyte with a metal or polymer coating[16] and to use layered semiconductors in which the valence band has non-bonding character.[25]

Dye Sensitization. Dye sensitized systems consist of a dye molecule, usually with an absorbance in the visible region, adsorbed on the surface of a large band gap semiconductor (see Figure 1.6). The strategy is to sensitize a stable large band gap semiconductor to radiation with lower energy than the band gap. This process depends on how the semiconductor and dye energy levels match up on an absolute energy scale. Figure 1.6 depicts an ideal energy scheme for dye sensitization of an n-type semiconductor. The first excited state of the dye overlaps the conduction band edge allowing dye sensitization to be possible.

The promotion of electrons in the conduction band normally requires radiation with energy equal to or greater than the band gap. However, when dye molecules with transition energies less than the band gap but with S^*/S^+ more negative than E_{CB} are adsorbed on the semiconductor surface, as shown in Figure 1.6, electron transfer occurs from the excited electronic state in the adsorbed dye to the conduction band of the semiconductor.[26] If a bias potential is applied or a redox species added to the electrolyte solution an electric field is

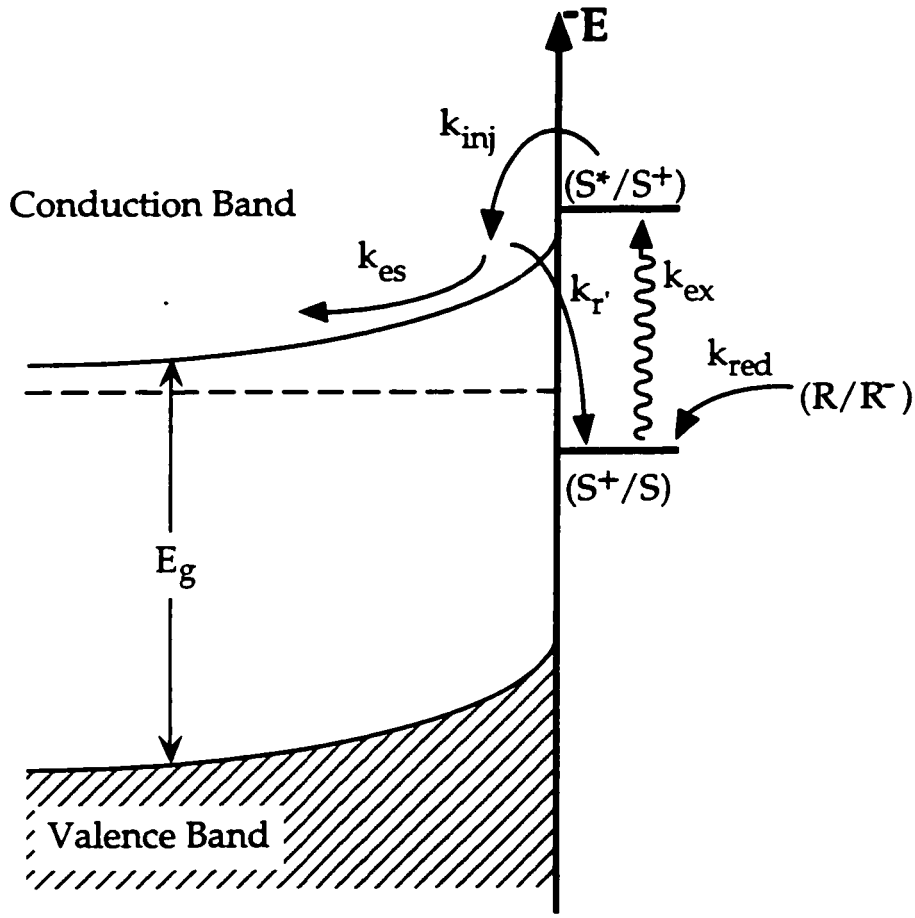

Figure 1.6. Kinetic scheme for electron transfer for dye sensitized n-type semiconductor.

generated by the semiconductor/liquid junction. This creates a depletion region at the semiconductor surface that induces charge separation.

The generally accepted kinetic scheme for dye sensitization is depicted in Figure 1.6. In this system there is an energy overlap between the excited state of the adsorbed dye and the conduction band of the semiconductor. When the semiconductor/dye system is irradiated with sub band gap light, an electron is promoted from the ground state to the first excited state of the adsorbed dye (k_{ex}). Excitation is followed by electron injection from the excited state of the dye to the conduction band of the semiconductor (k_{inj}). At this point, the electron can either be efficiently separated from the oxidized dye (k_{es}) or recombine with the dye in the ground state ($k_{r'}$). If the electron is collected as photocurrent then the oxidized dye is reduced by a regenerating agent (k_{reg}) in the supporting electrolyte solution. An electron donor (regenerating agent) donates an electron to the ground state of the excited dye before recombination can transpire.

Early Dye Sensitization Studies on Crystalline Semiconductors. Some of the earliest work on semiconductor photoelectrochemistry was performed by Tributsch and Gerischer[27,28] on single crystal ZnO. Spectral sensitization of ZnO, an n-type semiconductor, was achieved through the light absorption by three organic dyes; rhodamine B, rose bengal and crystal violet, that were adsorbed to the semiconductor surface. Sensitization was evident when photoaction spectra (photocurrent vs wavelength) and the absorption spectrum of the dye in solution proved to be in agreement.

Continued work in this area was accomplished by Memming and Tributsch[29] on p- and n-type crystalline GaP electrodes. They discovered that only the cathodic photocurrent was enhanced when various dyes, such as rhodamine B, rose bengal, and crystal violet, were added to the electrolyte solution. This current flow was achieved when electrons in the valence band were injected into the ground state of the adsorbed dye producing holes in the valence band of GaP. The electric field at the semiconductor-electrolyte interface repels these holes into the interior of the semiconductor generating current. The sensitized cathodic photocurrent was typically much smaller for n-type GaP than for p-type. This resulted from the greater potential barrier to electron injection from the electrode to the ground state of the dye for n-type GaP.

Earlier work by Gerischer and Tributsch[27] with n-type ZnO revealed strikingly different results compared to those obtained with n-type GaP. In their studies, Gerischer and Tributsch observed sensitized anodic instead of cathodic photocurrents for n-type ZnO. These differences were attributed to the energetics of each semiconductor.[29] Both the position of the conduction and valence bands on an absolute energy scale, as well as the actual band gaps of these two materials, differ (see Figure 1.7). Therefore, disparities in the sensitized photocurrent were observed because on an absolute energy scale, the first excited state of the dyes studied straddles the valence band for both p- and n-type GaP, and the conduction band for ZnO. The cathodic photocurrent was generated as described previously while the anodic photocurrent resulted when

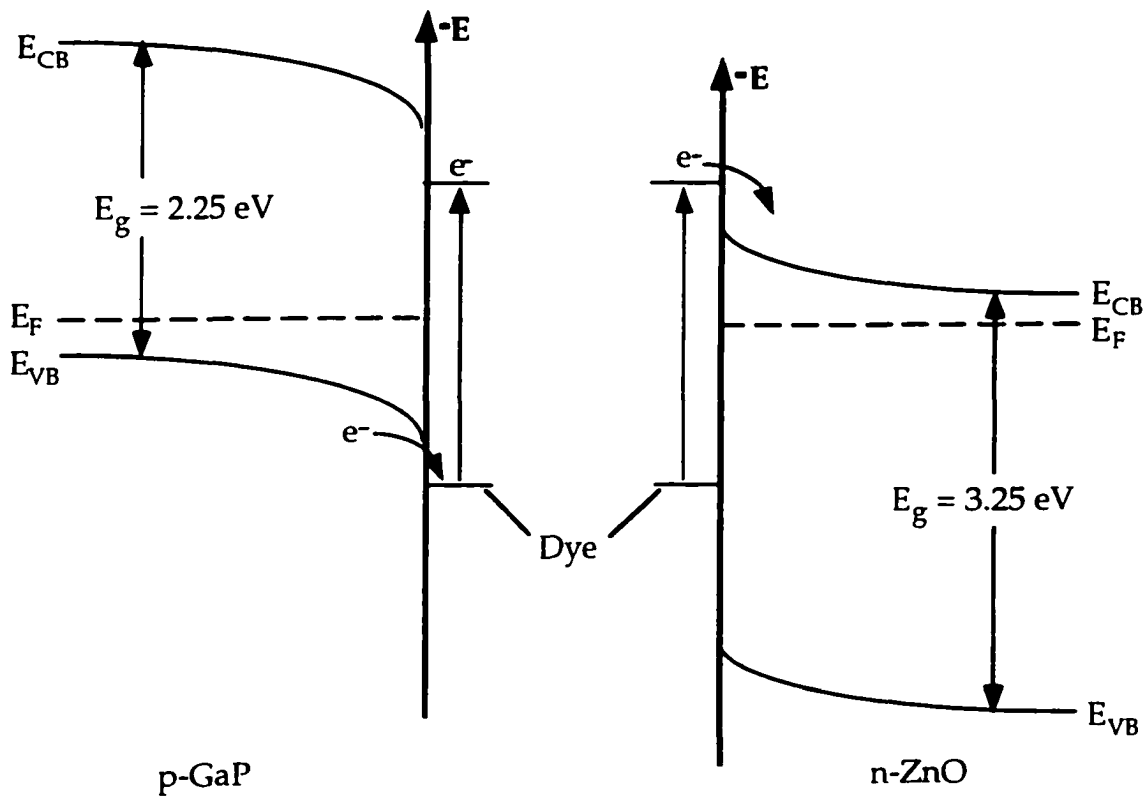

Figure 1.7. Energetics of dye sensitized p-GaP and n-ZnO.

electrons from excited dye molecules were injected into the conduction band as depicted in Figure 1.7 for ZnO.

Memming and Tributsch noted several other photoelectrochemical differences between GaP and ZnO.[29] One intriguing result was the different responses to oxidizing and reducing species added to electrolyte/dye solutions. Reducing agents such as hydroquinone (H_2Q) increased the anodic sensitization current for ZnO in rose bengal, crystal violet or rhodamine B solutions, but not for p-type GaP. However oxidizing agents such as O_2 increased the sensitization for p-type GaP in similar dye solutions, but not for ZnO. Following the energy the scheme depicted in Figure 1.8, reducing agents should prevent current flow from p-GaP to the dye ground state while oxidizing agents should deplete the first excited state of dye electrons. Thus, photocurrent generated at a GaP electrode, was predicted to decrease upon the addition of reducing agents and increase with the addition of oxidizing agents. The decrease in photocurrent was explained by the competitive rate of electron transfer from the reducing agent to the grounds state of the dye (k_R). This mode of electron transfer reduced the rate of electron injection from the valence band to the ground state of the dye (k_V) as shown in Figure 1.8. Because there is only a slight decrease in photocurrent, k_V is predicted to be much greater than k_R. Furthermore, the dye must be adsorbed on the semiconductor surface for fast electron transfer between the valence band edge and the ground state of the dye. ZnO, on the other hand, has an energy scheme with the first excited state of rose bengal, crystal violet or rhodamine B

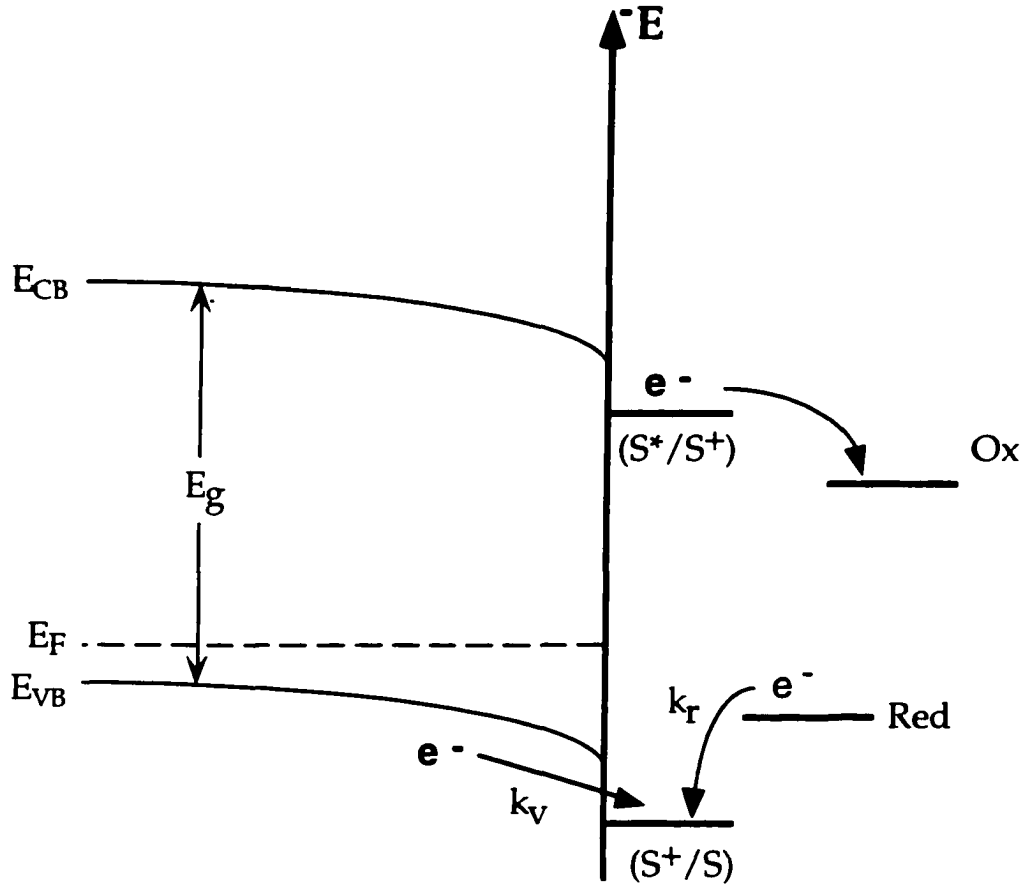

Figure 1.8. Energy scheme for dye sensitized p-GaP showing supersensitization.

straddling the conduction band edge as shown in Figure 1.7.[29] Thus, reducing agents regenerate the ground state of the dye, causing an increase in the sensitization current. In this situation the reducing agent was referred to as the regenerator or the supersensitizer.[29]

Memming and Tributsch tried to determine whether the mechanism of sensitization on GaP was based on energy or charge transfer. They predicted that if the process were primarily dependent on energy transfer, then low quantum efficiencies would be obtained due to recombination. This was based on the knowledge that a direct energy transfer from a dye to GaP would generate an electron-hole pair at the semiconductor surface where there was a high recombination rate. However, relatively high quantum efficiency values, on the order of 10-30%, were obtained which led Memming and Tributsch to conclude that charge transfer was the primary mechanism of sensitization for GaP.

In 1972, work by Gerischer[30] examined the fundamental principles for dye sensitization of p- and n-type crystalline semiconductors. At this time, electron transfer had already been established as the primary step for photosensitization. Scientists had also realized that large band gap semiconductors were well suited for photosensitization.[27,29,31] These semiconductors had intrinsically high resistivities but doping allowed reasonable conductivities to be obtained.[30] In order to compare various semiconductor-liquid junctions, the band edges at the semiconductor surface were recorded on a common energy scale for electrochemical analysis. The addition of redox species was eliminated as

Gerischer was interested in semiconductor-dye interactions. Instead of adding redox species, a potentiostatic bias was applied to the semiconductor, anodic for n-type and cathodic for p-type, to create a depletion region at the semiconductor surface. The depletion region allowed charge separation; preventing the recombination of the injected electron with the dye. This explains earlier studies where the sensitization of both n- and p-type GaP had been examined with cathodic biasing and the n-type GaP had shown extremely low sensitization photocurrents.[29] Gerischer's work[30] focused on the electron energy level densities of dissolved dyes and provided an understanding of solvation effects associated with the oxidized and reduced form of dyes.

Photosensitization studies on semiconductor-dye interactions were continued by Memming.[32] His earlier work with Tributsch on GaP revealed a decrease in the sensitzation photocurrents over time for various dyes.[29] This suggested that the dyes must adsorb to the surface to sensitize the semiconductor. Their hypothesis was supported by Memming's studies on the effects of competitive adsorption between two dyes that both access the triplet state, eosin and methylene blue, adsorbed on single crystal p-SiC. Since methylene blue has been shown to adsorb more strongly than eosin[32], this characteristic was manipulated to monitor the decrease in photocurrent for eosin upon a systematic addition of methylene blue. This difference in adsorption strength could be attributed to the planar conformation of methylene blue compared to the bent structure associated with the benzoate group of eosin.

Photocurrent results showed the sensitization signal for eosin decreased with time as the methylene blue signal increased. These results agreed with the postulation that since methylene blue adsorbs more strongly, the eosin was replaced by methylene blue. However, since the triplet state of eosin had a longer lifetime, 2.2 μs[33] compared to 150 ns for methylene blue[34], these observations could have been the result of an energy transfer from eosin to methylene blue.

Continued efforts on electrode reactions of excited molecules were carried out by Gerischer and coworkers[35]. They theoretically derived both the redox potentials for the donor and acceptor states of an excited dye molecule, and the quantum yield of charge injection by excited molecules per absorbed photon. Then the theoretical quantum yields were compared to actual in situ measurements for a series of Kodak dyes on ZnO. These experiments were performed using attenuated internal reflection techniques (ATR), where light absorption and photocurrent were simultaneously measured with ZnO as the internal reflection element.[36] While the actual quantum yield results were much lower than the theoretical prediction, this was attributed to a greater degree of surface recombination facilitated by surface states present on the semiconductor above and below the conduction band edge. This explanation was supported by the increase in quantum yield associated with the addition of ethylene diamine to the electrolyte solution. This reagent was predicted to passivate vacant surface states, decreasing recombination reactions.

An effective study on the photo-oxidation of rose bengal adsorbed on ZnO was accomplished with ATR techniques by Spitler and coworkers[37]. Although photo-oxidation had typically been studied through electrochemical methods Spitler choose to utilize ATR methods, as previously discussed, to directly measure sensitization characteristics of adsorbed dyes. This was possible because the evanescent wave generated from ATR extends about 2000 Å into the dye containing solution. These ATR studies enabled Spitler to uncover information on adsorption sites, the rate of adsorption, and molecular orientation of rose bengal.

Time resolved ATR measurements showed the bulk of dye adsorption occurring within the initial 100 seconds followed by much slower long term adsorption. These results led Spitler to conclude that there were a variety of adsorption sites with different heats of adsorption. In addition, the rate of adsorption declined substantially when a bias was applied to the ZnO crystal. This was evidenced by a drop in photocurrent associated with the oxidation of rose bengal. Because the drop in photocurrent coincided with the applied potential onset, this suggested that the oxidized dye might not desorb quickly or perhaps oxidation products adsorbed to the ZnO surface. Furthermore, these experiments indicated that the electrolyte affected the quantum efficiency of dye sensitized ZnO.

In conjunction with ATR measurements, the absorption spectra for both parallel ($\parallel$) and perpendicular ($\perp$) polarized light were analyzed to determine

the orientation of the dye adsorbed to the ZnO surface.[37] Absorption spectra were measured by focusing modulated light from a Xenon lamp on the "entrance surface" of the crystal, similar to ATR experiments. Because the absorption spectra showed no significant differences, rose bengal appeared to be randomly oriented.

Another aspect of photosensitization that has received considerable attention of late was the reduction in photocurrent caused by a back reaction. Spitler[38] addressed this issue in his continued ATR studies of single crystal ZnO sensitized with rhodamine B and rose bengal. These investigations concentrated on whether the low quantum efficiency (~10^{-2}) could be attributed to a fast back reaction between the injected electron and the oxidized dye molecule or an energy transfer due to fast quenching through neighbor adsorbed dye molecules in close proximity. Spitler monitored the quantum efficiency as a function of surface coverage. As the surface coverage decreased the quantum efficiency was reduced. There was no increase in the quantum efficiency, even when the surface coverage went as low as $\theta \leq 0.001$, well below the critical concentration for energy transfer. This led to the conclusion that, even though the driving force for electron injection from dye to semiconductor was large, the back reaction sufficiently reduced the quantum efficiency. Analysis of the data indicated there were two forms of dye, one a more efficient sensitizer than the other. Because the quantum efficiency decreases with decreasing surface coverage, it was presumed that the more efficient dye forms adsorbed less

tightly. Similar effects had been studied through thermal desorption experiments by another group and they concluded that this difference was caused by "special sites" composed of hydroxyl groups on the semiconductor surface.[39]

Direct spectroscopic information was obtained for electron transfer of eosin adsorbed on crystalline TiO_2, SnO_2 and ZnO by Spitler and coworkers[33] through internal reflection flash photolysis measurements. This technique allowed photochemical transients for dye injection to be measured at the semiconductor surface following flash photolysis. These experiments indicated that the ground state bleaching of the dye occurs via electron injection from the singlet and triplet states to the TiO_2 conduction band. The triplet electron injection rate was calculated to be about $2x10^5$ s^{-1} while singlet electron injection occurred on a time scale shorter than the 100-ns resolution of the instrument. However, the back reaction rate was determined to be $2.6x10^5$ s^{-1}. This was the first direct evidence for electron injection from an adsorbed triplet dye into the semiconductor. The result was obtained even though the estimated overlap of the triplet donor states with the acceptor states of TiO_2 (conduction band) were very poor. This indicated that extensive overlap was not necessary. Due to the low quantum yields, a greater portion of the adsorbed dye must have its excited state quenched through energy transfer or electron transfer back reaction. Current voltage measurements indicated the possibility of surface states being involved in the recombination of injected electrons with oxidized dye molecules.

Dye Sensitized Colloidal TiO_2. Early work on single crystal TiO_2 sensitized with polypyridineruthenium complexes by Clark and Sutin[40] investigated the effects of pH on the energetics of their system. Studies showed the band edges of TiO_2 were pH dependent. Raising the pH shifted the band edges to more anodic potentials. A similar effect was not observed for polypyridineruthenium complexes. The reduction potentials of these dyes varied with the ligand moieties but were independent of pH. Therefore the energy overlap between the ruthenium complexes and the TiO_2 band edges are altered with changing pH. As the pH was increased the driving force for electron injection from a ruthenium complex was decreased. This translates to a decrease in photocurrent sensitization with increasing pH.

Recent developments on nanocrystalline TiO_2 by Zaban and coworkers[41] revealed strikingly different results for pH dependencies. These experiments were carried out in response to results published by Yan and Hupp[42] on pH independent rates of back electron transfer. Colloidal TiO_2 films were coated with a ruthenium complex and the corresponding absorption spectrum measured. Then the sensitized film was soaked in an aqueous Br_2 solution at a fixed pH. By monitoring the fraction of oxidized dye produced as a function of pH, it was determined that both the band edges and the dye reduction potentials shifted with changes in pH. Extensive control over the driving force for electron injection via pH control is therefore not possible for nanocrystalline TiO_2. This result varied from single crystal TiO_2 where the semiconductor band edges

shifted with increasing pH. These unique properties of nanocrystalline TiO_2 have led to profound advances in solar energy conversion.

The Grätzel Cell. High surface area polycrystalline anatase TiO_2 has been studied extensively in the past 10 years. This material has been incorporated into extremely efficient liquid junction solar cells by Grätzel and coworkers[2]. They found that by increasing the surface area of the film, more ruthenium dye was adsorbed on the semiconductor surface which increased the quantum yield as more of the irradiating light was absorbed. This is the result of only adsorbed molecules inject electrons into the semiconductor as excited-state life times are too short to allow for diffusion of solution species to the semiconductor surface.[22]

The TiO_2 solar cells were assembled in a sandwich configuration. A thin layer of colloidal TiO_2 was spread on conductive glass followed by the adsorption of ruthenium dye. An electrolyte solution consisting of I^-/I_3^- in acetonitrile was then sandwiched between the dye sensitized TiO_2 and a Pt counter electrode. The most efficient sensitizer developed has been *cis* di(thiocyanato)-bis(2,2'-bipyridyl-4,4'-dicarboxylic acid)ruthenium(II), $Ru(dcbpy)_2(SCN)_2$.[43] This system has achieved a conversion efficiency of greater than 10% and has already been incorporated into commercial use.[2] Much is still unknown about the interfacial electron transfer of this system.

Photoelectrochemical and Dye Sensitization of Crystalline Layered Materials. Metal dichalcogenides were investigated for photoelectrochemical applications in the late 1970s by Tributsch.[25] Originally $MoSe_2$ and WSe_2 were

examined, but today a number of other layered compounds have also been studied. These materials exhibit long term stability to corrosion and high solar energy conversion efficiencies.[44-48] The van der Waal (0001) surfaces of these layered materials are ideal for studying dye sensitization. They should be devoid of surface states making them difficult to oxidize and fairly unreactive to solvents.[49]

Early work on SnS_2 by Katty and coworkers[50] examined the photoelectrochemical behavior of this material in aqueous solutions. N-type single crystals were grown via chemical vapor transport (CVT). These crystals exhibited low dark currents under anodic polarization. Upon illumination the current-voltage curves were shifted revealing a photocurrent onset dependence on the redox reagent as well as the pH of the solution. Increasing the pH led to a negative shift in photocurrent onset. These conclusions were confirmed by capacitance measurements that showed similar shift in the flat band potential.

Shifts caused by the redox species were thought to occur as a result of either band edge movement or surface states close to the conduction band edge. This conclusion was reached from observation of photopotential shifts caused by the introduction of redox species that had different redox potentials into the electrolyte solution. Under anodic bias, in an acidic solution, the addition of I^-/I_2 shifted the photocurrent onset to more negative potentials possibly because there was a large increase in the number of acceptor states on the surface created by the production and adsorption of I_3^-, Equation 1.8:

$$I^- + I_2 \rightarrow I_3^- \quad (1.8)$$

When the addition of I^-/I_2 was to an alkaline solution, it produced a positive shift in the onset of the photopotential and the dissolution of the electrode.[51] Adding S^{2-}/S_2^{2-} to solution, on the other hand, shifted the flat band to more negative potentials due to the increased negative charge on the surface.

SnS_2 was shown to degrade with continuous illumination in acidic or basic solutions. Decomposition products were monitored and the following anodic decomposition reactions were predicted for acidic (pH = 0) and basic (pH = 14) solutions, respectively:

$$SnS_2 + 4h^+ \rightarrow 2S + Sn^{4+} \quad (1.9)$$

$$SnS_2 + 3H_2O + 4h^+ \rightarrow 2S + SnO_3^{2-} + 6H^+ \quad (1.10)$$

While the cathodic decomposition in acidic solutions was proposed as follows:

$$SnS_2 + H_2O + 2H^+ \xrightarrow{2e^-} SnO + 2H_2S \quad (1.11)$$

In basic solutions, SnO was presumably formed but then reacted with oxygen to produce SnO_3^{2-}. The effects of photocorrosion were diminished in acidic solution via the addition of KI to the electrolyte solution as I^- can be oxidized by photogenerated holes. In conclusion, SnS_2 appears to have low anodic current in the dark, to be susceptible to photocorrosion and to have a photopotential dependent on pH and the redox couple used. Electrodes can, however, be stabilized with iodide in acidic solutions.

Dye sensitization studies of layered metal dichalcogenides by Spitler and

Parkinson[49] revealed high absorbed photon to current efficiencies for these materials. Specifically, n-WS_2 and n-WSe_2 electrodes were sensitized with thiapentacarbocyanine, an infrared absorbing dye. At low surface coverage, this dye appeared to occupy all adsorption sites. This was concluded as even a 400 fold increase in dye concentration in solution did not increase the photocurrent response. Aggregation was observed at higher dye concentrations as a blue shift in the photoaction spectrum.

Analysis of the photoaction spectra allowed one of the two forms of the adsorbed infrared dye, cis vs trans, to be determined. The cis form of the dye was stabilized in polar solvents. Results indicated that the trans form of the dye was adsorbed to the semiconductor surface. This allowed the investigators to conclude that the surface of the semiconductor was essentially nonpolar and, thus, further characterized the semiconductor surface.

Incident photon to current efficiency (IPCE) or quantum yield per incident photon (QYIP) measurements were taken for dye sensitized WSe_2 electrodes. Combined with previous results from work on rhodamine B the quantum efficiency per absorbed photon (QYAP) was estimated at 0.6 to 0.8.[52] This result supports the evidence that layered dichalcogenide materials are excellent substrates for studying dye sensitization as virtually all photoexcited electrons are injected into the conduction band.

Parkinson studied dye sensitization of another layered dichalcogenide material, SnS_2.[53] This layered semiconductor has a larger band gap than the

previously studied WSe_2 or WS_2 allowing a larger variety of dyes to be investigated. Parkinson surveyed over thirty dyes and determined that there was a linear relationship between the absorption maximum and the potential energy difference between the first oxidation and reduction potentials of the dyes in solution. Thus, the first excited state, S^*/S^+, from Figure 1.9 was approximated as S/S^- which can be measured electrochemically.

Single SnS_2 crystals grown for this study had low doping densities (10^{15} cm^{-3}) that affected the quantum efficiency. Higher doping density levels were desired as, according to Spitler's one dimensional charge injection theory, low doping densities are synonymous with low quantum efficiencies.[54] Indeed, higher quantum efficiencies were observed in the previous study with WSe_2 (10^{17} cm^{-3}).[49] Higher doping density created a narrower space charge region in the WSe_2 crystals that corresponded to a high electric field gradient providing more efficient charge separation and higher quantum efficiencies. Thus, attempts were made to increase the doping density of SnS_2 through the incorporation of chlorine as a dopant instead of phosphorous.

Later work by Parkinson and Spitler[48] investigated high quantum yield dye sensitization on SnS_2 single crystals doped with chlorine. In this work current-voltage characteristics were analyzed and the effects of the regenerating agent were examined. Differences between adsorbed and "free" dyes were studied. The photocurrent spectrum for oxazine at a SnS_2 electrode was compared to the absorption spectrum of oxazine in solution. The action

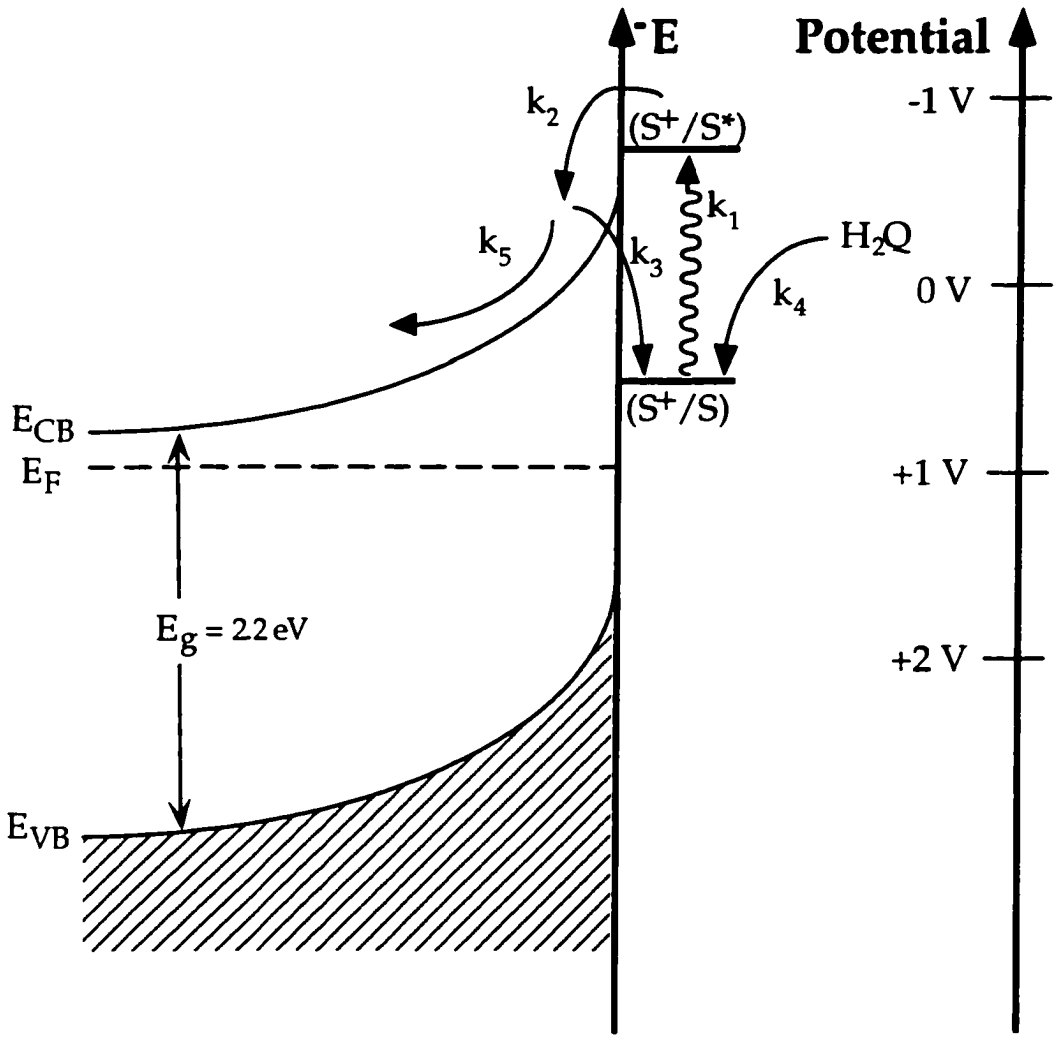

Figure 1.9 Kinetic scheme for electron transfer events at SnS_2.

spectrum was red shifted and had a tail at long wavelengths. While spectral shifts are common, the origin of the long wavelength tail was not fully understood. This "tail" was considered a phenomenon of dye aggregation or possible evidence of a direct electron transfer to the conduction band from the dye, bypassing the dye excited state. Time resolved electron injection studies were undertaken to better understand the dynamics of dye sensitization.

Charge Injection. Early investigations of dye sensitized charge injection either into or from semiconductors provided researchers with a general understanding of charge transfer processes at the semicondcutor-solution interface.[27,29-31] Electrochemical techniques were utilized to probe electron transfer reactions at the semiconductor surface. From this work, Gerischer[30] determined the rate of electron transfer from a dye excited state to the conduction band for an n-type semiconductor as denoted by the following reaction:

$$D^* \rightarrow D^+ + e^-_{CB} \tag{1.12}$$

where e^-_{CB} is an electron in the conduction band. The rate of electron transfer for this process is proportional to the following exponential term:

$$j^*_C \sim \exp\left(-\frac{(E_C - {}^0E_D - E^*)^2}{4L^*_D kT}\right) \tag{1.13}$$

where j^*_C is the current density, E_C is the energy of the conduction band edge, ${}^0E_D$ is the ground state energy level of the dye, E^* is the excited state energy of the dye and L^*_D is the reorganization energy in the excited state. While this

derivation of the electron transfer rate accounts for both the reorganization energy associated with solvation and the energy difference between the dye excited state and the conduction band edge, actual and theoretical results varied.

Attempts to more rigorously describe electron transfer were pursued by Spitler[54] who described dye sensitized charge injection into semiconductors with his one dimensional diffusional model based on the Onsager[55] model for charge carrier separation in a dielectric material. His model was based largely on previous work by Charlé and Willig[56] where they developed a diffusional model for charge injection at organic insulator interfaces. Spitler's model aimed at predicting the role of image charge forces, back reactions and surface defects in current production by charge injection from excited dye molecules at semiconductor surfaces.

The Spitler model centers on the assumption that electrons that are generated in the conduction band for n-type semiconductors are exposed to the electric field of the space charge region. These electrons can either be collected as current or they can recombine with the oxidized dye due to thermal diffusion. The escape of surface generated charge carriers into the bulk of the semiconductor may be impeded by the formation of an image force charge.[54] A positive force charge is generated in the electrolyte solution when an electron from a dye molecule is injected into the semiconductor, repelling the injected electron from the surface. The rate of escape or recombination for electrons generated at the surface are determined by the features of the space charge

region. This theory predicts that the current-voltage characteristics depend on the dielectric constant of the solvent, the recombination rate for electrons at the surface, and the stabilization of the oxidized dye molecules.

In this model, the space charge region spans the distance from $x = x_0$ at the semiconductor surface to $x = W$ at the edge of the space charge region. Spitler defines the boundary conditions for the recombination and generation of thermalized carriers at x_0 and W:

$$j(x_0) + k_{rec}^{em}\rho(x_0) = j_g^{em} \tag{1.14}$$

$$j(W) + k_{rec}^{coll}\rho(W) = j_g^{coll} \tag{1.15}$$

where $\rho(x)$ is the charge density, k_{rec}^{em} is the recombination velocity of the reaction of the thermalized charge carriers with acceptors at the surface, k_{rec}^{coll} is the thermal velocity of charge carriers in the bulk, j_g^{em} is the generation rate of electrons at the semiconductor surface and j_g^{coll} is the generated electrons that are collected. From the boundary conditions and assuming that the recombination rate at the surface was much slower than the recombination in the bulk ($k_{rec}^{em} < k_{rec}^{coll}$), an equation for the current produced is determined to be:

$$j = j_{ISL} + (1/1 + (bk_t / k_{dis}F)R / k_{es})\{bR - j_{ISL}\} \tag{1.16}$$

where $R = \{1 + (N_D k_r / k_{dis}F)R / k_{dis})\exp(-\Delta\phi / kT)\}^{-1}$, j_{ISL} is the current produced in the limit where k_{rec}^{em} was infinitely large and the surface is an ideal sink for electrons, b is the total injected charge, k_{es} is the escape velocity of the injected charge. The drop in the work function across the space charge region was

$\Delta\phi = \phi(x_0) - \phi(W)$ and k_{dis} was the rate constant for the disappearance of the oxidized dye from the substrate surface through all paths except electrochemical reduction. A linear dependence between the collection rate (j_g^{coll}) and the doping density (N_D) was predicted from this theory:

$$j_g^{coll} = k_{rec}^{coll} N_D e \tag{1.17}$$

Equation 1.17 demonstrates that an increase in the doping density should result in an increase in the collection of electrons corresponding to an increase in the quantum efficiency. Changes in the collection rate or recombination in the bulk of the semiconductor could diminish the effects of changes in the doping density.

The escape velocity, k_{es}, is the rate at which electrons move from the semiconductor surface to the edge of the space charge region. From the theory detailed by Spitler[54], this rate is affected by the potential barrier and the diffusion constant of the charge carrier:

$$k_{es} = D / \int_{x_0}^{W} \exp(-\Delta\phi / kT) \tag{1.18}$$

Electrons that do not escape into the bulk can recombine with surface states or solution species. Spitler reported that the most important recombination site at the surface was the oxidized dye. The rate of recombination (k_{rec}) is viewed as a pseudo first order rate constant:

$$k_{rec} = k_r'[D^-] \tag{1.19}$$

In order to predict the photocurrent, j, the potential was assumed to be $\phi(x) = -q' / 16\pi\varepsilon\varepsilon_0 x - V_{appl}(x)$, which accounts for the image charge force (q') and

the applied potential (V_{appl}). This resulted in current-voltage curves that showed influences of image charge forces, recombination rate constant (k_r') and the recombination ratio (k_r' / k_{dis}). The image charge force creates a shift in the flat band to more positive potentials as the escape of electrons from the semiconductor surface is inhibited. Increases in the recombination rate constant caused shifts in the current-voltage curves to more positive potentials as a larger driving force was required to collect the injected electrons. Thermalization lengths were determined to play a minor role in the kinetic scheme and will not be discussed further.

This model was tested on layered dichalcogenide semiconductor electrodes.[54] These semiconducting materials were chosen because they exhibit atomically smooth surfaces that are virtually defect free and, are thus ideal substrates.[49] The absorbed photon to electron conversion was 0.6-0.8 for the semiconductors WS_2 and $MoSe_2$ with 3,3'-diethyl-9,11,15,17-dineopentylene-2,2'-thiapentacarbocyanine adsorbed on the surface. Spitler observed a decrease in quantum efficiency for surfaces with a large number of defects and upon the addition of an additional acceptor species to the electrolyte. The one dimensional model developed by Spitler agreed with experimental results. However, this model only allows the current produced by thermalized charged carriers to be calculated and does not yield information on the actual carrier dynamics.

Spitler's theory was tested with an in-depth analysis of the

photocurrent-voltage behavior.[54] In agreement with the theory, an increase in the concentration of regenerator corresponded to an increase in the photocurrent. There was also a shift in the half wave potential of the dye to more negative potentials associated with an increase in the regenerator concentration. This can be explained via the kinetics of the system as diagrammed in Figure 1.9. As the concentration of regenerator was increased, the recombination rate, k_3, had to compete with regeneration of the dye ground state, k_4. Therefore, the recombination rate decreased and the quantum efficiency increased.

Adsorption isotherms were measured for monomeric and aggregating dye species to further analyze what effects the regenerating agent (H_2Q) has on the back reaction (k_3). This was accomplished by comparing adsorption isotherms obtained with and without H_2Q in solution. The adsorption was monitored by measuring the quantum efficiency as these were shown to be proportional. It was presumed that H_2Q was not adsorbed to the semiconductor surface because the quantum efficiency did not increase when H_2Q was absent. The authors suggested there could be a cooperative adsorption between H_2Q and dye molecules or a reduction in the back reaction brought about by the addition of H_2Q.[49]

Similar effects were seen with aggregate dye species. However, these adsorption isotherms were not as reproducible as those obtained for monomer species. It was postulated that edge sites might affect the reproducibility or that there could be coexisting monomer and aggregate dye species. Because only

blue and red shifts in the photoaction spectra were observed for dye aggregates with no additional peaks appearing at higher dye concentration, aggregation was presumed to be a surface phenomena.

Spectral shifts for dye molecules upon adsorption and aggregation, in agreement with previous work, were observed by Spitler[54]. This was expected as the solvation was altered when dye molecules adsorb onto a surface and aggregate. A linear relationship was measured between the sensitization maximum and the absorbance maximum for dyes in solution.

Recent studies of dye sensitization kinetics have focused on the rate of electron injection. Grätzel and coworkers[57] outlined a general scheme for the rate constants of nanocrystalline TiO_2 sensitized with a Ru complex in 1995. Electron injection was reported as 10^{10}-10^{12} s^{-1}, the back reaction at 10^6 s^{-1} and the electron movement in the nanocrystalline TiO_2 electrode to the back-contact at approximately 10^3-10^0 s^{-1}. Fluorescence quenching studies of oxazine adsorbed on SnS_2 in 1992 revealed similar electron injection rates, $3x10^{13}$ s^{-1}.[58]

Further research on the rate of electron injection from ruthenium dyes to TiO_2 was carried out by Willig and coworkers[59] with ultrafast time-resolved spectroscopy. They determined that the primary light-driven electron transfer process of Ru-dyes chemisorbed on TiO_2 occurred with a rise time of less than 25 fs. Willig and coworkers[59] reported that the electron transfer reaction did not involve redistribution of vibrational excitation energy which was in agreement with the results published by the McCusker group[60], and Miller and coworkers[61].

Therefore the electron transfer reaction differs from the typical weak electronic interaction assumed with the Marcus-Levich-Jortner-Gerischer model.[62]

Work by Miller and coworkers[63] on the lifetime of conduction band electrons in dye sensitized SnS_2 was measured with ultrafast time-resolved spectroscopy. Their results revealed that there was a short lifetime (<60 fs) even at the conduction band minimum (CBM). Since the QYAP was high for this system[48], one possible explanation for the short CBM lifetime was that defect trapping competes with the back reaction.

Earlier work looked at the ground state recovery of oxazine sensitized SnS_2. Miller and coworkers[58] reported a rate of 10^{11} s^{-1} for the back reaction in this system. There were two components to the back reaction. The dominant feature of the fluorescence quenching signal was a fast, approximately 10 ps decay, while the weaker slower decay was 900 ps. The slower decay was presumed to correspond to less strongly coupled dye molecules. Similar results were observed for cresyl violet, another singlet dye. This back reaction rate differed dramatically from values reported by Grätzel[57] for TiO_2 nanocrystalline films sensitized with ruthenium complexes.

While considerable efforts in the field of dye sensitization have recently focused on nanocrystalline TiO_2, Miller suggested that because there were three basic materials with high efficiency dye sensitized photoinduced charge transfer they should all be thoroughly characterized and compared.[63] These three materials are two dimensional layered semiconductors such as SnS_2 and WSe_2,

silver halides and nanocrystalline TiO_2.

The following chapter details the growth of one of these materials, single crystal SnS_2, which is a two dimensional layered semiconductor. Chapters 3 and 4 investigate dye sensitization dynamics at the SnS_2-electrolyte interface and provide insights into this field of study.

REFERENCES

1 ERDA-49, *National Solar Energy Research, Development, and Demonstration Program* (US Government Printing Office, Washington, DC, 1976).

2 O'Regan, B. and Grätzel, M. *Nature* **353,** 737 (1991).

3 Vlachopoulos, N.; Liska, P.; Augustynski, J. and Grätzel, M. *J. Am. Chem. Soc.* **110,** 1216 (1988).

4 Becquerel, E. *C. R. Acad. Sci.* **9,** 561 (1839).

5 Brattain, W. H. and Garrett, C. G. B. *Bell Sys. Tech. Journal* **34,** 129 (1955).

6 Gerischer, H. Z. *Phys. Chem. (Munich)* **26,** 223 (1960).

7 Gerischer, H. Z. *Phys. Chem. (Munich)* **27,** 48 (1961).

8 Turner, D. R. *J. Electrochem. Soc.* **103,** 252 (1956).

9 Boddy, P. J. *J. Electrochem. Soc.* **115,** 199 (1968).

10 Dewald, J. F. *J. Phys. Chem. Solids* **14,** 155 (1961).

11 Williams, R. *J. Chem. Phys.* **32,** 1505 (1960).

12 Morrison, S. R. and Freund, T. *J. Chem. Phys.* **47,** 1543 (1967).

13 Gomes, W. P.; Freund, T. and Morrison, S. R. *J. Electrochem. Soc.* **115,** 818 (1968).

14 Fujishima, A. and Honda, K. *Bull. Chem. Soc. Japan* **44,** 1148 (1971).

15 Fujishima, A. and Honda, K. *Nature* **238,** 37 (1972).

16 Finklea, H. O., In *Studies in Physical and Theoretical Chemistry,* Vol. 55, Finklea, H. O., Ed. (Plenum, New York, 1988), pp. 1.

17 Hodes, G.; Howell, I. D. J. and Peter, L. M. *J. Electrochem. Soc.* **139,** 3136 (1992).

18 Sharp, L. I.; Dou, X. and Parkinson, B. A. *Langmuir,* in preparation.

19 McCaldin, J. O.; McGill, T. C. and Mead, C. A. *J. Vac. Sci. Tech.* **13,** 802 (1976).

20 Sze, S. M. *Physics of Semiconductor Devices,* 2nd ed. (John Wiley & Sons, New York, 1981).

21 Gerischer, H. Z. *Adv. Electrochem. Electrochem. Engr.* **1,** 139 (1961).

22 Tan, M. X.; Laibinis, P. E.; Nguyen, S. T.; Kesselman, J. M.; Stanton, C. E. and Lewis, N. S., In *Progress in Inorganic Chemistry,* Vol. 41, Karlin, K. D., Ed. (John Wiley & Sons, Inc, New York, 1994), pp. 21.

23 Howard, J. N. and Koval, C. A. *Chem. Rev.* **92,** 441 (1992).

24 Gerischer, H. *J. Electroanal. Chem.* **82,** 133 (1977).

25 Tributsch, H. *Ber. Bunsenges. Phys. Chem.* **81,** 361 (1977).

26 Miller, R. J. D.; McLendon, G. L.; Nozik, A. J.; Schmickler, W. and Willig, F. *Surface Electron Transfer Processes* (VCH Publishers, Inc., New York, 1995).

27 Gerischer, H. and Tributsch, H. *Ber. Bunsenges. Phys. Chem.* **72,** 437 (1968).

28 Gerischer, H.; Michel-Beyerle, M.-E.; Rebentrost, F. and Tributsch, H. *Electrochim. Acta.* **13,** 1509 (1968).

29 Memming, R. and Tributsch, H. *J. Phys. Chem.* **75,** 562 (1971).

30 Gerischer, H. *Photochem. Photobiol.* **16,** 241 (1972).

31 Michel-Beyerle, E.; Gerischer, H.; Rebentrost, F. and Tributsch, H. *Electrochim. Acta.* **13,** 1509 (1968).

32 Memming, R. *Photochem. Photobiol* **16,** 325 (1972).

33 Ryan, M. A.; Fitzgerald, E. C. and Spitler, M. T. *J. Phys. Chem.* **93,** 6150 (1989).

34 Capolla, N.; Lessard, R. A.; Carré, C. and Lougnot, D. J. *Appl. Phys. B* **52,** 326 (1991).

35 Gerischer, H.; Spitler, M. T. and Willig, F., In *Electrode Processes,* Vol. 80-3,

Bruckenstein, S., McIntyre, J. D. E., Miller, B., and Yeager, E., Eds. (The electrochemistry Society, Inc., USA, 1979), pp. 115.

36 Harrick, N. J. *Internal Reflection Spectroscopy* (Interscience, New York, 1967).

37 Spitler, M.; Lübke, M. and Gerischer, H. *Ber. Bunsenges. Phys. Chem.* **83,** 663 (1979).

38 Spitler, M. T. *J. Phys. Chem.* **90,** 2156 (1986).

39 Bressel, B. and Gerischer, H. *Ber. Bunsenges. Phys. Chem* **77,** 963 (1983).

40 Clark, W. D. K. and Sutin, N. *J. Am. Chem. Soc.* **99,** 4676 (1997).

41 Zaban, A.; Ferrere, S.; Sprague, J. and Gregg, B. A. *J. Phys. Chem. B* **101,** 55 (1997).

42 Yan, S. and Hupp, J. T. *J. Phys. Chem.* **100,** 6867 (1996).

43 Tachibana, Y.; Moser, J. E.; Grätzel, M.; Klug, D. R. and Durrant, J. R. *J. Phys. Chem.* **100,** 20056 (1996).

44 Tributsch, H. *Sol. Energy Mater.* **1,** 257 (1979).

45 Canfield, D.; Kam, K. K.; Kline, G. and Parkinson, B. A. *Sol. Energy Mater.* **4,** 301 (1981).

46 Fan, F. F.; White, H. S.; Wheeler, B. and Bard, A. J. *J. Electrochem. Soc.* **127,** 518 (1980).

47 Schneemeyer, L. F.; Wrighton, M. S.; Stacy, A. and Sienko, J. J. *Appl. Phys. Lett.* **36,** 701 (1980).

48 Parkinson, B. A. and Spitler, M. T. *Electrochimica Acta* **37,** 943 (1992).

49 Spitler, M. and Parkinson, B. A. *Langmuir* **2,** 549 (1986).

50 Katty, A.; Fotouhi, B. and Gorochov, O. *J. Electrochem. Soc.* **131,** 2806 (1984).

51 Fotouhi, B.; Katty, A. and Parsons, R. *J. Electroanal. Chem.* **183,** 303 (1985).

52 Spitler, M. T. and Calvin, M. *J. Chem. Phys.* **67,** 5193 (1977).

53 Parkinson, B. A. *Langmuir* **4,** 967 (1988).

54 Spitler, M. T. *J. Electroanal. Chem.* **228,** 69 (1987).

55 Onsager, L. *Phys. Rev.* **54,** 554 (1938).

56 Charlé, K. P. and Willig, F. *Chem. Phys. Lett.* **57,** 253 (1978).

57 Hagfeldt, A. and Grätzel, M. *Chem. Rev.* **95,** 49 (1995).

58 Lanzafame, J. M.; Miller, R. J. D.; Muenter, A. A. and Parkinson, B. A. *J. Phys. Chem.* **96,** 2820 (1992).

59 Hannappel, T.; Burfeindt, B.; Storck, W. and Willig, F. *J. Phys. Chem. B.* **101,** 6799 (1997).

60 Damrauer, N. H.; Cerullo, G.; Yeh, A.; Boussie, T. R.; Shank, C. V. and McCusker, J. K. *Science* **275,** 54 (1997).

61 Xu, S.; Miller, C. C.; Cao, J.; Mantell, D. A.; Mason, M. G.; Muenter, A. A.; Parkinson, B. A.; Miller, R. J. D. and Gao, Y. *J. Vac. Sci. Technol. A* **15,** 1510 (1997).

62 Gerischer, H., In *Solar Energy Conversion: Solid-State Physics Aspects*, Vol. 31, Seraphin, B. O., Ed. (Springer-Verlag, New York, 1979), pp. 115.

63 Xu, S.; Miller, C. C.; Dol, S. J.; Gao, Y.; Mantell, D. A.; Mason, M. G.; Muenter, A. A.; Sharp, L. I.; Parkinson, B. A. and MIller, R. J. D. *Chem. Phys. Lett.* **272,** 209 (1997).

CHAPTER 2

Growth and Characterization of Single Crystal SnS_2

INTRODUCTION

A major portion of this thesis was focused on studying the mechanism of dye sensitization. Choosing a proper substrate to study the mechanism of electron injection from an excited dye state to the conduction band of a semiconductor was extremely important. Single crystal SnS_2 has distinct properties that make it conducive to studying such photoelectrochemical processes as dye sensitization. Because SnS_2 is a two dimensional semiconductor, it has atomically smooth surfaces that are easily regenerated. These surfaces are convenient for surface coverage determinations and allow multiple experiments to be performed on a single crystal. Thus single crystal SnS_2 was considered a viable substrate for studying photoelectrochemical processes.

Tin disulfide is a layered compound semiconductor with the CdI_2 structure (Figure 2.1). This structure has a layer of Sn atoms sandwiched between two layers of S atoms. These SnS_2 sandwich layers are held together by van der Waals forces allowing the crystals to be easily cleaved perpendicular to

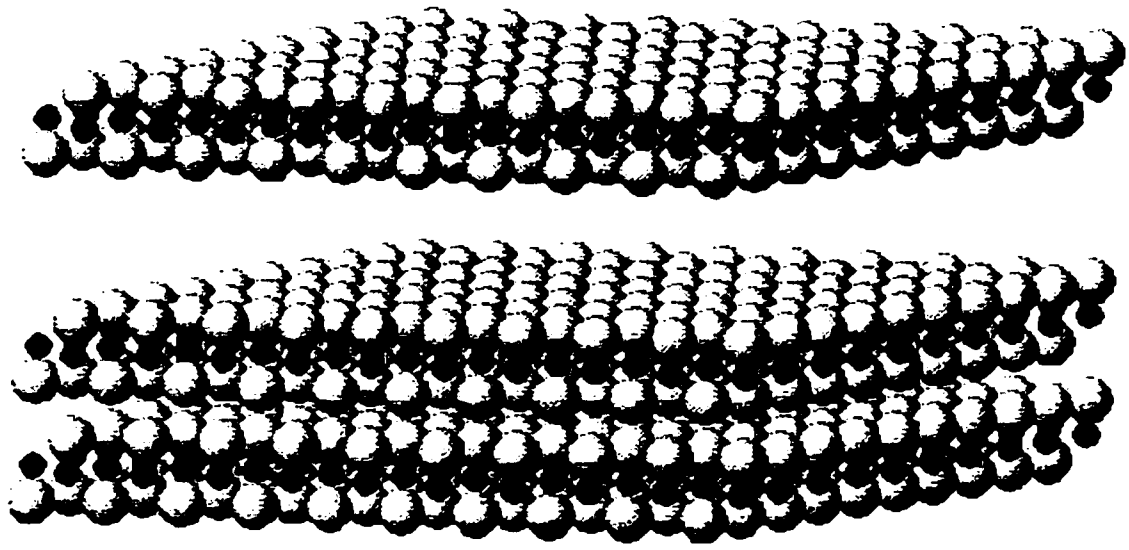

Figure 2.1. Representation of three SnS_2 layers. A single layer of SnS_2 consists of one layer of Sn atoms (larger light spheres) sandwiched between two layers of S atoms (smaller dark spheres).

the c-axis.

This material has a strong anisotropic nature and is stable in ambient air. Single crystal SnS_2 has been studied for various purposes including use as a material in lithium intercalation batteries,[1] for switching effects observed in the current-voltage behavior,[2] and as a superior substrate for epitaxial growth[3] and dye sensitization studies[4,5].

Single crystals of SnS_2 have typically been grown through normal freezing methods[6-8] or vapor deposition[9-11] while thin films have been grown with molecular beam epitaxy[3]. Because these materials are not available commercially and our studies required large quantities of bulk SnS_2, normal freezing with the Bridgman method was employed to grow crystals that were up to 6 cm long and 2 cm in diameter.[12]

The vertical Bridgman technique was feasible as SnS_2 grows congruently from the melt (Figure 2.2).[13] An atmosphere of S was maintained above the melt as the crystals were grown in closed ampoules.[14] This allowed us to exercise control over the composition and dopant concentration. We were able to grow single crystal SnS_2 with electron carrier concentrations ranging from $3x10^{15}$ to $3x10^{18}$ cm^{-3}. The electronic properties of these crystals were characterized with Hall measurements and Mott-Schottky plots and optical characteristics were studied with photoelectrochemistry. Surface analysis was achieved through Secondary Ion Mass Spectrometry (SIMS). Bulk properties were analyzed with X-ray Powder Diffraction (XRD) and Energy Dispersion Spectroscopy (EDS).

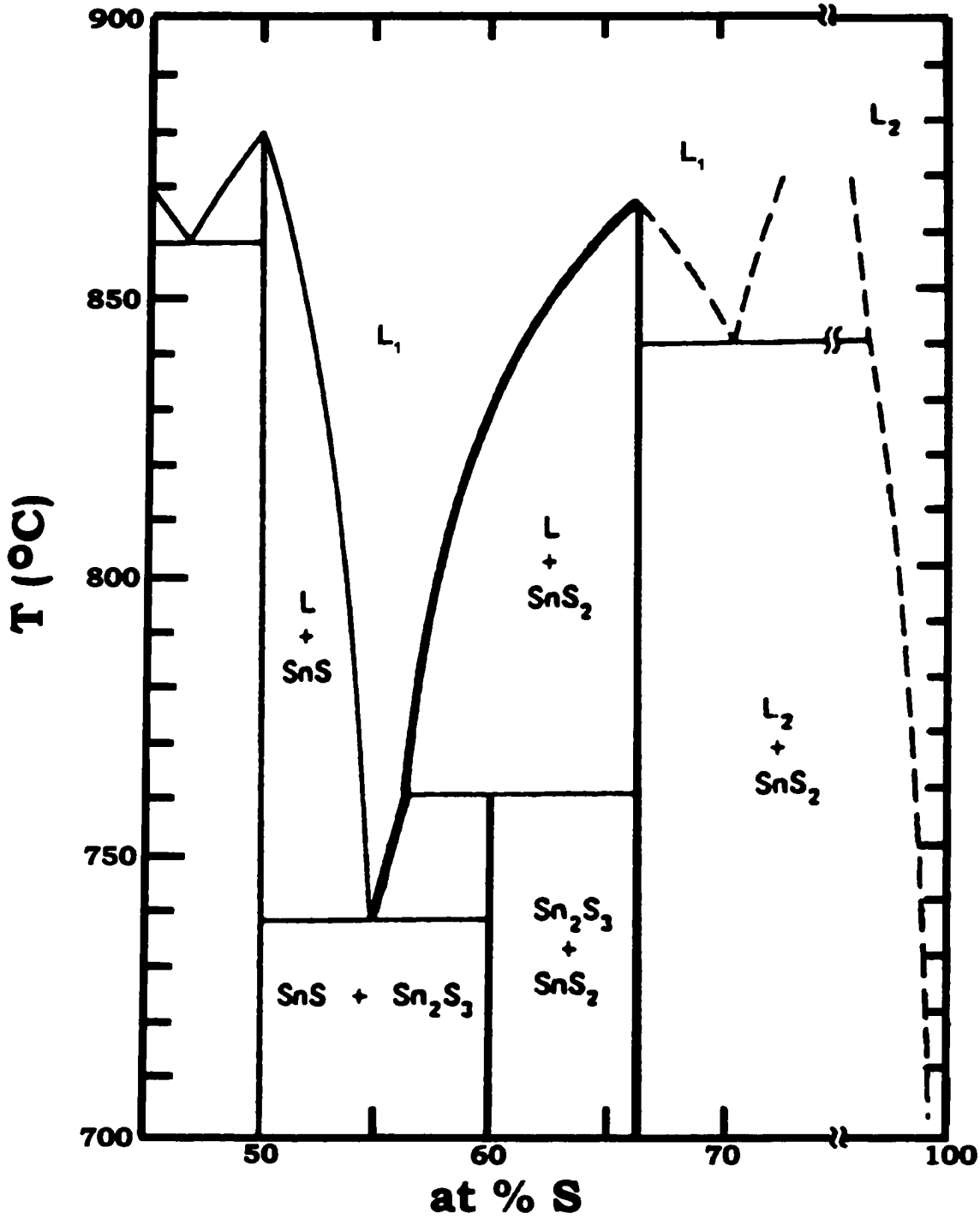

Figure 2.2. A Phase Diagram of S-Sn in the %S range where SnS_2 single crystal growth occurs. The diagram was adapted from reference 13.

BACKGROUND

Crystal growth methods are generally separated into four major categories: growth from the solid, from the melt, from the vapor, or from solution. All growth techniques are based on the principle that crystal growth commences when there is a decrease in the total free energy of the system resulting in a phase transition.[15] The free energy difference between the solid and the parent phase is the driving force for crystallization. A decrease in the free energy can occur when the dynamic equilibrium of the system is disrupted by a change in temperature, pressure, chemical potential, electrochemical potential, or strain.[16]

Preparation of single crystals requires strict control over the phase change associated with nucleation of the thermodynamically stable crystalline phase.[14] Nucleation is the precursor of crystal growth and of the overall crystallization process.[17] Once nucleation is achieved there should be a subsequent extension of the crystal to consume the remaining nutrient. Throughout crystallization a thermodynamic population of defects are created in the crystal as well as kinetic defects associated with the crystal growth rate. The creation of defects can be reduced by allowing the system to release energy to its surroundings.[16] Removal of this latent heat is an important aspect of crystal growth. Heat removal is accomplished by designing systems that generate a driving force for crystallization by creating a slight deviation of only one equilibrium parameter, such as temperature, while maintaining all others.

Semiconductor crystal growth encompasses a variety of different methods. Bulk semiconductor materials are generally produced from melt growth, solution growth or chemical vapor transport procedures. Thin films and superlattice materials are generated through epitaxial growth and vapor deposition techniques. Methods are chosen that best suit the characteristics and application of the crystal being grown. This is based on the growth kinetics, purity requirements, economics and the properties of the material itself.

The most prominent methods for bulk single crystal growth are melt growth processes including crystal pulling (Czochralski), normal freezing (Bridgman-Stockbarger) and zone melting. These methods employ a temperature gradient to advance the crystal interface and provide for latent heat dissipation. The temperature must be homogeneous throughout the melt and above that of the charge. The critical local heat flow balance at the charge-melt interface is expressed in Equation 2.1:

$$K_s G_s = R\rho_s L + K_l G_l \qquad (2.1)$$

where K is the thermal conductivity, G is the temperature gradient, R is the growth rate, ρ is the density, L is the latent heat of fusion, and subscripts s and l denote solid and liquid, respectively.[18] This equation reveals the relationship between the latent heat of fusion and the temperature gradient, as well as belays the importance of establishing a well defined temperature profile.

Melt growth techniques can be further divided as conservative and nonconservative. The former involves charge solidification until all the starting

material is consumed while the latter entails the continual addition of starting material to the melt. Conservative processes of melt growth, where there is unidirectional solidification, yield an impurity concentration (C_S) distribution given by the normal freeze equation (Eqn. 2.2):

$$C_S = k_0 C_0 (1-g)^{k_0 - 1} \tag{2.2}$$

where g is the fraction of the melt solidified, k_0 is the distribution coefficient and C_0 is the initial impurity concentration. While the nonconservative melt growth processes generate a crystal with an impurity distribution along the X axis as seen in the zone melting equation (Eqn. 2.3):

$$C_S = C_0[1-(1-k_0)\exp(-k_0 X/L)] \tag{2.3}$$

where L is the zone length. The degree of purification is greater with normal freezing. However, with repetitive cycles of zone melting, high purity crystals are produced from both techniques.[14]

Optimal growth conditions require thermal and mechanical stability for bulk single crystal growth from the melt. These requirements must be observed when choosing a drop rate for the ampoule as it passes through the temperature gradient. The drop rate must provide an adequate growth rate; steeper gradients usually allow for faster drop rates. Furthermore, the growth of single crystals from the melt requires no decomposition before melting and no phase transition between the melt and room temperature.[19]

The three most widely used methods as mentioned previously for the growth of bulk single crystals from the melt are Czochralski, Bridgman-

Stockbarger and floating zone. High-purity silicon is predominately grown using the Czochralski method while silicon with a lower oxygen content is grown by the float zone technique. The Bridgman-Stockbarger method is rarely used to grow silicon, but is frequently used as a source of single crystal GaAs.[20]

The remainder of this chapter will be dedicated to the Bridgman-Stockbarger growth method. This technique allows both the shape and size of the crystal to be manipulated and the atmosphere above the melt to be controlled by the incorporation of a closed ampoule.[19] Disadvantages include the need for an inert crucible and the requirement that there is no crystal expansion upon solidification.[21] There are several variations on this technique, but the basic principle involves a melt passing through a freezing plane. A constriction at the tip of the ampoule is incorporated to force crystal growth in a single orientation. The temperature gradient and growth rate must be optimized to obtain high purity crystals.

The data presented in the following sections are my own work. I grew the SnS_2 single crystals and accomplished Hall, Mott-Schottky, XRD and EDS measurements. Dr. Soltz, a post doctoral fellow in our laboratory, repeated Hall and Mott-Schottky measurements and obtained similar results. SIMS measurements were performed at Hewlett Packard with the assistance of Terry Potts, a senior technical director.

EXPERIMENTAL METHODS

Single Crystal Growth. Stoichiometric quantities of high purity Sn (puratronic, Alfa Æsar), S (puratronic, Alfa Æsar) with <1 mole % of dopants, Cl_2 as $SnCl_4$ (5N, Alfa Æsar), P (5N, Strem), Se (5N, Alfa Æsar) or As (5N, Alfa Æsar) were introduced to the thick walled (3 mm) quartz ampoules under an atmosphere of nitrogen. Table 2.1 lists the elements and the mole percentages added for each boule of SnS_2 grown.

Ampoules were approximately 16 cm by 2.5 cm with one end tapered to promote single crystal growth. After loading the ampoules they were evacuated to approximately 10^{-6} torr and sealed under vacuum. The charge was prebaked in a Thermcraft horizontal single zone tube furnace at 750°C for 168 hours to allow the charge to react.

After the prebake, single crystals of SnS_2 were grown in a Dynatherm vertical Bridgman furnace equipped with a sodium isothermal furnace liner (Dynatherm 11-14-06) as shown in Figure 2.3. There are two zones in the Bridgman furnace, each 6 inches in length, separated by a 1 inch insulating spacer. The upper or "hot" zone was equipped with a sodium isothermal furnace liner to provide homogeneous temperature control throughout the entire zone. The temperature profile of the furnace is depicted in Figure 2.4. The profile shows the superior temperature uniformity of the "hot" zone (870°C) as compared to the "cold" zone (680°C).

Bridgman growth proceeded when prebaked ampoules were placed in the

Table 2.1. Growth parameters of single crystal SnS_2 doped with $SnCl_4$, Se, As or P.

Run #	Mole % of Dopant Added	Mole % of excess S
8	0.0416 Cl	--
9	0.0747 Cl	--
10	0.340 Cl	--
12	0.410 Cl	0.454
13	3.92 Cl	--
14	0.3317 Se	0.6650
15	0.3312 As	0.6625
16	1.024 P	--
17	0.0412 Cl	0.6826
18	0.411 Cl	0.8670

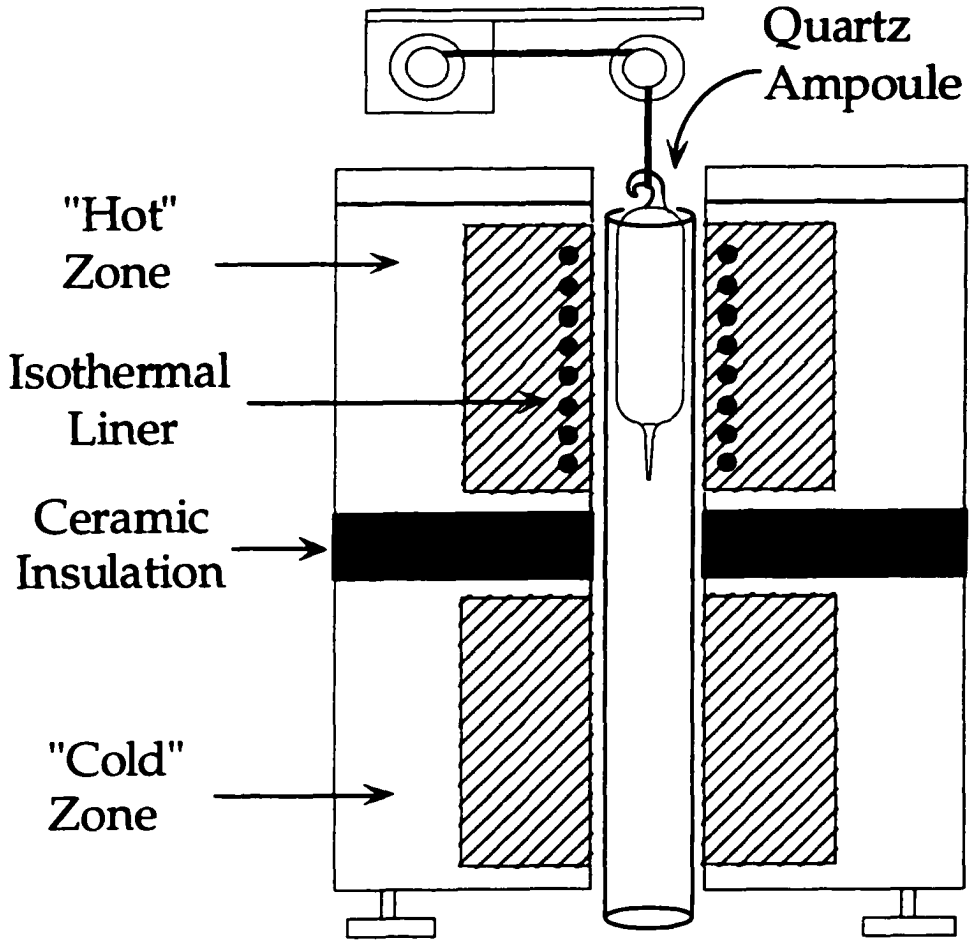

Figure 2.3. Ampoules are slowly lowered from the "hot" zone to the "cold" zone in a vertical Bridgman furnace to promote single crystal growth.

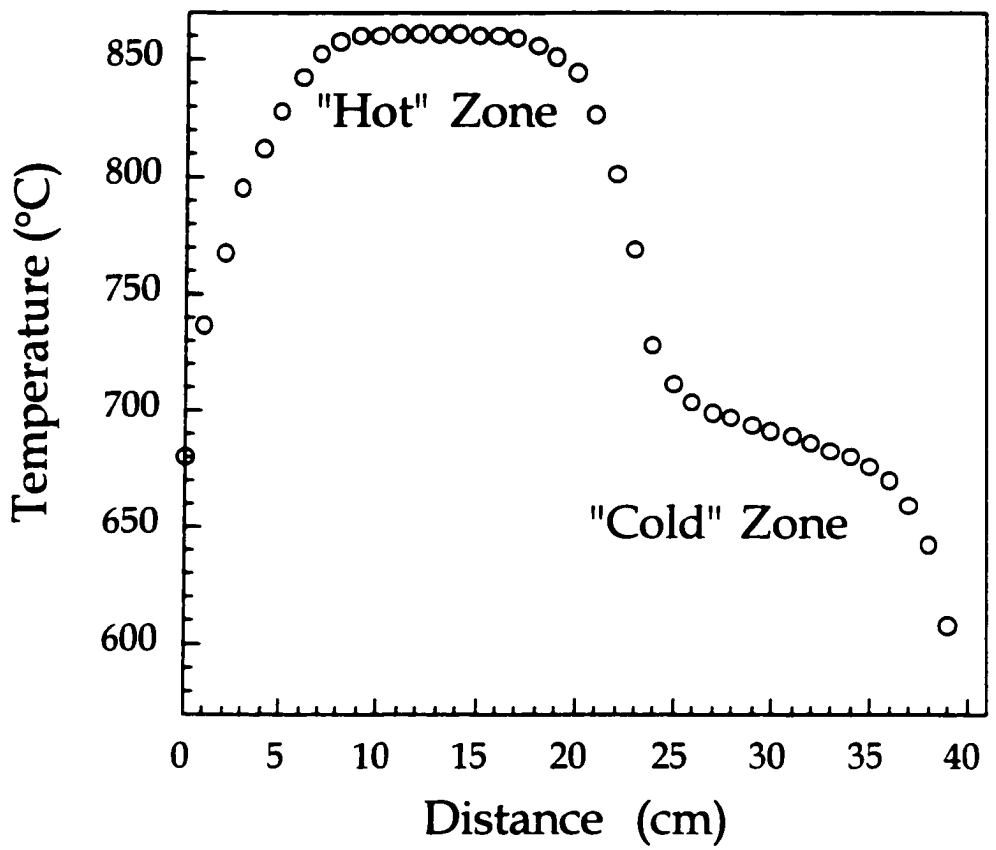

Figure 2.4. A plot of Temperature vs. Distance down the center of a vertical Bridgman furnace.

"hot" zone and subsequently lowered from the "hot" zone, above the melting temperature of SnS_2 into the "cold" zone, below the melting point of SnS_2. The ampoule was then allowed to cool to room temperature. The lowering rate of the ampoule through the furnace was approximately 2 cm/day.

Characterization of Single Crystal SnS_2. Electrical properties were determined through Hall and Mott-Schottky measurements. Samples for Hall measurements were contacted with evaporated In or sputtered Au to which Ag wire was attached with Ag paste (SPI Supplies®). Hall measurements were carried out at room temperature, in air, on a locally designed and built instrument. A PC-controlled power supply provided a constant current to the terminals of the samples with the voltage measured by a precision digital multimeter (HP 3488A). The constant current ranged from 0.1 - 1 mA depending on the SnS_2 crystal run. The magnitude of the magnetic field at the sample was held constant at 1400 Gauss.

SnS_2 electrodes, shown in Figure 2.5, were prepared for Mott-Schottky and photoelectrochemical measurements by mounting approximately 1 mm thick and 1 cm^2 pieces of single crystal SnS_2 onto Cu disks with Ag paste (SPI Supplies®). The Cu disks had Cu wire soldered to the opposite side that was fed through a glass tube, bent 90° at one end. The disk was pressed against the bent end of the tube and epoxied (Epoxy-Patch®) in place. Sealant (Dow Corning 732) was used to isolate the Cu disk and SnS_2 edges from solution.

All photoelectrochemical and Mott-Schottky measurements were taken in

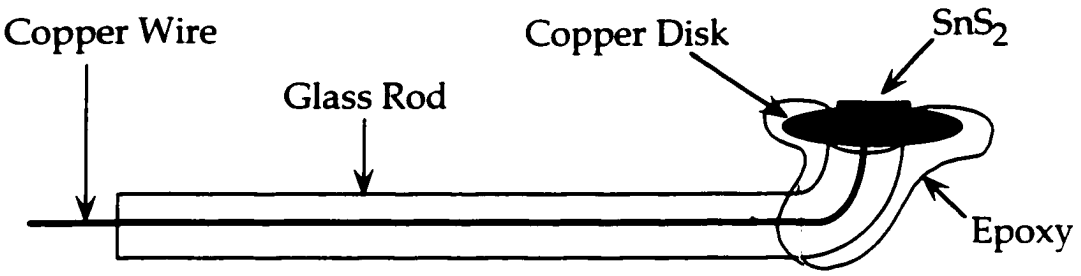

Figure 2.5. Tin disulfide electrode fabrication for photoelectrochemical measurements.

a three compartment electrochemical cell. Measurements were carried out in a 1 M LiCl/methanol electrolyte solution with a Ag/AgCl reference electrode, a Platinum counter electrode, and a semiconductor working electrode. Mott-Schottky measurements were carried out using a Princeton Applied Research 173 potentiostat, Stanford Research System 830 lock-in amplifier, HP function generator and PC computer. The data acquisition was semi-automated. The computer scanned a voltage range (forward and reverse), acquired in- and out-of-phase data from the lock-in, did a linear least-squares fit, analyzed the flat-band potential and dopant density data, and plotted, printed and stored the data on disk. Photoelectrochemical measurements were carried out in a similar three electrode cell with an optical quartz window mounted on the working electrode compartment. Monochromatic light from a Fisher Scientific Jarell-Ash Monospec 27 with a tungsten halogen lamp light source was focused onto the semiconductor surface and chopped at a rate of 28 kHz. A Princeton Applied Research 174A potentiostat, Stanford Research System 830 lock-in amplifier and PC computer were utilized to measure and record the photocurrent. The semiconductor electrode was biased 0.7 V vs Ag/AgCl for all photoelectrochemical measurements.

Crystal composition was determined with a Kevex Super 8000 energy dispersion spectrometer and a Vacuum Generators ESCA Lab 220x1-i X-ray photoelectron spectrometer. The crystal structure was analyzed with a Philips Powder X-ray Diffractometer.

RESULTS AND DISCUSSION

Electrical Properties of SnS_2. Four primary electrical properties measured to characterize semiconducting materials were resistivity, mobility, conductivity, and carrier concentration. Resistivity, ρ, can be determined with a four point probe where a small current is passed through two leads while the resistivity is monitored between the other two. Conductivity, σ, can be calculated from resistivity measurements since the two properties are inversely proportional, as seen in the following equation:

$$\sigma = \frac{1}{\rho} \tag{2.4}$$

Both the number of free charge carriers, N, and mobility, μ, are directly proportional to the conductivity, as related by Equation 2.5:

$$\sigma = Ne\mu \tag{2.5}$$

with e being the charge of an electron. Calculating the number of free carriers and the mobility of semiconductor materials was accomplished through two methods: Hall effect and Mott-Schottky measurements.

Prior to Hall measurements, the resistivity of the Hall samples was measured. This allowed corresponding resistivity, carrier concentration, and mobility to be obtained for all SnS_2 samples. The results of these measurements are listed in Table 2.2.

After the resistivity was determined, Hall effect measurements were performed. This effect occurs when an external magnetic field influences the

Table 2.2. Electrical Properties of single crystal SnS_2 as determined from Hall Effect measurements.

	Growth Parameters		Hall Effect Measurements		
Run #	Mole % of Dopant added	Mole % of excess S	Resistivity (Ω-cm)	e^- Mobility (cm^2/Vs)	Carr. Conc. ($x10^{16}$ cm^{-3})
8	0.0416 Cl	--	1.57±0.07	51±5	7.8±1
9	0.0747 Cl	--	6.04±0.03	32±1	3.2±0.1
10	0.340 Cl	--	2.24±0.01	38±1	7.3±0.1
12	0.410 Cl	0.454	1.1±0.5	18±5	37±20
13	3.92 Cl	--	0.28±0.04	21±4	109±4
14	0.3317 Se	0.6650	2.9±0.4	38±3	5.7±1
15	0.3312 As	0.6625	51±1	33±9	0.4±0.4
16	1.024 P	--	--	--	~0.001
17	0.0412 Cl	0.6826	0.815±0.005	33±2	23±1
18	0.411 Cl	0.8670	0.59±0.01	25±1	42±2

motion of charge carriers in a conductor.[22,23] This effect is depicted in Figure 2.6 for an n-type semiconductor.[20] When a steady current, I_x, flows in the positive x-direction with a current density, j_x, and a constant magnetic field, B_z, is applied normal to the surface of the semiconductor, a force ($F_L = \upsilon_x B_z e$) results that deflects electrons in the negative y-direction with a velocity, υ_x. A transverse electric field ($-E_y$), opposing the Lorentz force (F_L) is established in the positive y-direction of the semiconductor to counterbalance the charge accumulation. Thus, the two forces are in balance:

$$\upsilon_x B_z = E_y \tag{2.6}$$

Substituting in the current density, $j_x = -N\upsilon_x e$, the equation reduces to:

$$E_y = -\frac{j_x B_z}{Ne} = R_H j_x B_z \tag{2.7}$$

where the proportionality constant $R_H = \frac{1}{Ne}$ is the Hall coefficient.

The Hall field, E_y, is calculated by measuring the Hall voltage, V_H, with a high resistance voltmeter as:

$$V_H = E_y h \tag{2.8}$$

where h is the sample width.[24] Thus the Hall coefficient can be determined, providing that both the magnetic field strength and current density are known. Since the Hall coefficient is directly related to N, the carrier concentration can also be established. Furthermore, the type of carrier, n or p, is ascertained as the sign of the charge carrier affected the value of the Hall coefficient.

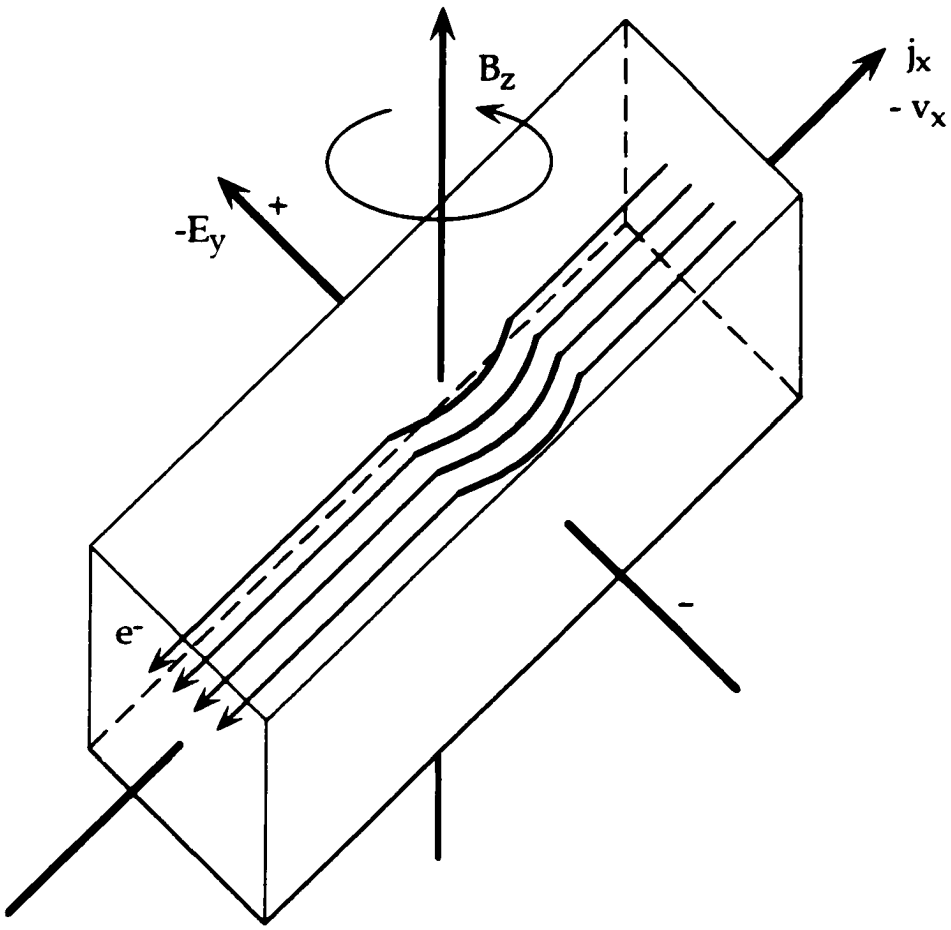

Figure 2.6. Schematic of the Hall effect. A constant magnetic field, B_z, is applied normal to the current density, j_x, creating a force, F_L, in the negative y-direction with an opposing Hall field, $-E_y$. By measuring the resulting Hall voltage along the y-axis the carrier concentration can be calculated.

In addition to calculating the carrier concentration, the mobility is obtained through Hall measurements. Substituting the Hall coefficient into Equation 2.5 yields:

$$R_H \sigma = \mu \tag{2.9}$$

Combining Hall effect and conductivity measurements allows the mobility to be determined. Both mobility and charge carrier concentrations determined from these calculations are listed in Table 2.2.

Carrier concentration was independently determined through a second method with Mott-Schottky plots. The Mott-Schottky equation relates capacitance to carrier concentration, N, through the relationship:[25]

$$\frac{1}{C^2} = \frac{2}{q\varepsilon N}\left(\frac{\Delta E}{q} - V\right) \tag{2.10}$$

where C is the capacitance, q is the charge of an electron, ε is the dielectric constant of the semiconductor, ΔE is the change in the potential energy, and V is the applied potential. A plot of the inverse square of the capacitance as a function of applied voltage yields a linear relationship, as seen in Figure 2.7, with the voltage intercept equal to the flat band potential and the slope inversely proportional to the doping density.[26] Comparing Table 2.2 and 2.3 shows the carrier concentrations determined from both methods were in close agreement. Both Hall and Mott-Schottky measurements revealed the SnS_2 crystals were all n-type.

Mott-Schottky measurements were further analyzed to determine the flat

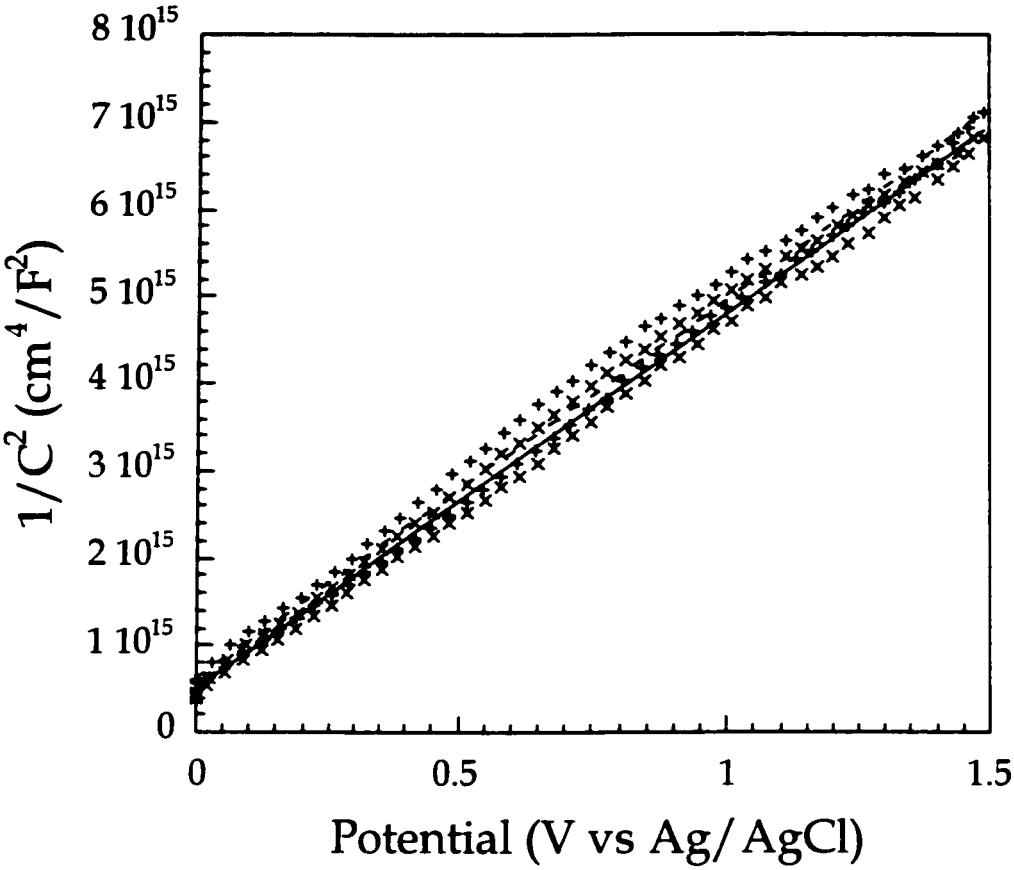

Figure 2.7. Mott-Schottky plots of Run 12 at two frequencies, 10 kHz (x) and 20 kHz (+). The slope of the line is inversely proportional to the carrier concentration.

Table 2.3. Electrical Properties of single crystal SnS_2 as determined from Mott-Schottky measurements.

	Growth Parameters		Mott-Schottky	
Run #	Mole % of Dopant added	Mole % of excess S	Carr. Conc. ($x10^{16}$ cm^{-3})	Flat Band Pot. (V vs Ag/ AgCl)
8	0.0416 Cl	--	0.6±0.09	+ 0.06±0.05
9	0.0747 Cl	--	4±1	+ 0.002±0.181
10	0.340 Cl	--	9±4	+ 0.05±0.03
12	0.410 Cl	0.454	130±17	+ 0.030±0.02
13	3.92 Cl	--	310±100	+ 0.08±.05
14	0.3317 Se	0.6650	5±4	- 0.003±0.127
15	0.3312 As	0.6625	0.27±0.06	- 0.1±0.1
17	0.0412 Cl	0.6826	5.6±0.6	- 0.07±0.03
18	0.411 Cl	0.8670	74±11	- 0.05±0.09

band potential. Increasing the S concentration in the crystal appears to move the flat band potential more negative as shown by Table 2.3. This shift in the potential occurs as the electrode surface becomes more negative as a result of the increased S content in the crystals. A similar effect was observed by Katty et al.[27] in aqueous solution. The effects of dopant concentration on flat band potential were different for Se and As (Table 2.3).

The variation of dopant concentration throughout the SnS_2 single crystals was determined for several chlorine doped samples with Hall measurements. A diagram showing a typical dopant profile of Run 8 is shown in Figure 2.8. The chlorine content appears to remain constant throughout the bulk of the crystal, although there are slight decreases in the chlorine concentrations at the top and bottom of the crystal. Resistivity shows a similar trend, however, higher values were observed at the top and bottom of the crystals measured, consistent with the lower dopant concentrations.

A decrease in resistivity with increasing chlorine concentration was previously noted by Kourtakis et al.[9] who suggested that the chlorine impurity was solely responsible for the donor states that lie slightly below the conduction band. Their work revealed that when the S content was slightly below stoichiometric proportions for physical vapor transport (PVT), low resistivity SnS_2 crystals were produced. This work has been supported by Arora et al.[10] who observed similar results for chemical vapor transport (CVT) crystals of SnS_2. Even though a decrease in resistivity can be associated with S content as opposed

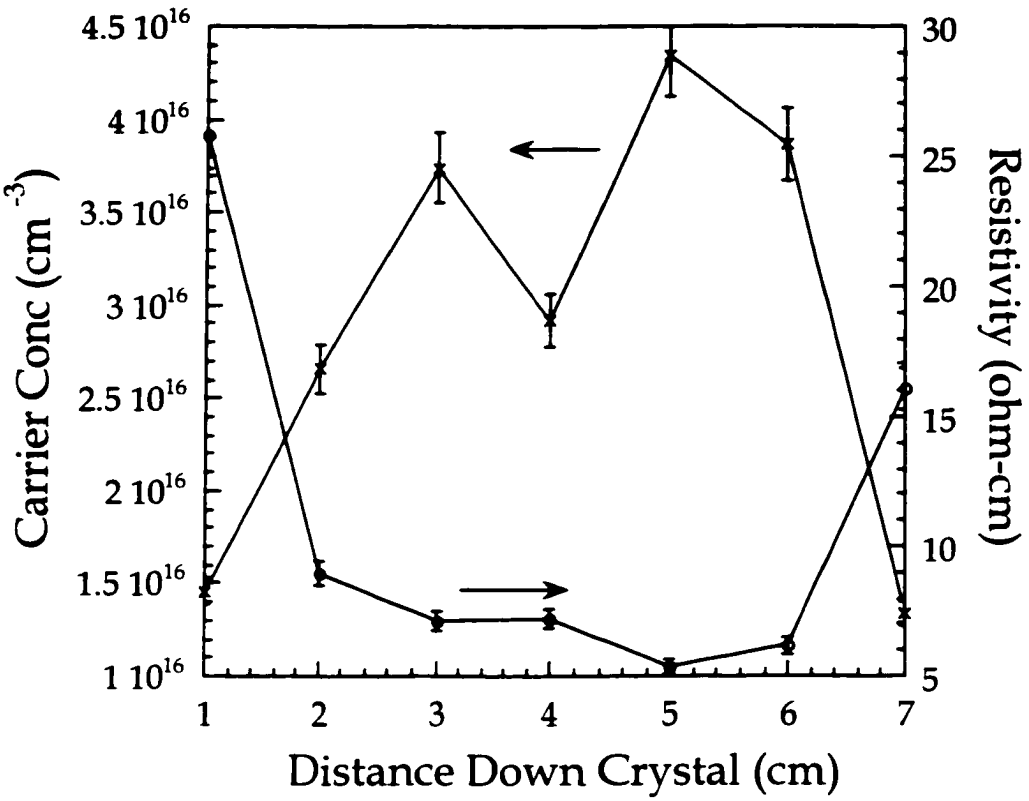

Figure 2.8. Depth profile of carrier concentration and resistivity going down a piece SnS_2 single crystal from Run 8. The arrows indicate which axis the data points along the lines correlate to in the diagram.

to carrier concentration, research has shown that conductive SnS_2 single crystals require the addition of dopant atoms.[7] Therefore, the presence of chlorine in the SnS_2 single crystals grown was confirmed with SIMS.

Similar to resistivity, the electron mobility was seen to change with carrier concentration. Increasing the carrier concentration led to a decrease in electron mobility. This may affect the dye sensitization current as Nakao et al.[28] observed that greater quantum efficiencies were associated with larger electron mobilities for rhodamine B - SnO_2 and - ZnO_2 systems.

Bulk Analysis of SnS_2. X-ray powder diffraction was used to verify the SnS_2 crystal structure. Several polytype structures, that are the same in two dimnesions but different in the third, exist for SnS_2 and the relative stability of specific polytypes is unknown at present.[29] Our SnS_2 single crystals, grown through the Bridgman technique, revealed that variations in the carrier concentration had no effect on the polytypes. All SnS_2 crystals grown were comprised of more than one polytype.

Elemental analysis through EDS revealed stoichiometric quantities of Sn and S were present for all SnS_2 single crystals grown to an accuracy of ±1%. Atomic percents from EDS were 64.57 (S), 33.90 (Sn) and 1.53 (Cl) for Run 13. Both SIMS and EDS confirmed the presence of dopant atoms in the crystal.

Incident Photon to Current Efficiencies. Photoelectrochemical measurements were used to determine the efficiency of SnS_2 single crystals towards converting light into electrical energy. By applying a bias, an electric

field gradient referred to as the space charge region, was established at the semiconductor surface. This allowed the separation of electron-hole pairs generated in this region by irradiating the surface with light of energy equal to or greater than the band gap (560 nm or 2.2 eV).[30] The quantum yield for the incident photon to current efficiency (IPCE or Φ) was calculated from Equation 2.11:

$$\Phi = \frac{j_P E}{I} \tag{2.11}$$

where j_P is the photocurrent, E is the photon energy in eVs and I is the photon flux.

The IPCE was plotted vs wavelength in Figure 2.9 to investigate the correlation between various SnS_2 crystals and quantum efficiency. From these plots it was determined that at longer wavelengths, chlorine doped SnS_2 crystals with higher carrier concentrations displayed larger IPCEs. This was confirmed by Powell[31] who noted in previous work that the presence of impurities in SnS_2 crystals created a relatively high absorption tail extending to lower energies.

The IPCE data was further analyzed to confirm the SnS_2 band gap energy and the type of electronic transition, indirect or direct. Because the IPCE dropped below 0.1% at approximately 560 nm, which is the band gap energy of SnS_2,[32] the electron transition was predicted to be indirect. In addition, the SnS_2 absorption coefficient[32], α, was 143 cm^{-1} at 560 nm with a penetration depth of 6.99×10^{-3} cm that corresponds to the indirect band gap edge of SnS_2[30]. Plotting

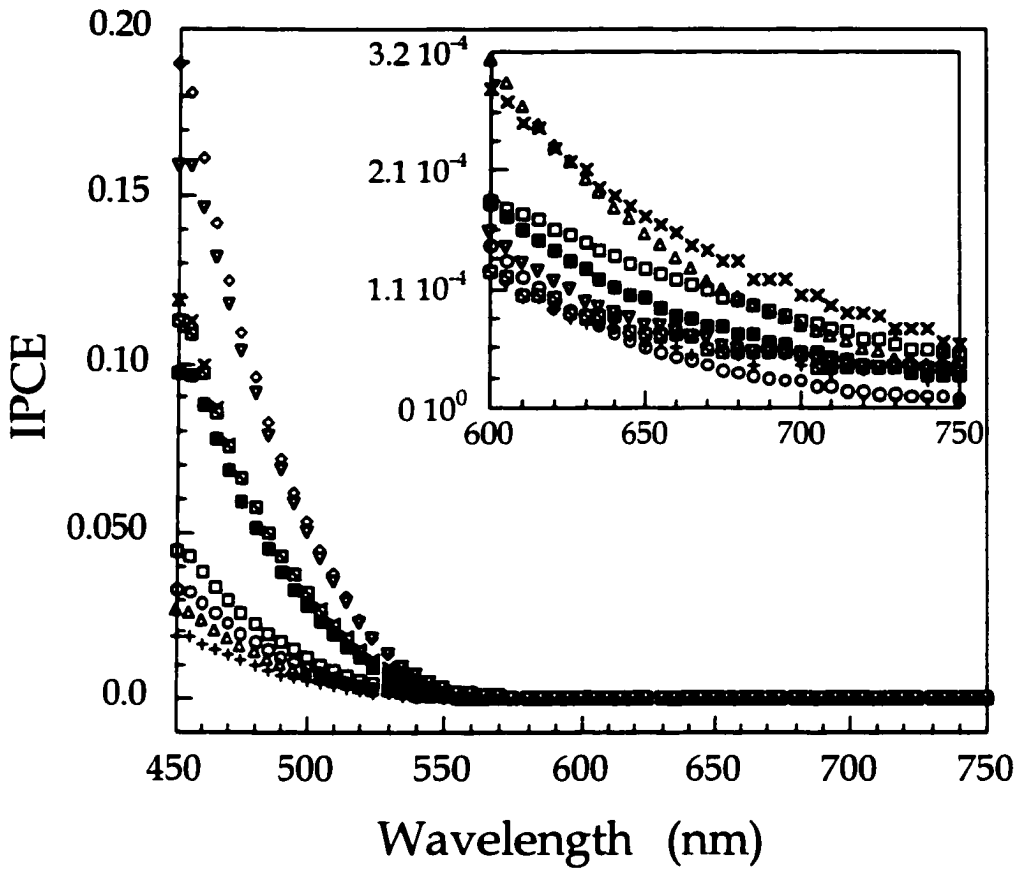

Figure 2.9. IPCE vs wavelength dependence for various SnS_2 runs. The SnS_2 carrier concentrations from Table 2.2, in units of $x10^{16}$ cm^{-3} Cl (unless otherwise noted) are; 109 (+), 42 (o), 37 (Δ), 23 (□), 7.8 (∇), 7.3 (⧅), 5.7 Se (x), 3.2 (⊞) and 0.4 As (◊). The SnS_2 electrodes were biased 0.7 V vs Ag/AgCl reference electrode in a 1M LiCl/methanol solution.

$(\Phi h\nu)^{1/2}$ vs $(h\nu)$ for an indirect transition material yields a linear relationship with the intercept of the photon energy axis being the band gap edge. The values obtained experimentally, 2.2 eV for all SnS_2 crystals, agree with the literature.[30,32-34]

The width of the space charge region was calculated to determine if a correlation with carrier concentration existed. The space charge widths, W, listed in Table 2.4 were tabulated from Equation 2.12:

$$W = \left(\frac{2\varepsilon\varepsilon_o V_{FB}}{eN_D} \right)^{1/2} \tag{2.12}$$

with ε as the dielectric constant, ε_o the permittivity of free space, e the elementary charge, N_D the donor concentration, and V_{FB} the flat band potential of the semiconductor. Values obtained for the width of the space charge region ranged from 0.0162 - 0.121 μm as shown in Table 2.4. These values increased with decreasing carrier concentration. It was predicted that the width of the space charge region would affect the area in which electrons could be collected since recombination readily occurs when electron hole pairs are generated outside of the space charge region.

Photocurrent collected from wavelengths outside the space charge region depended on the minority (hole) carrier diffusion length, L_p. The hole diffusion lengths are listed in Table 2.4. The values were calculated from the Gärtner model.[35]

Table 2.4. Space charge width and diffusion length of single crystal SnS_2.

Run #	Mott-Schottky Carr. Conc. ($x10^{16}$ cm^{-3})	Space Charge Width (μm)	Diffusion Length (μm)
8	0.6±0.09 Cl	0.407	0.121
9	4±1 Cl	0.134	0.0694
10	9±4 Cl	0.142	0.0770
12	130±17 Cl	0.0655	0.0202
13	310±100 Cl	0.0383	0.0171
14	5±4 Se	0.185	0.0842
15	0.27±0.06 As	0.632	0.121
17	5.6±0.6 Cl	0.0784	0.0462
18	74±11 Cl	0.0591	0.0142

$$j_P = eI\left[\left(1-\frac{1}{1+\alpha L_P}\right)exp(-\alpha W)\right] \quad (2.13)$$

Assuming space charge layer effects can be neglected ($\alpha W << 1$) Equation 2.13 reduces to:

$$\frac{1}{\Phi} = \frac{1}{\alpha L_P} + 1 \quad (2.14)$$

A plot of $1/\Phi$ vs. $1/\alpha$, Figure 2.10, yielded straight lines with the slopes proportional to $1/L_P$.[36] Similar values were obtained when analyzing current voltage curves taken at a single wavelength. Graphs of - $\ln(1-\Phi)$ vs $(V-V_{FB})^{1/2}$ were linear with the slope being proportional to L_P and yielded values that agreed with the results obtained from Figure 2.10.[37]

CONCLUSION

Single crystals of SnS_2 intentionally doped with Cl, As, Se, and P were successfully grown through the Bridgman method. Carrier concentrations measured through the Hall effect and Mott-Schottky measurements were in good agreement. Increasing the quantity of dopants introduced in to the ampoule increased the carrier concentration in the single crystals grown. Samples doped with equivalent concentrations of Se, As, and Cl displayed similar carrier concentrations. On the other hand, introduction of P at a larger concentration than As, Se, and Cl resulted in a much smaller carrier concentration. This probably reflects the lower solubility of P in SnS_2 compared to the other dopants used in this study.

Chlorine concentration as a function of distance was obtained from depth

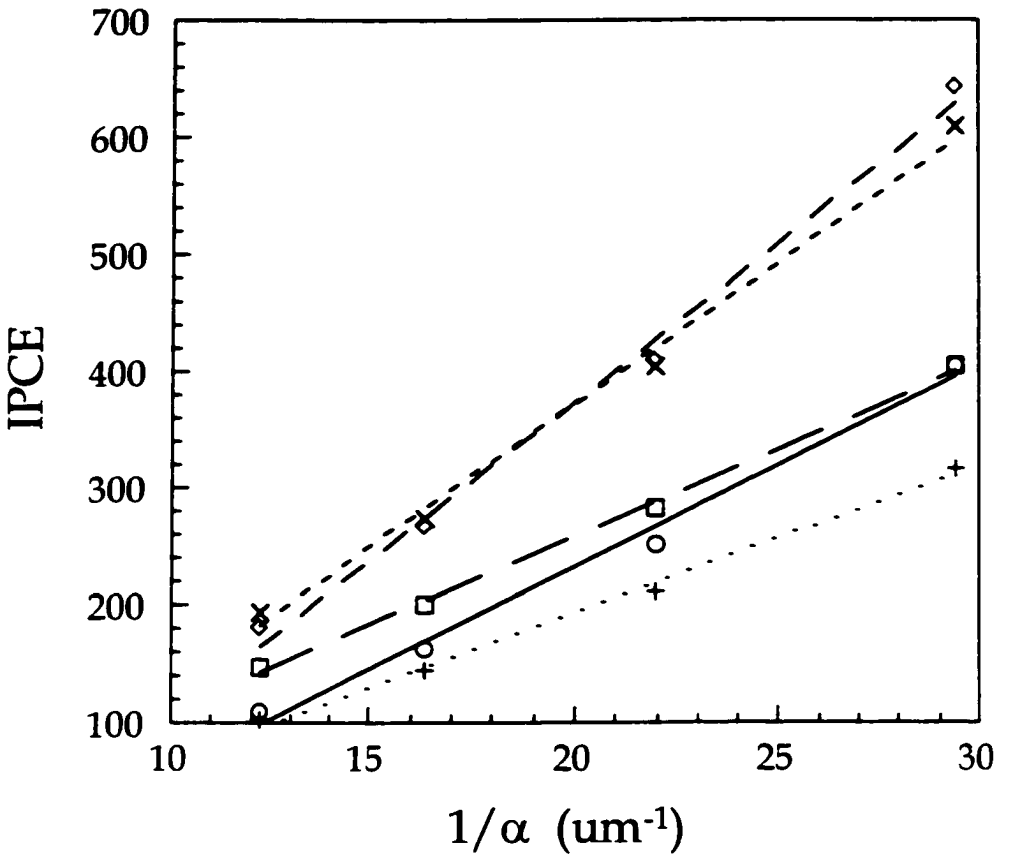

Figure 2.10. Minority carrier diffusion length (μm) determination for photogenerated holes in SnS_2 Runs; 15 (o), 14 (□), 10 (◊), 9 (x) and 8 (+). The SnS_2 electrodes were biased 0.7 V vs Ag/AgCl reference electrode in a 1M LiCl/methanol solution.

profile analysis on Cl-doped SnS_2. It was found that the Bridgman growth technique yielded SnS_2 crystals with uniform carrier concentrations throughout the middle section of the crystals. The chlorine concentration decreased two-fold at the bottom of the charge, near the tip, which is in agreement with studies published by Lawson and Nielsen[21]. Furthermore, it was possible to prepare crystals that spanned a wide range of Cl carrier concentrations.

The effect of Cl doping on resistivity and carrier mobility was analyzed. Both resistivity and carrier concentration were found to depend inversely on Cl concentration. In the case of Se, As, and P, no such correlation was studied as only one dopant concentration was used for each element.

Variations in the S concentration affected both the carrier concentration and the flat band potential. The S concentration was controlled through the amount of S initially added to the ampoule. From Hall and Mott-Schottky data tabulated in Table 2.2 and 2.3, an excess of S corresponds to a higher carrier concentration. However, increasing the amount of excess S does not ultimately increase the carrier concentration. The correlation between the Cl carrier concentration and the addition of excess S may be linked to a more defect free lattice, allowing for increased Cl intercalation.

In addition to affecting the Cl concentration, the S concentration also influenced the flat band potential. While there was a significant amount of fluctuation in the flat band potentials recorded, an increase in the S concentration correlated to a decrease in the flat band potential. This decrease in the potential

was presumably affected by the excess negative charge associated with the incorporation of increased S.

Analysis of the photocurrent data revealed a direct correlation between the carrier concentration, the minority carrier diffusion length, and the IPCE. As discussed previously, the minority carrier diffusion length increased as the Cl carrier concentration decreased. At wavelengths of energy greater than the band gap, the IPCE decreased with increasing Cl concentration and increased with increasing minority carrier diffusion lengths. This occurred because fewer electron hole pairs generated outside the space charge region recombine when the minority carrier diffusion length is large and are, therefore, collected as photocurrent.

REFERENCES

1 Yamaki, J. and Yamaji, A. *Physica* **105B,** 466 (1981).

2 Rimmington, H. P. B.; Balchin, A. A. and Tanner, B. K. *J. Crystal Growth* **15,** 51 (1972).

3 Schlaf, R.; Louder, D.; Lang, O.; Pettenkofer, C.; Jaegermann, W.; Nebesny, K. W.; Lee, P. A.; Parkinson, B. A. and Armstrong, N. R. *J. Vac. Sci. Technol., A* **13,** 1761 (1995).

4 Parkinson, B. A. *Langmuir* **4,** 967 (1988).

5 Xu, S.; Miller, C. C.; Dol, S. J.; Gao, Y.; Mantell, D. A.; Mason, M. G.; Muenter, A. A.; Sharp, L. I.; Parkinson, B. A. and MIller, R. J. D. *Chem. Phys. Lett.* **272,** 209 (1997).

6 Buck, P., In *Preparation and Crystal Growth of Materials with Layered Structures*, Vol. 1, 1st ed., Lieth, R. M. A., Ed. (D. Reidel Pub. Co., Dordrecht, 1977), pp. 255.

7 Katty, A.; Fotouhi, B. and Negard, N. L. *Sol. St. Chem.* **309,** 1149 (1989).

8 Julien, C.; Eddrief, M.; Samaras, I. and Balkanski, M. *Mat. Sci. and Eng.* **B15,** 70 (1992).

9 Kourtakis, K.; DiCarlo, J.; Kershaw, R.; Dwight, K. and Wold, A. *J. Sol. St. Chem.* **76,** 186 (1988).

10 Arora, S. K.; Patel, D. H. and Agarwal, M. K. *J. Mat. Sci.* **29,** 3979 (1994).

11 Shibata, T.; Muranushi, Y.; Miura, T. and Kishi, T. *J. Phys. Chem. Solids* **52,** 551 (1991).

12 Hurle, D. T. J., In *Crystal Growth: An Introduction*, Vol. 1, Hartman, P., Ed. (American Elsevier Pub. Co., Inc., New York, 1973), pp. 531.

13 Mikkelsen, J. C. *J. Crystal Growth* **49,** 253 (1980).

14 Hurle, D. T. J., In *Crystal Growth: A Tutorial Approach*, Vol. 2, 1st ed., Bardsley, W., Hurle, D. T. J., and Mullin, J. B., Eds. (North-Holland Pub. Co., Amsterdam, 1979), pp. 91.

15 Brice, J. C. *The Growth of Crystals from Liquids*, Vol 12, 1st ed. Wohlfarth, E. P., Ed., Series of Monographs on Selected Topics in solid State Physics (North-Holland Series in Crystal Growth, New York, 1973).

16 Pamplin, B. R., In *International Series on the Science of the Solid State*, Vol. 16, 2nd ed., Pamplin, B. R., Ed. (Pergamon Press Inc., Elmsford, 1980), pp. 609.

17 Toschev, S., In *Crystal Growth: An Introduction*, Vol. 1, 1st ed., Hartman, P., Ed. (American Elsevier Pub. Co., Inc., New York, 1973), pp. 531.

18 Carruthers, J. R., In *Crystal Growth: A Tutorial Approach*, Vol. 2, 1st ed., Bardsley, W., Hurle, D. T. J., and Mullin, J. B., Eds. (North-Holland Pub. Co., Inc., Amsterdam, 1979), pp. 157.

19 Gatos, H. C., In *Crystal Growth: A Tutorial Approach*, Vol. 2, 1st ed., Bardsley, W., Hurle, D. T. J., and Mullin, J. B., Eds. (North-Holland Pub. Co., Amsterdam, 1979), pp. 1.

20 Hummel, R. E. *Electronic Properties of Materials*, 2nd ed. (Springer-Verlag, Berlin, 1993).

21 Lawson, W. D. and Nielsen, S. *Preparation of Single Crystals*, Vol 1, 1st ed. Hogarth, C. A., Ed., Semi-conductor Monographs (Butterworths Scientific Pub., London, 1958).

22 Blood, P. and Orton, J. W. *The Electrical Characterization of Semiconductors: Majority Carriers and Electron States*, Vol 14, 1st ed. March, N. H., Ed., Techniques of Physics (Academic Press, Inc., San Diego, 1992).

23 McKelvey, J. P. *Solid State Physics for Engineering and Materials Science* (Krieger Pub. Co., Malabar, 1993).

24 Van der Pauw, L. J. *Philips Research Reports* **13,** 1 (1958).

25 Pankove, J. I. *Optical Processes in Semiconductors*, Vol 8, 1st ed. Holonyak, N., Ed., Solid State Physical Electronics Series (Prentice-Hall, Inc, Englewood Cliffs, 1971).

26 Turner, J. A. *J. Chem. Ed.* **60,** 327 (1983).

27 Katty, A.; Fotouhi, B. and Gorochov, O. *J. Electrochem. Soc.* **131,** 2806 (1984).

28 Nakao, M.; Itoh, K. and Honda, K. *J. Phys. Chem.* **88,** 4906 (1984).

29 Palosz, B.; Steurer, W. and Schulz, H. *Acta Cryst.* **B46,** 449 (1990).

30 Nozik, H. and Imai, I. *Physica* **105B,** 74 (1981).

31 Powell, M. J. *Solid State Phys.* **10,** 2967 (1977).

32 Domingo, G.; Itoga, R. S. and Kannewurf, C. R. *Phys. Rev.* **143,** 536 (1966).

33 Lee, P. A.; Said, G.; Davis, R. and Lim, T. H. *Phys. Chem. Solids* **30,** 2719 (1969).

34 Greenaway, D. L. and R., N. *J. Phys. Chem. Solids* **26,** 1445 (1964).

35 Gärtner, W. W. *Phys. Rev.* **116,** 84 (1959).

36 Kautek, W.; Gerisher, H. and Tributsch, H. *J. Electrochem. Soc.* **127,** 2471 (1980).

37 Fotouhi, B. and Katty, A. *Electrochimica Acta* **31,** 795 (1986).

CHAPTER 3

Sensitization Studies of SnS_2 Photoanodes with Methylene Blue, Azure B, Cresyl Violet and Oxazine

INTRODUCTION

Dye sensitization of semiconductor electrodes with large band gaps has been the subject of many investigations ranging from studies of the fundamentals of interfacial charge transport in semiconductor/electrolyte systems to solar energy conversion, as well as modeling of the photographic process.[1-5] The generally accepted kinetic model for this process involves excitation of an adsorbed dye molecule (k_{ex}) that can undergo an excited state electron transfer into the conduction band of the semiconductor (k_{inj}), as shown in Figure 3.1. The injected electron can be either efficiently separated from the oxidized dye (k_{es}) by the interfacial electric field or recombine with it ($k_{r'}$). If the electron is collected as photocurrent, the oxidized dye can then be reduced (k_{reg}) by an externally added reducing agent (regenerating agent). Other processes such as energy or electron transfer between the dye molecules could also occur with a rate constant k_{et} (not shown in Figure 3.1).

Layered metal chalcogenide semiconductors such as SnS_2, WSe_2 and

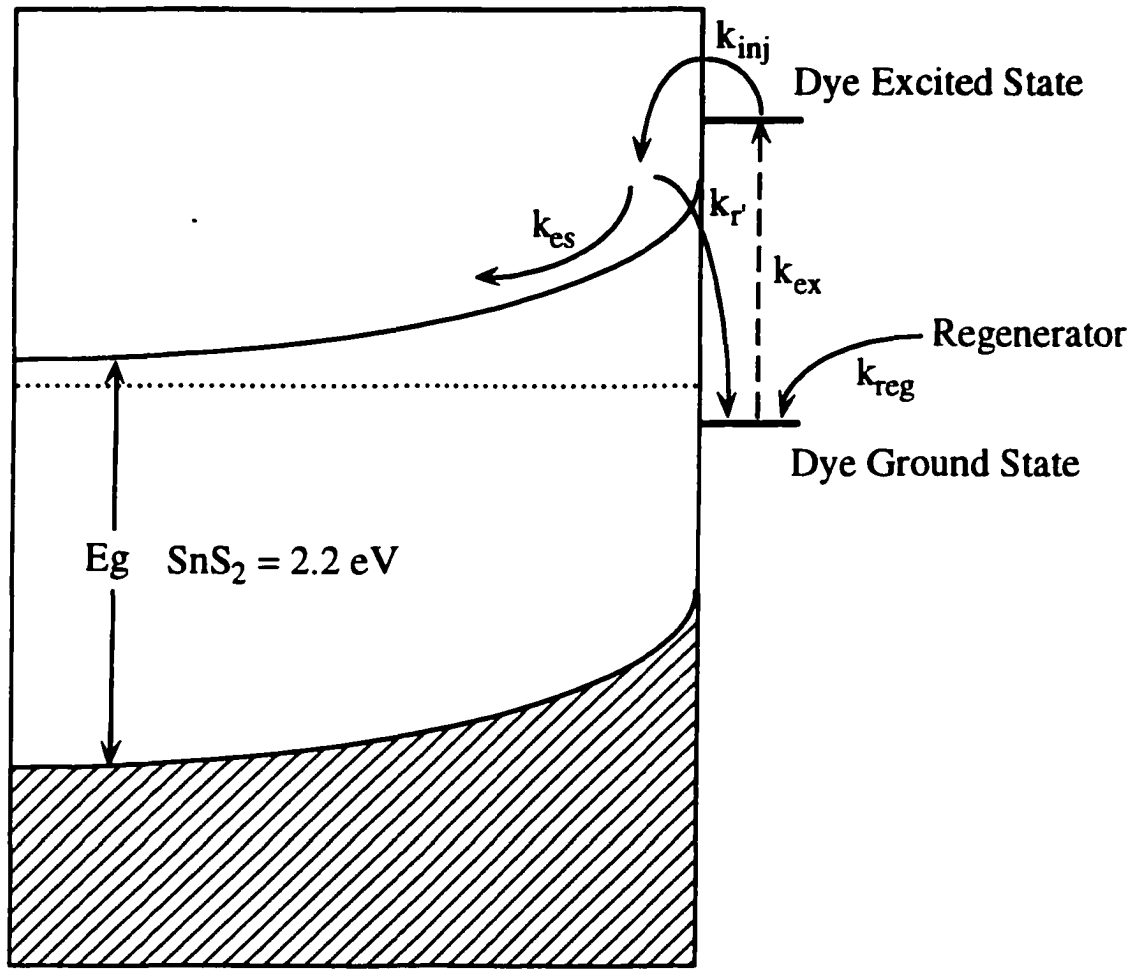

Figure 3.1. A general kinetic model for dye sensitization of SnS_2. An adsorbed dye molecule is excited from light absorption, k_{ex}, and injects an electron into the semiconductor conduction band, k_{inj}. The electron can be swept toward the semiconductor bulk by the interfacial electric field, k_{es}, and collected as photocurrent. Competing with the escape process is the recombination of the injected electron and the oxidized dye, $k_{r'}$. Oxidized dye can also be reduced by an externally added reducing agent (regenerator), k_{reg}.

$MoSe_2$, have been shown to be superior substrates for fundamental studies of dye sensitization due to high photocurrent quantum yields per absorbed photon (QYAP).[6]

The metal chalcogenide used in the subsequent studies was SnS_2. This semiconductor is built from sandwiches consisting of a S layer, a Sn layer and then another S layer as illustrated in Chapter 2 (Figure 2.1). These sandwiches stack together in a crystal with the adjacent S layers held together by weak intermolecular (van der Waals) forces. Because the sandwiches are held together by weak intermolecular forces, it is easy to cleave off sandwich layers to expose a fresh van der Waals surface for each experiment.

It has been postulated that the high dye sensitized IPCEs obtained when using layered metal chalcogenides is due to the lack of the interface states and surface contamination layers on the van der Waals surfaces since these surfaces contain no broken covalent bonds and can be freshly generated by easy cleavage.[6-8] Interface states are unavoidable on three-dimensional materials and may be responsible for assisting the recombination of the excited electrons and the holes. The recombination process is in direct competition with the collection of electrons as photocurrent, as illustrated in Figure 3.1.

The metal chalcogenide semiconductor, SnS_2 is also an excellent substrate for dye sensitization studies as it has a band gap of 2.2 eV, making a large number of dyes with absorption maxima to the red of about 565 nm suitable for these studies. This was illustrated in a previous report by Parkinson[7] where the

sensitization of SnS_2 with 30 different dyes was investigated. Despite the high QYAP for many dyes, the maximum quantum yield per incident photon (QYIP) or the incident photon to current efficiency (IPCE), remains rather low (< 1%) due to the low light absorption of a single monolayer of dye molecules. The work presented in this chapter agrees with the previous report with the exception of some very high IPCE (14%) values for methylene blue (MB^+) that were attributed to the intercalation of dye molecules into exfoliated regions near the surface.

To further analyze the dye sensitization process, the physicochemical properties of the SnS_2 substrate were carefully monitored and analyzed by measuring the sensitization efficiency of various dyes adsorbed on the SnS_2 surface. This was accomplished by growing SnS_2 crystals with various n-type doping levels to evaluate what effects both bulk properties and surface states have on dye sensitization. Then the SnS_2 crystals were sensitizated with a variety of dyes. Due to their sensitization yields, four organic dyes are emphasized in this chapter; methylene blue (λ_{max} = 680 nm), azure B (λ_{max} = 615 nm), oxazine (λ_{max} = 645 nm) and cresyl violet (λ_{max} = 634 nm). These four dyes all have absorption maxima in the visible region that are at energies below the SnS_2 band gap transition (2.2 eV or 563 nm) with little overlap in their sensitization spectra. The dye absorption maxima must be at lower energies (longer wavelengths) to be distinguished from the SnS_2 absorption spectrum. The lack of overlap in the dye sensitization spectra allows the individual dyes to

be distinguished in photoelectrochemical measurements when more than one dye is present in solution. The dye absorption maxima are also close to convenient laser lines (HeNe at 632.8 nm and a red diode at 689 nm) and these dyes all have suitable excited state energies for dye sensitization of SnS_2, however, with contrasting excited state dynamics.[9-12] Two of the dyes, cresyl violet (CV^+) and oxazine (OX^+), are known to have high fluorescence quantum yields and thus a low triplet quantum yield[9,10], whereas methylene blue (MB^+) and azure B (AZB^+) undergo rapid intersystem crossing from the singlet to the triplet excited state.[11,12] The molecular structures of all four dyes are depicted in Figure 3.2. Other dyes, including diethythiadicarbocyanine (DTTC), diethythiadcarbocyanine (DTDC), merocyanine 540 (MER), chlorophyll a (Chl a), chlorophyll b (Chl b), B chlorophyll a (B Chl a) and B chlorophyll b (B Chl b) were tested on these substrates, but IPCEs could not be detected above the noise level.

Since the electron transfer from the photoexcited dye molecules to the SnS_2 conduction band has been found to be very facile[13-15], additional aspects of the sensitization process such as the substrate composition, substrate doping density, nature of adsorption sites, dye adsorption effects on the substrate, dye adsorption isotherms, adsorption kinetics, photoxidation kinetics, regeneration kinetics, and the interactions between these parameters were investigated. Both CV^+ and MB^+ were also simultaneously adsorbed in order to investigate the possibility of selective photoxidation and possible energy or electron transfer

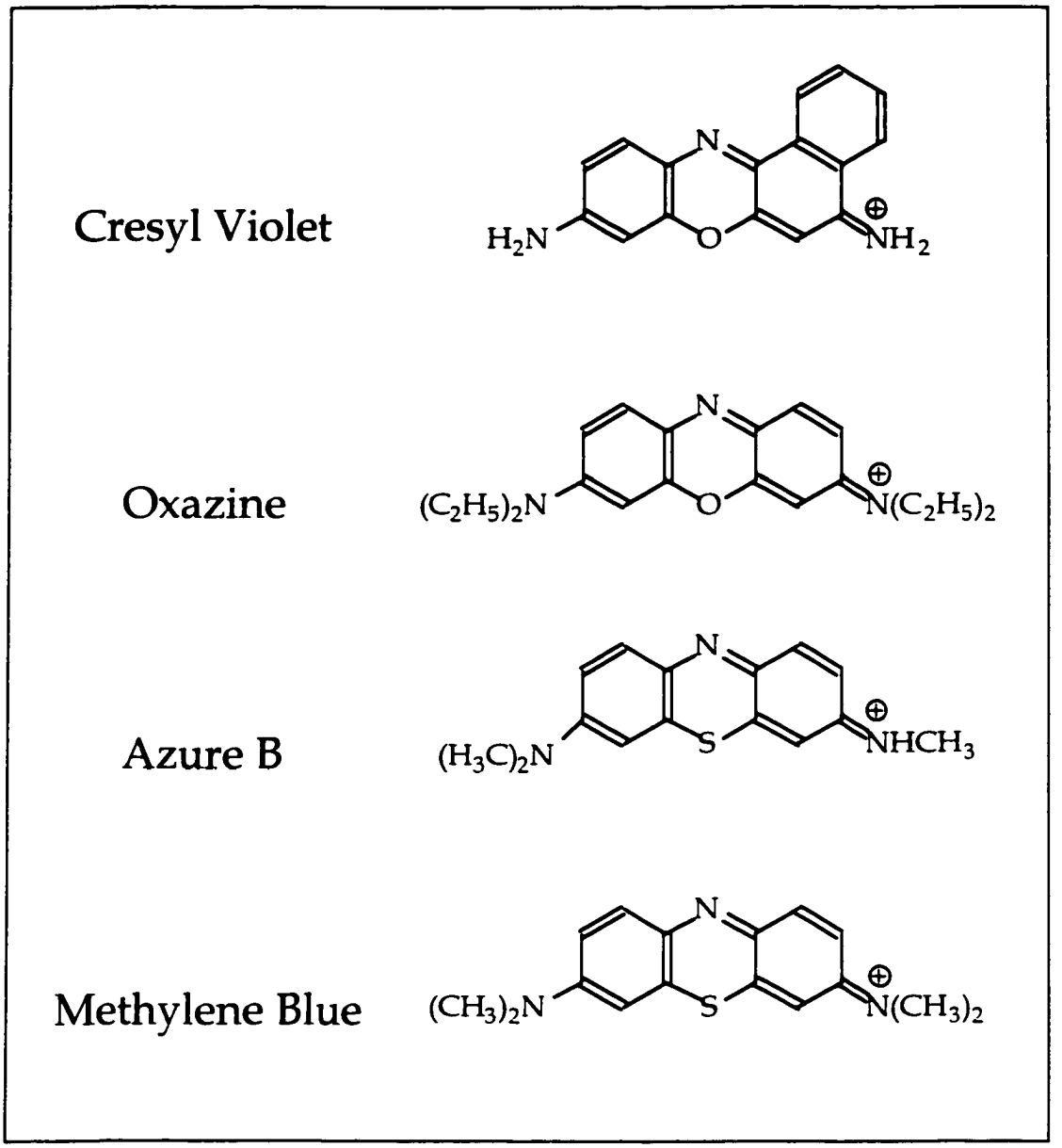

Figure 3.2. Chemical structures of the four organic dyes emphasized in the photoelectrochemical studies discussed in this chapter.

between adsorbed dyes.

Understanding these phenomena may aid in the design of more efficient solar energy conversion systems based on dye sensitization. The idea of selective photoxidation can possibly be applied to information storage, since data can be encoded via the presence or absence of multiple dye photocurrent signals.

The adsorption isotherm of MB^+, the selective photoxidation experiments and the absorption measurements on the SnS_2 crystals reported herein were carried out by Xiumei Dou, a former post doctoral fellow in the Parkinson research group.

EXPERIMENTAL METHODS AND MATERIALS

All of the SnS_2 crystals were grown with the vertical Bridgman method as described in Chapter 2. Both unintentionally doped and doped (Cl^-, Se or As) SnS_2 crystals were grown with this technique. Semiconductor electrodes were prepared as detailed in Chapter 2.

All photoelectrochemical and Mott-Schottky measurements were taken in a three compartment electrochemical cell with a Ag/AgCl reference electrode, a Platinum counter electrode, and a semiconductor working electrode all in a 1 M LiCl/methanol electrolyte solution. Mott-Schottky measurements were carried out as described in Chapter 2. Photoelectrochemical measurements were carried out as reported previously[7] in a similar three electrode cell with an optical quartz window mounted on the working electrode compartment. The electrolyte

solution was 1 M LiCl in methanol with or without hydroquinone (H_2Q) added as regenerator. The dyes, methylene blue, azure B, cresyl violet perchlorate, oxazine 1 perchlorate, diethythiadicarbocyanine, diethythiadcarbocyanine and merocyanine 540 were purchased from the Eastman Kodak Company and used as received. Chlorophyll was provided by Prof. C. C. Schenck at Colorado State University. The area of electrodes was typically 0.3-0.5 cm^2 with a thickness of 1-3 mm, allowing several experiments on fresh surfaces to be carried out by simply cleaving off a thin layer of the crystal with adhesive tape. The light source used for the collection of the photocurrent spectra was a Newport 780 50-W tungsten-halogen lamp. Monochromatic light was obtained by using a Jarrel-Ash Monospec 27 monochromator. The light was focused to a spot of 1x2 mm on the sample. A Lasermax LSX-680-20-D diode laser with an elliptical beam dimension of 3.3x0.8 mm was used to detect MB^+ photocurrent at 689 nm and a Melles Griot 05 LHP 991 HeNe laser with a beam diameter of 1.18 mm was used to detect CV^+ photocurrent at 632.8 nm. Using neutral density filters with the laser provided a large range of light intensities. The light spot was kept smaller than the electrode area so that it could be moved around on the surface to investigate the uniformity of the photocurrent response.

Absorbance measurements of the dyes adsorbed on the van der Waals surface of single crystal SnS_2 were obtained with a Hitachi U-3501 spectrophotometer equipped with a 60 mm diameter integrating sphere. Because SnS_2 absorbs light, a background absorption spectrum of SnS_2 was

subtracted from the absorbance spectra of the dyes adsorbed on the SnS_2 surface. The background spectrum of SnS_2 was obtained by cleaving a thin crystalline layer (a few microns in thickness) of unintentionally doped SnS_2 off of a bulk crystal. Surfaces on both sides of the thin crystal were fresh and smooth. This crystal was then mounted on a 2 mm slit and set in front of the spherical integrator window for transmissive samples, as shown in Figure 3.3. The light beam was focused by a cylindrical lens to a 5 mm x 1 mm line onto the sample. The area of the focused light was smaller than that of the thin crystal to assure that the absorption was only from the dyes adsorbed on the van der Waals surface of the semiconductor. Since the inner wall of the sphere was coated with highly reflecting barium sulfate, the diverged transmitted light was then reflected repeatedly on the walls of the sphere before falling into the aperture formed for the detector on top of the sphere. This divergent transmittance method eliminates the interference effect usually seen in the normal thin layer absorption spectra taken in the usual transmission geometry. After the absorption spectrum of the bare SnS_2 was obtained, the thin crystal was dipped into the diluted dye/methanol solution. It took CV^+ less than a minute to attain an adsorption equilibrium while MB^+ and OX^+ required over a minute. In this experiment, the adsorption time was 5 minutes for each dye. After the thin crystal was taken out and the methanol dried, the sample was again mounted onto the 2 mm slit and its absorption spectrum measured. The absorption spectrum of the dyes on the surface was then obtained by subtracting the

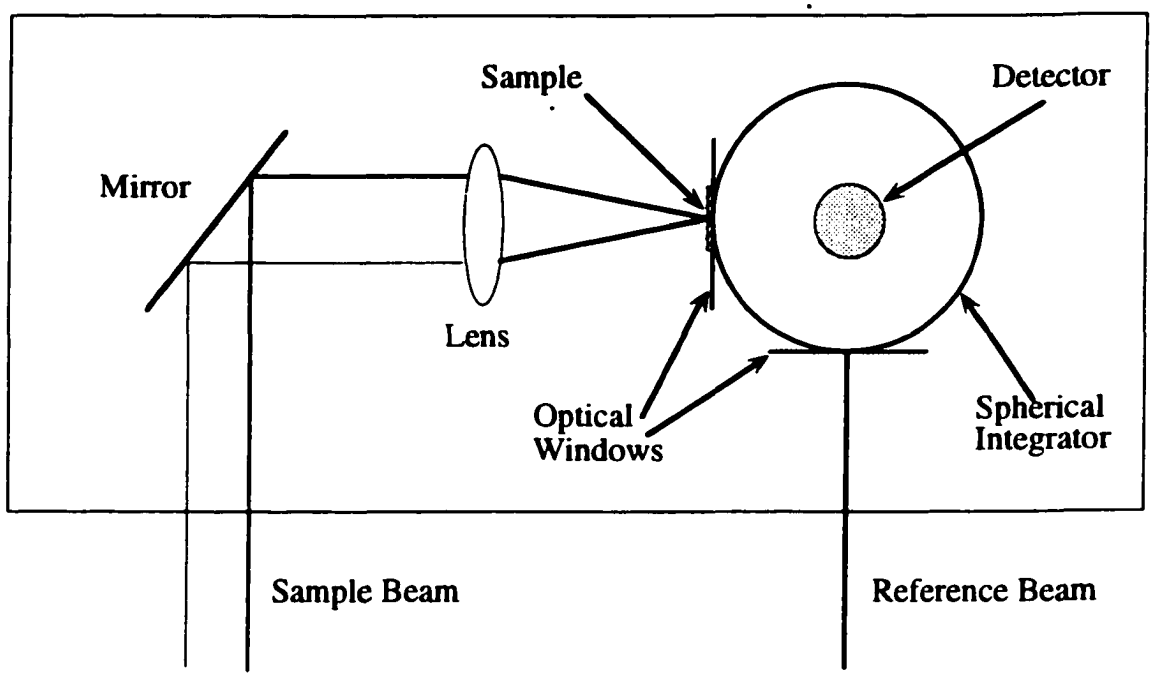

Figure 3.3. Experimental setup for the absorbance measurement of adsorbed dyes on SnS_2 thin films. Light is focused onto the sample by a cylindrical lens and the transmitted light is measured. The spherical integrator is used to eliminate the interference fringes due to the thin sample.

background collected on the bare SnS_2 layer from the total absorption. The Cl-doped SnS_2 was also used for this measurement with no significant difference in the results.

The thiol treatment experiments were carried out with dodecanethiol. After measuring the photoaction spectrum (photocurrent yield vs excitation wavelength) in a dye solution, SnS_2 electrodes from Run 10 were soaked in a 0.1 M dodecanethiol solution in ethanol for 20 minutes. The thiol solution was degassed with nitrogen while the electrodes were immersed in the solution. Then a second photoaction spectrum was obtained.

The SnS_2 samples from Runs 17 and 18 were annealed under a sulfur atmosphere in an attempt to fill any sulfur vacancies. Several crystal pieces from each run were loaded into thick walled quartz ampoules. Approximately 0.08 g of sulfur was placed in each ampoule to achieve the maximum sulfur atmosphere with a pressure 10% below the limitations of the ampoule, as suggested by Chem Glass. The crystals and sulfur were cooled in liquid nitrogen and the ampoule sealed under a pressure of 10^{-5} torr. Ampoules were then placed in vertical Dynatherm furnaces, heated to 500°C at a rate of 50°C/hr, held at this temperature for five days and subsequently cooled down at a rate of 50°C/hr.

RESULTS

Dye Sensitized IPCE on Smooth SnS_2 Surfaces. Figure 3.4a shows the incident photon to current efficiency (IPCE) for photocurrent at 689 nm, the

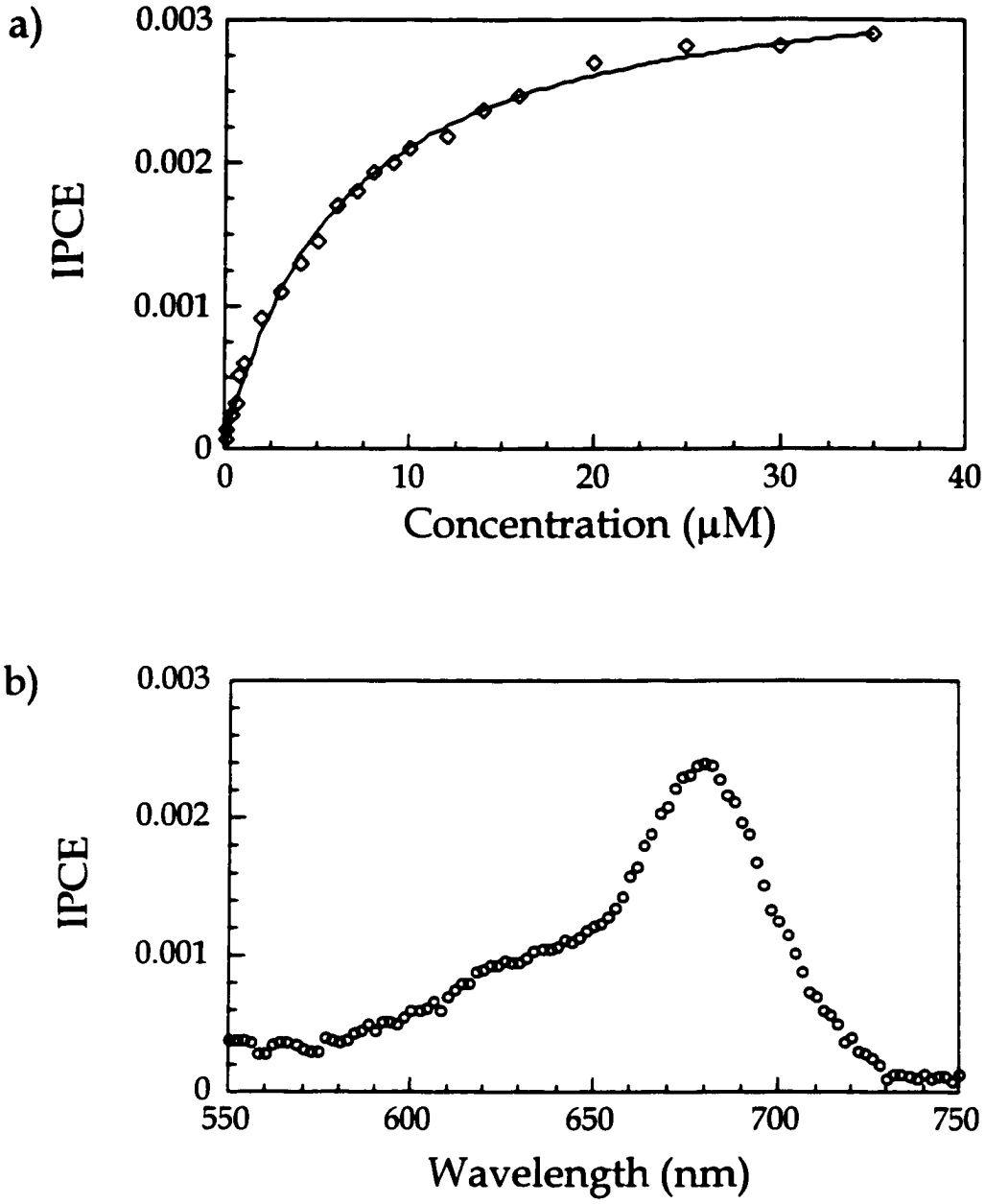

Figure 3.4. Incident photon to current efficiency (IPCE) for MB^+ on a smooth SnS_2 surface biased 0.7 V vs Ag/AgCl reference electrode in a 10 mM hydroquinone in a LiCl/methanol solution. a) IPCE at 689 nm as a function of dye solution concentration. Diamond markers are the actual data points collected and the solid line is the theoretical fit for a Langmuir isotherm. b) The photoaction spectrum with a 10 μM dye solution concentration.

absorption maximum of MB^+, as a function of the dye concentration in solution. The photocurrent was measured by consecutive additions of MB^+/methanol stock solution (1 mM) to the background electrolyte that contained 10 mM hydroquinone (H_2Q) as a regenerating agent. The H_2Q concentration was in one thousand-fold excess compared to the dye concentration to ensure that any changes in the H_2Q concentration would not affect the dye sensitization photocurrent. Each data point was obtained 10 minutes after dye addition. The light intensity for all measurements was 2 μW at 689 nm. The IPCE was derived from the ratio of photocurrent to the photon flux. The photoaction spectra, at all the concentrations measured in this curve, did not show any appreciable shifts indicative of aggregate formation. Figure 3.4b shows the corresponding photocurrent spectrum with a solution dye concentration of 10 μM. Figure 3.4a shows that the IPCE increased linearly with concentration at low dye solution concentration and approached a plateau at about 15 μM. At this concentration, with a freshly cleaved smooth surface, the maximum IPCE at the dye absorption maximum was 3.5×10^{-3} for MB^+.

The photocurrent quantum yield in the above case was both stable with time and remained constant within the light intensity range from 2 μW to 18 mW (77 $\mu W/cm^2$ to 692 mW/cm^2 using a diode laser at 689 nm). This indicates that, within this light intensity, the system is behaving ideally and the photoaction spectra can be accurately measured on the time scale of our experiments. Figure 3.5 shows a typical sensitized photocurrent-voltage curve for MB^+ with a

light intensity of 66.3 μW at 689 nm under the same experimental conditions as above. The current voltage behavior was similar to that of malachite green from a previous report[8] and many other dyes we have studied with SnS_2 as discussed in this chapter.

Photocurrent voltage measurements were used to analyze the electron transfer event at the SnS_2 interface under various solution conditions. A series of photocurrent voltage curves were recorded both with and without dye in an electrolyte/regenerator solution, as well as with irradiation from an argon ion laser (Ar^+, 514 nm or 488 nm), diode laser (689 nm) or helium-neon laser (HeNe, 633 nm). Figure 3.5 shows the photocurrent voltage behavior for three different conditions: 514 nm light with an H_2Q/electrolyte solution, 514 nm light with MB^+ added to the H_2Q solution and 689 nm light with the MB^+/H_2Q solution. The forward and reverse photocurrent voltage curves obtained when the electrode was illuminated with 514 nm light (greater than band gap radiation), have similar $E_{1/2}$ and IPCE values. However, the 514 nm photocurrent signal at 0.2 V was greater when dye was present in solution. Illumination with 689 nm light yielded a half-wave potential shifted approximately 50 mV more negative than the 514 nm curves. In addition, both 514 nm curves had IPCEs almost an order of magnitude greater than the 689 nm curve, as shown in Table 3.1.

Slightly different photocurrent voltage behavior was observed when comparing CV^+ and MB^+ in the same regenerator/electrolyte solution as shown in Figure 3.6. Compared to CV^+, the MB^+ curve had an $E_{1/2}$ approximately

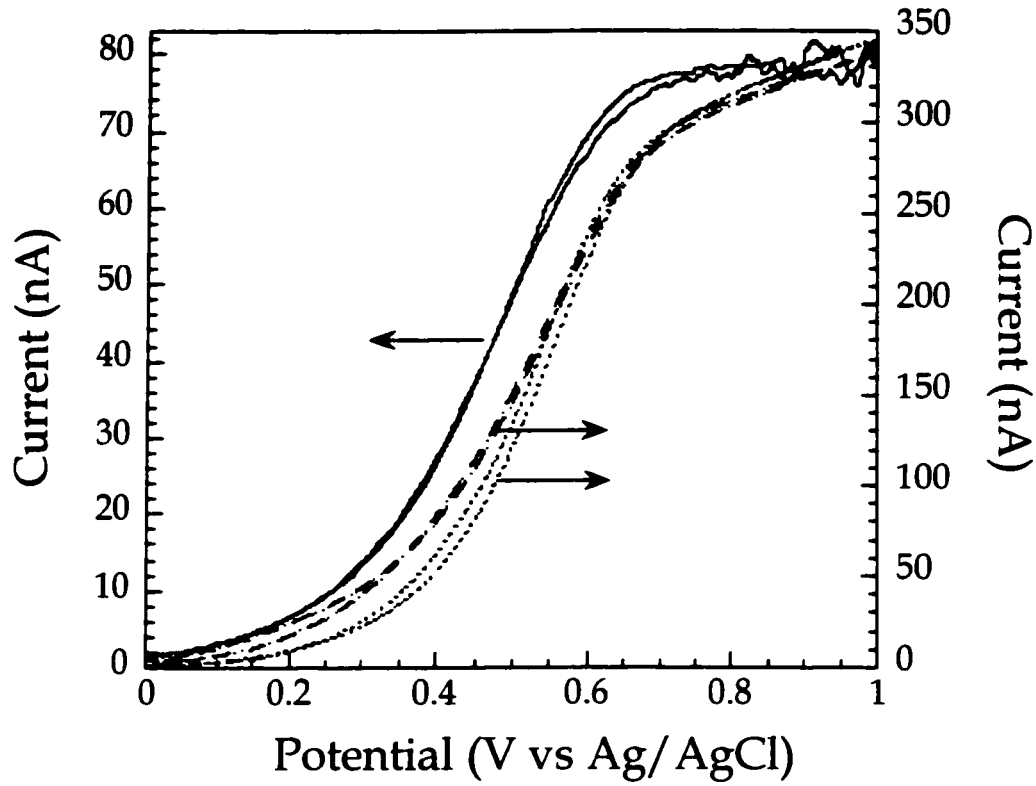

Figure 3.5. Photocurrent voltage curves (forward and reverse) for band gap illuminated and dye sensitized SnS_2 in a 1 M LiCl in methanol solution. The curves, were recorded sequentially with (·····) representing 514 nm light illumination with 30 mM H_2Q added to solution, (— ·) representing 514 nm light illumination with 7 μM MB^+ added to the H_2Q/electrolyte solution and (—) representing 689 nm light illumination with the MB^+/H_2Q/electrolyte solution. The Ar^+ laser power was 30.3 μW and the diode laser power was 66.3 μW. The potential was scanned continuously from 0 V to 1 V and back vs a Ag/AgCl reference electrode at a rate of 5 mV/s.

Table 3.1. Results from photocurrent voltage measurements. Potentials are reported versus a Ag/AgCl reference electrode. Light sources were an Ar^+ laser (488 nm and 514 nm), diode laser (689 nm) and a HeNe laser (633 nm). The IPCEs were taken at the wavelength listed. All measurements were carried out in an electrolyte solution, the electrochemically active species are listed in the Experimental Conditions column. The H_2Q solution was 30 mM and the dye solutions were 7 μM.

Power (μW)	Wavelength (nm)	IPCE (%)	$E_{1/2}$ (V)	Experimental Conditions (solution)
57.5	488 (Ar^+)	8.0	0.50	H_2Q
2250	514 (Ar^+)	2.1	0.53	H_2Q
30.3	514 (Ar^+)	2.6	0.53	H_2Q
3120	689 (Diode)	0.014	0.38	H_2Q
30.3	514 (Ar^+)	2.5	0.52	$H_2Q + MB^+$
66.3	689 (Diode)	0.23	0.45	$H_2Q + MB^+$
3120	689 (Diode)	0.31	0.38	$H_2Q + MB^+$
71.9	633 (HeNe)	0.044	0.38	$H_2Q + CV^+$

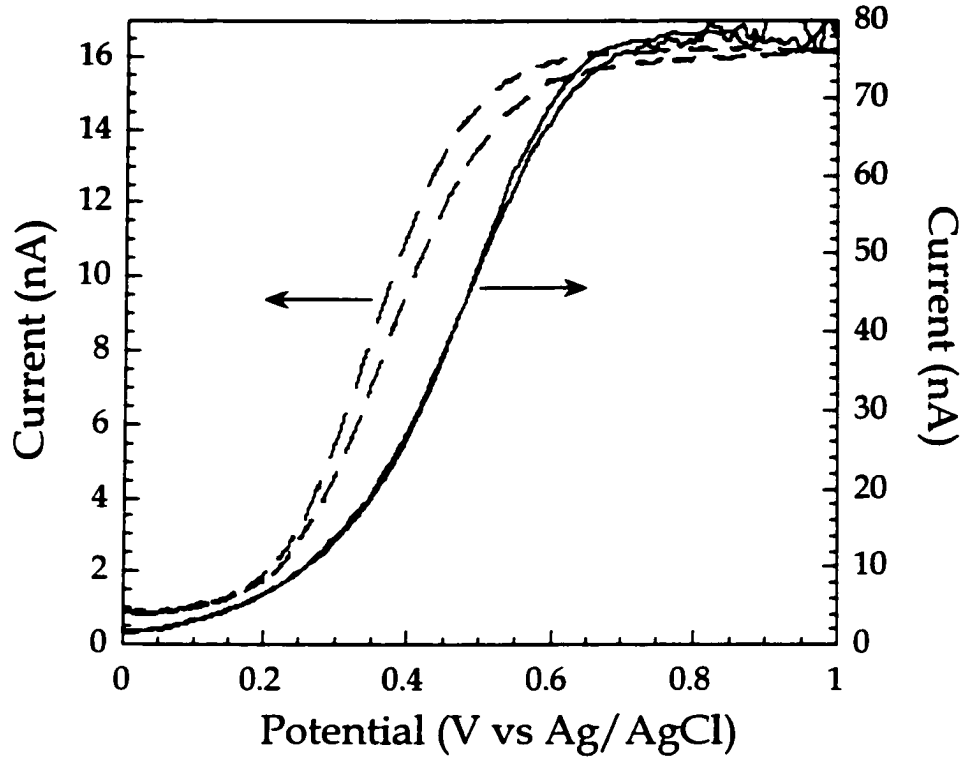

Figure 3.6. Dye sensitized photocurrent voltage curves (forward and reverse) for SnS_2 in a 7 μM dye/30 mM H_2Q/1 M LiCl in methanol solution. Dye sensitized response for CV^+ (— —) and MB^+ (—). The diode laser power was 66.3 μW and the HeNe laser power was 71.9 μW. The potential was scanned continuously from 0 V to 1 V and back vs Ag/AgCl at a rate of 5 mV/s.

70 mV more positive, an IPCE five times larger and a slower increase in the photocurrent with increasing positive voltage. The lower IPCE for CV^+, indicates that the overall MB^+ sensitization process was more efficient. This was surprising in view of the more negative $E_{1/2}$ of CV^+, which would suggest that its electron injection process should have a larger driving force. Hence, the driving force for electron injection does not appear to play a significant role in the IPCE for the dyes studied as long as the excited state potential is more negative than the SnS_2 conduction band edge.

The photocurrent voltage and current voltage data, listed in Table 3.1, shows the relationship between IPCE and $E_{1/2}$ for H_2Q, MB^+ and CV^+. This data reveals there was an order of magnitude difference in IPCE for 689 nm light illumination of SnS_2 before and after MB^+ was in solution. This validates the assumption that the photocurrent signal was produced by MB^+ as opposed to the regenerator H_2Q. The varying $E_{1/2}$ values indicate that different potentials were required for electron escape and subsequent photocurrent generation. The power of the light source did not appear to have a significant effect on the IPCE except that higher powers caused a slight decrease in the IPCE.

The maximum IPCE of CV^+ on smooth SnS_2 surfaces was a factor of five lower than that for MB^+ in the photocurrent voltage measurements (see Table 3.1). Low quantum yields for sensitization were also observed for several cyanine dyes including merocyanine 540 (MER 540), diethylthiadicarbocyanine (DTDC) and diethylthiatricarbocyanine (DTTC). All of these dyes had been

shown to sensitize SnS_2 in earlier work[7]. The earlier work, however, used vapor transported crystals while the studies herein used Bridgman melt growth crystals, both of which were discussed in Chapter 2. The vapor transport crystals could have different surface and or bulk properties than the Bridgman grown crystals and that could affect the dye sensitized IPCE.

The photocurrent at the CV^+ absorption maximum increased dramatically when the light spot was moved to areas near obvious defects such as edge defects on the SnS_2 surface that are recognizable with the human eye. While a much higher dye sensitized photocurrent (620 nm) was observed near these defect sites, the photocurrent signal for the SnS_2 band gap transition at 460 nm decreased slightly at these same sites, as shown in Figure 3.7a. Figure 3.7b shows the photocurrent spectrum after the electrode was soaked for 30 minutes in a solution containing 5 μM of both MB^+ and CV^+, washed with methanol, left overnight, and put back into 10 mM H_2Q electrolyte solution without dye present. The photocurrent spectrum indicates that the two dyes apparently both remain on the electrode surface. Figure 3.7b also shows that cleaving off a thin SnS_2 layer from the electrode removed the MB^+, however, the photocurrent spectrum still shows the presence of CV^+ as illustrated by the difference spectrum in Figure 3.7b.

Shifts in the SnS_2 Flat Band Potential. The flat band potential is a unique potential for which the potential drop between the surface and the bulk of the semiconductor electrode is zero (there is no electric field in the semiconductor).

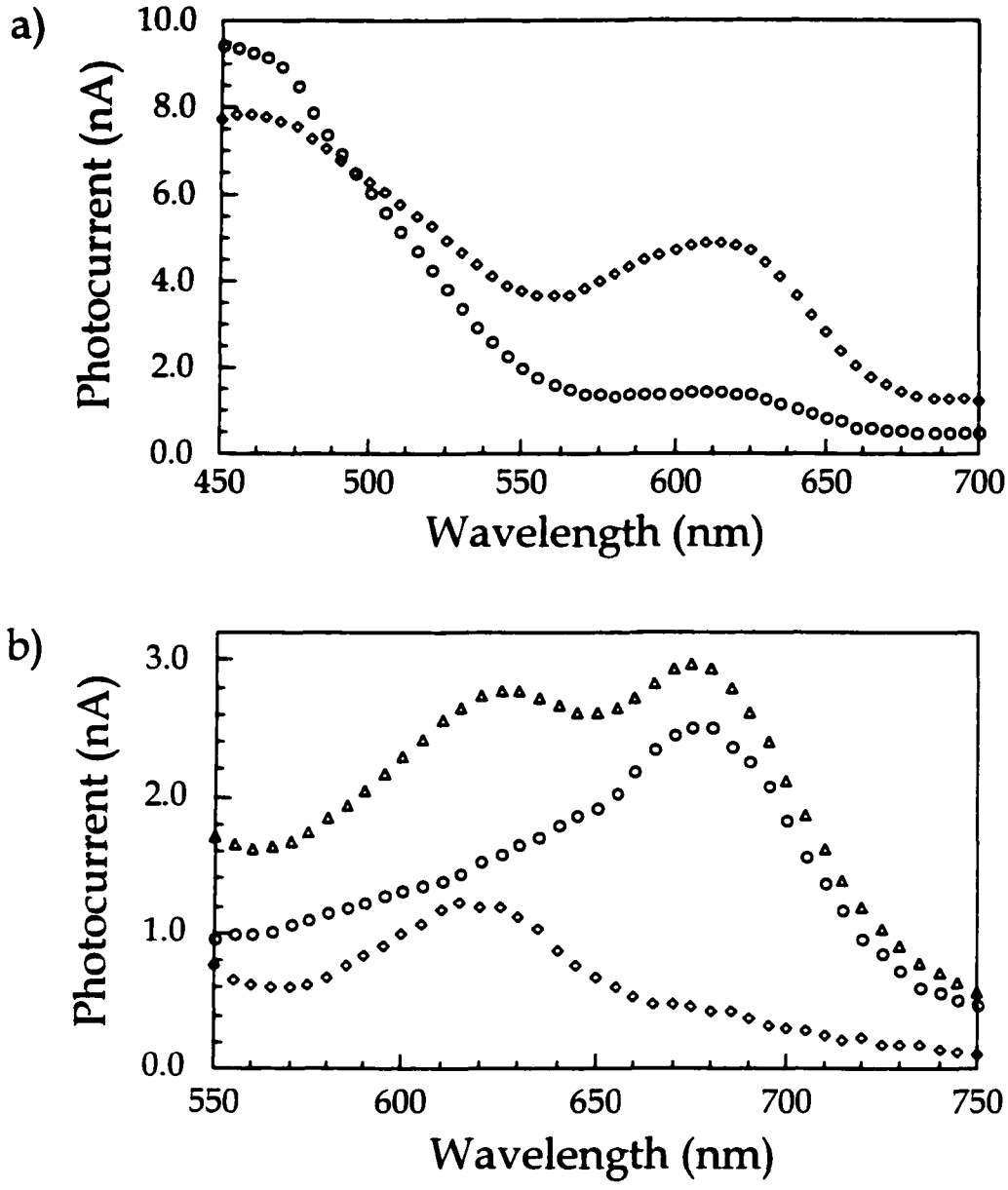

Figure 3.7. Effect of edge site defects on the dye sensitized photocurrent. The SnS_2 electrode was held at 0.7 V vs Ag/AgCl in a 10 mM H_2Q/methanol solution. a) Dye sensitized photoaction spectra of 5 μM CV^+ at exposed edge sites (diamonds) and in a smooth part (circles) of the SnS_2 electrode. b) Photoaction spectra of an electrode soaked in a solution of MB^+ and CV^+ (5 μM each), subsequently washed in methanol, reinserted into a fresh electrolyte solution (triangles) and then cleaved (diamonds). The difference spectrum of before and after cleaving (circles).

Measuring the flat band potential via impedance measurements provides information on the energetics of the semiconductor/electrolyte system. The effect that both H_2Q and MB^+ have on the flat band potential of SnS_2 in 1 M LiCl solutions was investigated. Impedance measurements taken in succession after the addition of electrolyte, H_2Q and then MB^+, demonstrated that a positive flat band (E_{FB}) shift occurred after each addition. Results are shown in Figure 3.8. The original E_{FB} was -0.168 V. Upon adding H_2Q, there was a shift to +0.259 V and a second shift to +0.392 V with the addition of MB^+. This corresponded to a positive shift of 0.43 V from the addition of H_2Q and then a further shift of 0.13 V, after the addition of MB. This positive shift demonstrates that there was a definite dye-semiconductor interaction. This interaction may affect the rate of geminate recombination if it becomes energetically more favorable for the injected electron to recombine with the dye ground state.

A check on these results was accomplished by determining the carrier concentration of the SnS_2 samples and comparing the results with those obtained in Chapter 2. This was possible because along with E_{FB} determination, Mott-Schottky plots allow the carrier concentration to be calculated. The carrier concentration for the SnS_2 samples (Run 10) used in this study was determined to be approximately 6.4×10^{16} cm^{-3} from Mott-Schottky plots, which agreed with the results presented in Chapter 2.

Absorbance of Dyes Adsorbed on Smooth SnS_2 Surfaces. To determine the actual amount of adsorbed dye on the SnS_2 surface, the absorption spectra of

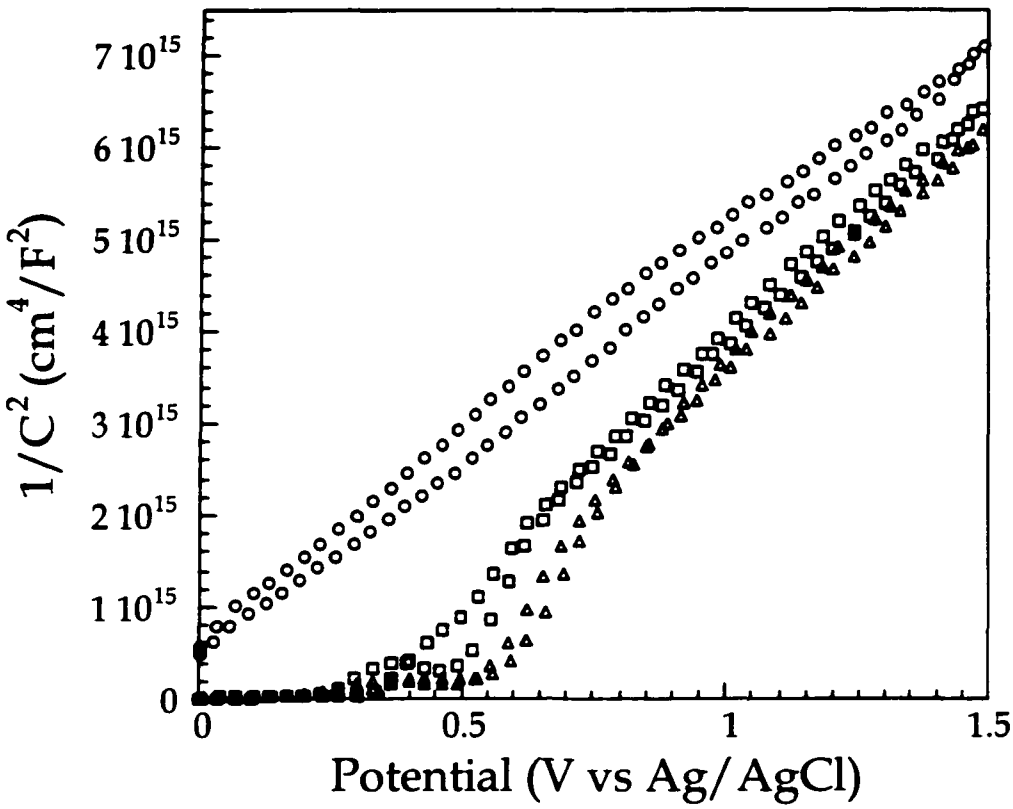

Figure 3.8. Mott-Schottky plots of SnS_2 vs Ag/AgCl at 20 kHz. Initially, the semiconductor electrode was in a 1 M LiCl/methanol solution (circles), then 30 mM H_2Q was added (squares) followed by the addition of 7 μM MB (triangles).

dyes adsorbed on thinly cleaved SnS_2 crystals were measured. Spectra were obtained after immersing a thin, freshly cleaved SnS_2 crystal into a 10 μM dye solution in methanol. This dye concentration was near the plateau of the adsorption isotherm and was the same concentration routinely used in the photoelectrochemical measurements. The divergent transmittance method, coupled with a spherical integrator, was used to eliminate the interference fringes caused by the thin SnS_2 samples, as mentioned in the experimental section. It can be seen, from Figure 3.9, that little or no absorption was detected for cresyl violet, which should show an absorption peak near 625 to 635 nm, while methylene blue as well as oxazine had an absorbance of about 0.016 absorbance units above the baseline as a result of dye adsorbed on both front and back faces of the crystal. Using Beer's law the absorption of dye molecules on one surface was estimated to be about 0.008 absorbance units for both MB^+ and OX^+ corresponding to close to monolayer coverage. Note that the absorption maximum of MB^+ on the surface in this experiment was about 667 nm, while its dye sensitized photocurrent maximum on the electrode was about 677.

Selective Photoxidation of MB^+. A selective photoxidation or "hole burning" experiment was carried out to see if dyes could be selectively removed from the surface. The dyes were adsorbed onto an electrode with exposed edge sites so CV^+ would show a dye sensitized photocurrent, either separately or simultaneously with MB^+. The electrode was then illuminated with laser light at wavelengths corresponding to their respective absorption maxima. When

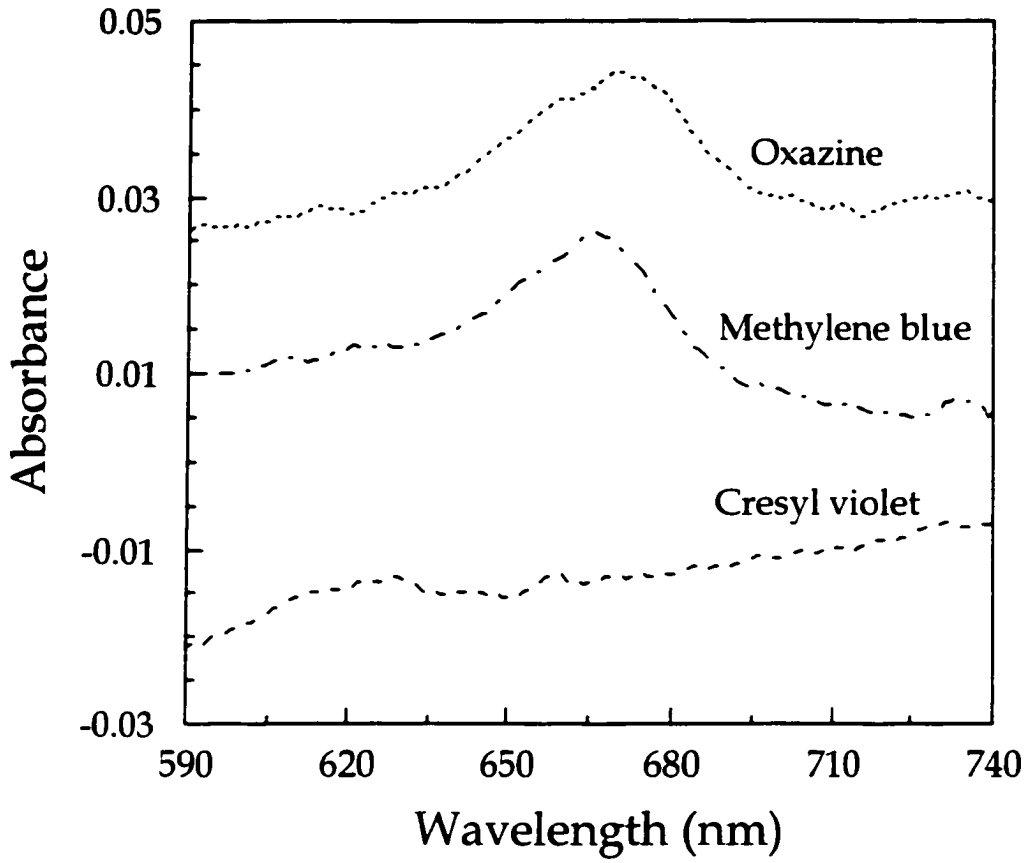

Figure 3.9. UV-Vis absorption spectra of OX^+, MB^+, and CV^+ adsorbed on smooth SnS_2 surfaces. A freshly cleaved unintentionally doped SnS_2 film was immersed in the 10 μM dye/methanol solution for 5 minutes removed and dried before taking a spectrum. The diffuse reflectance method was used to eliminate the interference fringes caused by the thin film absorption (see Figure 3.3).

regenerating agent (10 mM H_2Q) was present in the solution, neither CV^+ nor MB^+ could be depleted from the surface through photoxidation with either a HeNe laser or a diode laser with 2 mW of intensity. Selective photoxidation was achieved only when H_2Q was not present in the electrolyte solution.

The selective photoxidation of MB^+ over CV^+ was accomplished when the electrode was irradiated with either 689 nm or 633 nm light. Figure 3.10 displays the results when a dye sensitized SnS_2 electrode was illuminated by a 689 nm diode laser (2.5 mW), which is near the MB^+ absorption maximum, with 5 μM of each MB^+ and CV^+ in the electrolyte solution but containing no H_2Q. The initial photoaction spectrum was taken with only a few microwatts of illumination from a tungsten halogen lamp before the intense illumination and corresponds to a mixture of CV^+ and MB^+ sensitization. The spectrum after laser excitation showed only sensitization from CV^+, indicating the preferential removal of MB^+ from the surface (difference spectrum). Excitation near the absorption maximum of CV^+ with a HeNe laser (1 mW or greater at 632.8 nm) also resulted in the depletion of MB^+ molecules from the surface rather than CV^+. The photocurrent signal for MB^+ recovered gradually in about 45 minutes if there was MB^+ in the solution. During the course of recovery the CV^+ sensitization signal also increased. When the same experiment was done without MB^+ in the solution, its photocurrent signal was permanently removed and a substantial increase in the CV^+ signal was observed. These results indicate that the adsorption/desorption kinetics of CV^+ were faster than for MB^+.

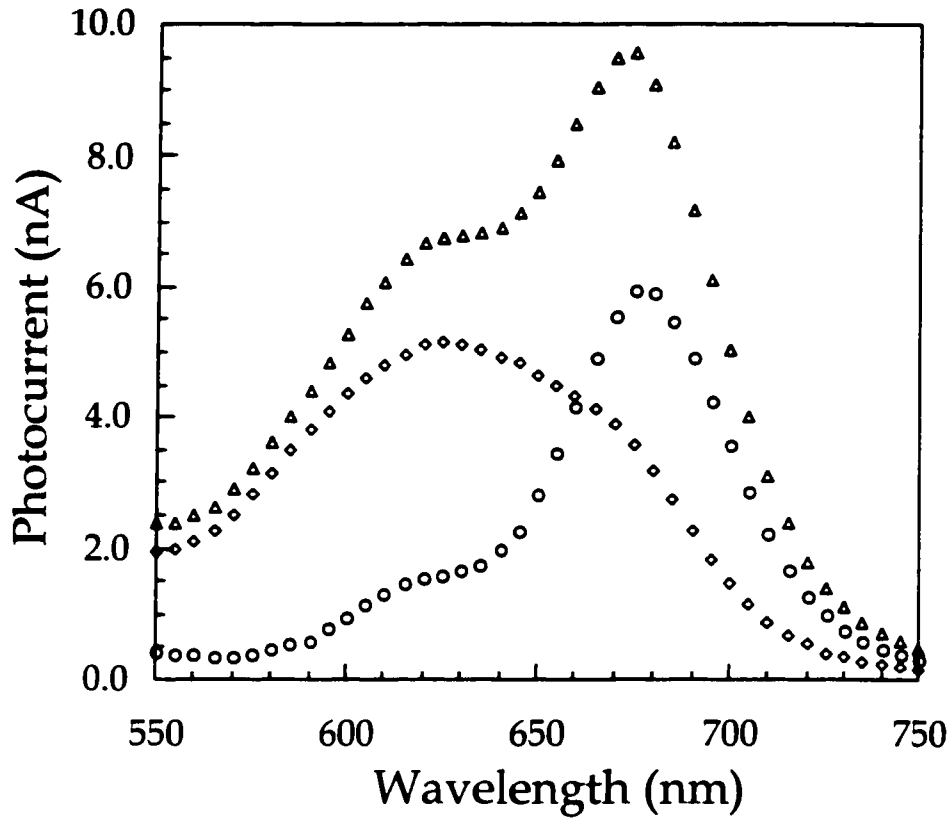

Figure 3.10. Selective photoxidation ("hole burning") of MB^+ from the SnS_2 surface by short time illumination with 2 mW of 689 nm light from a diode laser when regenerator was absent from solution. Triangles represent the photoaction spectrum before "burning", diamonds are after "hole burning", and circles are the difference (before - after). The SnS_2 electrode was in a electrolyte solution containing both 5 μM CV^+ and MB^+. The electrode was biased at 0.7 V vs Ag/AgCl reference electrode.

Effect of Doping Level on Sensitized Photocurrents. The effect of carrier concentration on IPCE was investigated with SnS_2 crystals with varying carrier concentrations, ranging from $4x10^{15}$ cm^{-3} to $1.09x10^{18}$ cm^{-3}. Table 3.2 shows the carrier concentrations and resulting IPCE for four dyes, MB^+, AZB^+, OX^+ and CV^+. No direct correlation was observed between the carrier concentrations and the dye sensitized IPCEs. This indicates that both the effects of the electric field gradient and the concentration of surface chloride do not affect the dye sensitization efficiency.

The results in Table 3.2 also show that there are distinct differences in IPCEs between the four dyes. The IPCE for MB^+ is roughly a factor of two greater than AZB^+ and a factor of five greater than both CV^+ and OX^+. Two of these dyes, MB^+ and AZB^+, have the same $^*E_{ox}$ (Table 3.3) and higher quantum yields than either CV^+ or OX^+ for formation of the triplet excited state[9,10,16], which may explain the higher IPCEs for MB^+ and AZB^+ compared to OX^+ and CV^+. The IPCE variation between all four dyes may be due to different recombination pathways and differences in adsorption behavior as will be discussed later.

Surface Modification via Thiol Addition. In an attempt to determine whether there were sulfur vacancies on the SnS_2 surface that could potentially affect both dye absorption and sensitization, SnS_2 electrodes were soaked in degassed 0.1 M dodecanethiol solutions in ethanol and changes in the photoaction spectra were monitored. If dodecanethiol adsorbs to the SnS_2

Table 3.2. The SnS_2 carrier concentrations and corresponding IPCEs for MB^+, AZB^+, OX^+ and CV^+. Dye sensitized IPCEs were measured in 7 μM dye/10 mM H_2Q/1 M LiCl/methanol solutions with the SnS_2 electrode biased at 0.7 V vs Ag/AgCl.

Run #	Carrier Conc. (cm^{-3} dopant)	IPCE (%) MB^+	IPCE (%) AZB^+	IPCE (%) OX^+	IPCE (%) CV^+
13	$1.09x10^{18}$ Cl	0.24±0.06	0.18±0.05	0.072±0.03	0.059±0.04
4	$8.0x10^{17}$ Cl	1.3±0.1	0.75±0.09	0.18±0.02	0.12±0.01
18	$4.2x10^{17}$ Cl	0.23±0.09	0.15±0.07	0.043±0.003	0.071±0.02
12	$3.7x10^{17}$ Cl	0.18±0.04	0.11±0.02	0.024±0.003	0.040±0.004
17	$2.3x10^{17}$ Cl	0.15±0.02	0.075±0.02	0.034±0.002	0.024±0.01
8	$7.8x10^{16}$ Cl	0.28±0.07	0.21±0.07	0.055±0.0023	0.051±0.01
10	$7.3x10^{16}$ Cl	0.18±0.01	0.090±0.01	0.030±0.0008	0.044±0.007
14	$5.7x10^{16}$ Se	0.47±0.05	0.29±0.01	0.085±0.003	0.074±0.002
9	$3.2x10^{16}$ Cl	0.24±0.003	0.13±0.009	0.035±0.004	0.048±0.007
15	$4x10^{15}$ As	0.27±0.08	0.13±0.05	0.044±0.01	0.053±0.001

Table 3.3. The λ_{max} in methanol for CV^+, OX^+, AZB^+ and MB^+ are listed along with the first oxidation and reduction potential in volts vs Ag/AgCl.[7] The IPCE is the average for the data in Table 3.2.

Dye	λ_{max} (nm)	$^{\circ}E_{ox}$ (V)	$^{\circ}E_{red}$ (V)	IPCE (%)
CV^+	601	1.35	-0.34	0.058±0.011
OX^+	645	1.25	-0.348	0.060±0.008
AZB^+	615	1.15	-0.2	0.21±0.04
MB^+	658	1.15	-0.295	0.35±0.05

surface filling sulfur vacancies, than the dye sensitized IPCE would be eliminated. However, both CV^+ and MB^+ exhibited only relative decreases of 10% in their IPCEs after thiol treatments. Photoaction spectra for MB^+ taken both prior to and after thiol treatment are shown in Figure 3.11. The minute decrease in the dye sensitized IPCE after thiol addition shows that dodecanethiol has little effect on the sensitization process. In addition, these results indicate that sulfur vacancies on the surface are not responsible for dye sensitization. There is also a possibility that dodecanethiol does not bind to the sites that effect sensitization. The influence of sulfur on the dye sensitization efficiency was further studied in the following section on annealing.

Sulfur Composition on Smooth SnS_2 Surfaces. In addition to the attempts to fill sulfur vacancies with dodecanethiol, SnS_2 samples were annealed in a sulfur atmosphere in an attempt to reduce the number of sulfur vacancies and determine whether sulfur vacancies affected the dye sensitized IPCE for MB^+, AZB^+, OX^+ and CV^+ on SnS_2 electrodes. Several SnS_2 samples were taken from two different growth runs with carrier concentrations of $2.3x10^{17}$ cm^{-3} Cl^- and 4.2x1017 cm^{-3} Cl^-. Half of these samples were annealed in an atmosphere of sulfur. After annealing, the dye sensitized IPCEs were measured for both the annealed and the unannealed samples. The results are graphed in Figure 3.12.

Figure 3.12 shows a bar graph comparing the IPCEs of MB^+, AZB^+, OX^+ and CV^+ on both annealed and unannealed SnS_2 with chloride carrier concentrations of $2.3x10^{17}$ cm^{-3} and $4.2x10^{17}$ cm^{-3}. An increase in the dye

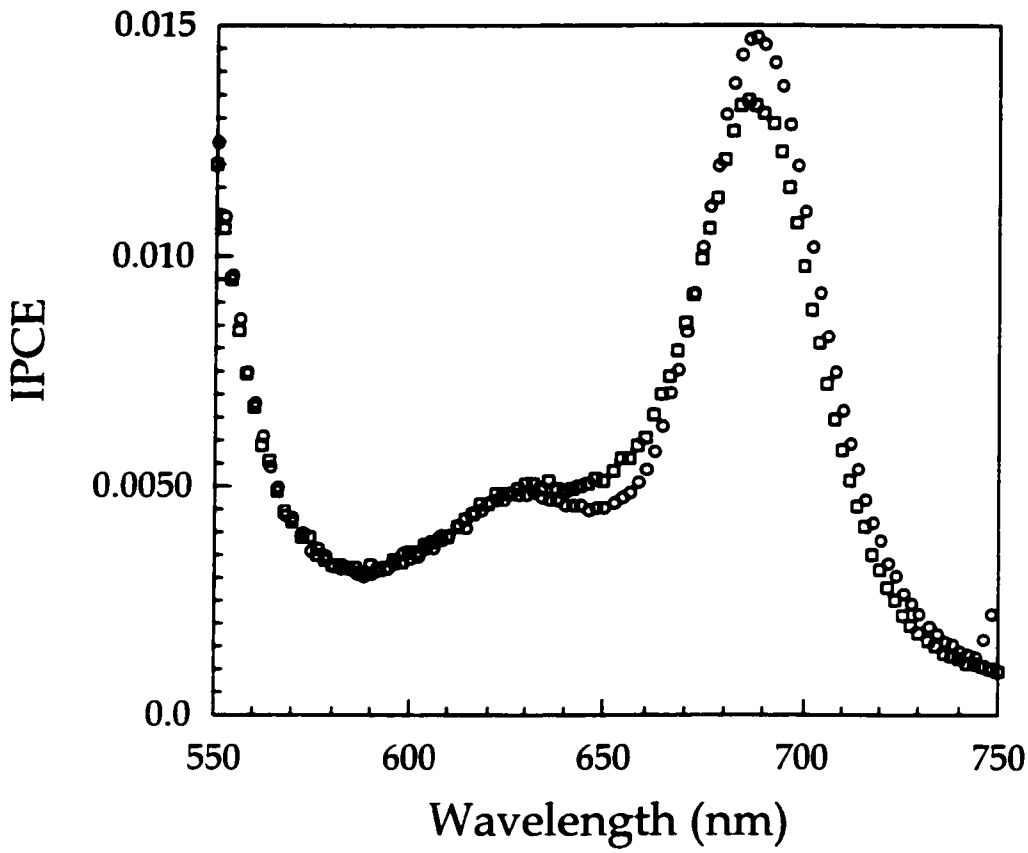

Figure 3.11. Dye sensitized photoaction spectra were measured vs Ag/AgCl in a 7 μM MB^+ and regenerator/electrolyte solution. A SnS_2 electrode was immersed in the dye solution and a photoaction spectrum taken (circles). Then the electrode was soaked in a degassed 0.1 M dodecanethiol solution in ethanol for 20 minutes, returned to the dye solution and a second photoaction spectrum acquired (squares).

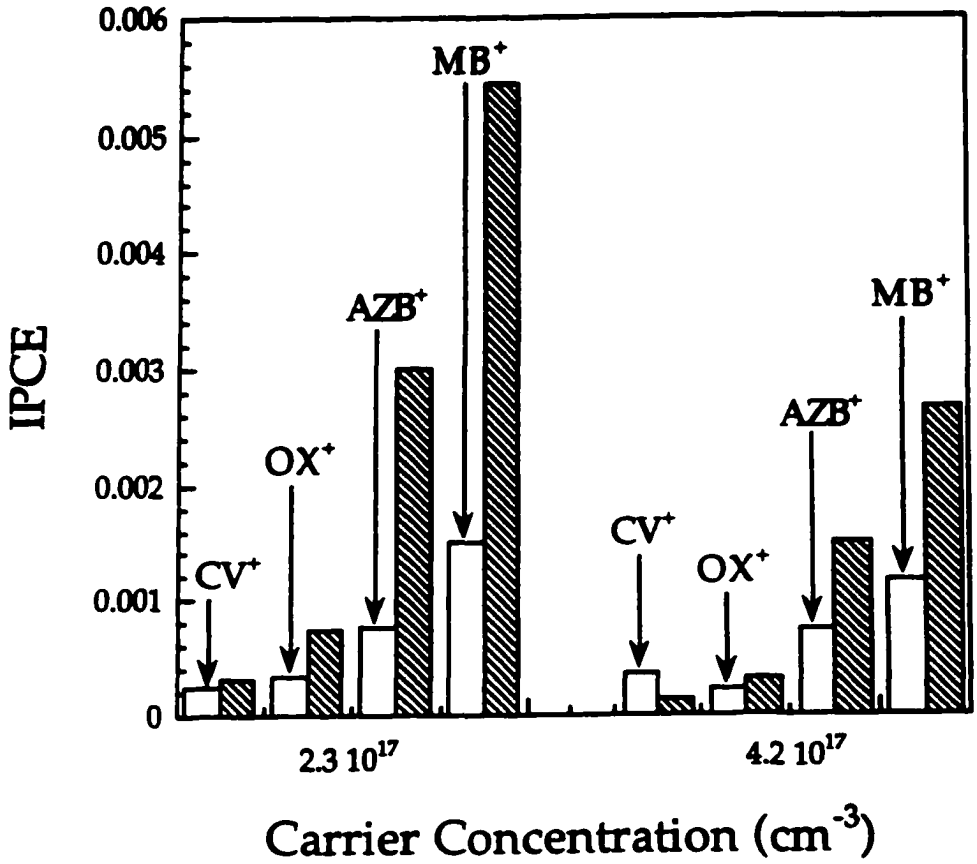

Figure 3.12. Several SnS_2 samples from two separate runs with different carrier concentrations were annealed under a sulfur atmosphere. Photoaction spectra of annealed SnS_2 (cross hatched columns) were measured and compared to SnS_2 (white columns) from the same runs that were not annealed. Photocurrent was then converted to IPCE. All photoaction spectra were biased 0.7 V vs Ag/AgCl in a 7 μM dye in a 30 mM H_2Q electrolyte solution. The IPCE is indicated for each dye on SnS_2 electrodes, that were not annealed. While the IPCE corresponding to the same dye but on annealed SnS_2 is depicted in the column directly to the right.

sensitized IPCE for MB^+, AZB^+ and OX^+ was observed for the annealed SnS_2. While CV^+ exhibited either a slight increase for the annealed $2.3x10^{17}$ cm^{-3} SnS_2 samples or a decrease for the annealed $4.2x10^{17}$ cm^{-3} samples. After annealing the $2.3x10^{17}$ cm^{-3} samples, AZB^+ showed a four-fold increase in dye sensitized IPCE, MB^+ showed a three-and-a-half fold increase and OX^+ showed a two fold increase for the same samples. Smaller increases in the dye sensitized IPCEs were observed for the $4.2x10^{17}$ cm^{-3} samples. Both MB^+ and AZB^+ yielded proportionally larger increases in dye sensitized IPCE for the higher carrier concentration samples than OX^+ and CV^+, the later of which showed a decrease in dye sensitized IPCE. These results indicate that sulfur vacancies have a strong influence on the dye sensitized IPCE. Further annealing experiments must be carried out to determine the importance of Cl^- concentration.

DISCUSSION

Low Dye Sensitized IPCE on Smooth Surfaces. It is known that the extinction coefficients for MB^+ and CV^+ in solution at their absorption maxima are about the same ($8x10^4$ L/mole-cm at ~ 615 nm for CV^+ and at ~ 650 nm for MB^+ in methanol). Therefore the non-detectable absorption from CV^+ on the thin crystal, shown in Figure 3.9, implies that there are no CV^+ molecules on the cleaved dry surface. The measured absorbance of the adsorbed MB^+ at its absorption maximum in Figure 3.9 may be considered an upper bound of the monolayer absorption because additional dye molecules may deposit on the SnS_2

surface after removing the thin crystal from the solution. This is due to small droplets of solution that remain on the crystal resulting in additional dye molecules on the surface. Combining the absorbance (0.008) with the quantum yield of MB^+ sensitized photocurrent at this wavelength results in a QYAP higher than 44%, in agreement with the previous conclusion of high QYAP in these layered semiconductors.[6,8] The lower IPCE for CV^+ on the smooth basal plane of SnS_2 could be explained by much smaller adsorption of the dye compared to MB^+ instead of any significant differences in their QYAPs. However, we explain the lack of CV^+ on the surface in the dry absorption experiment on the faster desorption of CV^+ compared to MB^+ as was determined in the "hole burning" experiments that will be discussed further in the section titled "Selective Photoxidation". Therefore the dry surface may not represent the state of adsorption in the electrolyte solution, conditions under which the sensitization experiments are done. A definitive experiment, that we have not done yet, would be to measure the surface concentration of the dye molecules during the sensitization experiments similar to experiments performed by Spitler[17] where dyes adsorption on ZnO was monitored using total internal reflection spectroscopy.

As mentioned earlier in this chapter, there is an ~10 nm shift between the absorption spectrum for MB^+ and its photocurrent spectrum. Because the absorption spectra are taken under dry conditions, the 10 nm blue shift in the absorption spectrum of MB^+ may reflect the absence of the electrolyte solution at

the interface that should influence the electronic states of a charged dye molecule such as MB^+. A similar shift is observed between the dye absorption maximum in solution and the maximum of the sensitization photocurrent that has previously been ascribed to solvation effects since about half of the solvation sheath is absent in an adsorbed dye.[18]

Dye Intercalation. The relatively large size of the SnS_2 semiconductor electrodes makes it possible to probe different areas of the crystal and correlate the photoresponse with the surface morphology. Figure 3.7a and b show that dye molecules can penetrate into the electrode near exposed edges of the SnS_2 crystal. This agrees with the previous observation for MB^+ on SnS_2 electrodes where very high quantum yields per incident photon (14%) were explained by the intercalation of dye molecules into exfoliated layers[7] putting multiple dye layers in the absorption path of the exciting light. In Figure 3.7a, the CV^+ photocurrent increases three fold when the incident light is moved from the center where the electrode is smooth to the edge of the SnS_2 electrode where step sites are present. Figure 3.7b demonstrates that CV^+ intercalated into the SnS_2 layers because a dye sensitized photoresponse was recorded after cleaving off surface layers of the SnS_2. Because a photoresponse was not observed for MB^+ after cleaving, this indicates that CV^+ penetration into multiple SnS_2 layers was more favorable.

Another factor that may account for the higher dye sensitized photocurrent near a step edge may be that the multiple SnS_2 layers exposed at

the edge site could result in an increased surface area and a correspondingly higher dye surface coverage. In addition, the step edges on the semiconductor electrode may provide either a much stronger binding site for the dyes, or sites for nucleation of two dimensional dye islands. This is especially true for CV^+ whose dye sensitized photocurrent is 3-7 times smaller than that for MB^+, on the smooth surface.

The ability of CV^+ to intercalate into the SnS_2 layers to a greater degree than MB^+ (Figure 3.7b) could be due to several phenomena. First, CV^+ may have a different binding site than MB^+ thus step edges could provide more sites for CV^+ adsorption. This contradicts the increase in sensitization observed in the experiment where MB^+ is "hole burned" from the surface. Second, the intercalation could reflect a kinetic factor, i.e., CV^+ adsorbs to the step edge sites faster than MB^+ and its replacement by MB^+ takes place on a longer time scale than the experiment (a few hours).

At this point, we have not determined if the intercalation is physically or chemically driven. We define physical intercalation as dyes entering layers that have already been separated as a result of damage to the surface from cleaving or strain in the as-grown crystal. Chemically driven intercalation results from a spontaneous expansion of the layers due to the chemical potential of the system being lowered by the intercalation process. We favor the physical intercalation of the electrode because X-ray analysis indicates no lattice expansion of SnS_2 powders exposed to methanolic solutions of concentrated dye molecules for

extended periods (up to 1 year).[19]

Adsorption Isotherm for MB^+. The shapes of the isotherm shown in Figure 3.4a resemble an adsorption isotherm for physisorption of a monolayer. If we assume that the photocurrent signal is linearly proportional to the amount of adsorbed dye, Figure 3.4a can be viewed as an adsorption isotherm for MB^+ on the surface. Work by Spitler[20] helped to validate this assumption as his adsorption isotherm results, using attenuated total reflection, showed that the QYAP was a constant function of surface coverage for rhodamine and rose bengal adsorbed on ZnO.

A relation describing Langmuir type adsorption for dye adsorption on crystal surfaces may be written as the following:[21,22]

$$C/C_s = C/C_m + 1/C_mK, \qquad (3.1)$$

where C is the dye solution concentration (μM), C_s is the dye surface concentration (molecules/cm^2), C_m is the dye surface concentration at monolayer coverage (molecules/cm^2), and K is the adsorption coefficient (μM^{-1}). If we assume that one electron is collected for each photon absorbed, i.e., QYAP =1, then:

$$C_s = IPCE/s \qquad (3.2)$$

where s is the molecular absorption cross section (cm^2/molecule). For MB^+ and CV^+, the molecular absorption cross section is about $1.2x10^{-16}$ cm^2/molecule for each molecule at their respective absorption maxima. Then, Equation 3.1 can be rewritten

$$IPCE = C_m KsC/(KC + 1). \quad (3.3)$$

The fit of the adsorption isotherm data with Equation 3.3 is plotted as a solid line in Figure 3.4a. The Langmuir type isotherm assumes that the heat of adsorption, $-\Delta H$, for dye molecules on the substrate surface is independent of the surface coverage, and that the dye molecules adsorb onto all the surface sites non-preferentially and independently. From Figure 3.4a, it can be seen that the Langmuir isotherm fits the data well. Therefore, MB^+ should exhibit Langmuir type adsorption behavior.

The information derived from this analysis is summarized in Table 3.4. The heat of adsorption ($-\Delta H$) is estimated for the expression adapted from Spitler and Günther[22-24] as follows:

$$\Delta H = 2.3\ RT \log(D/C_m K), \quad (3.4)$$

where D is the estimated thickness of the dye layer on the surface. The ΔH value in Table 3.4 is calculated using a thickness for the dye layer of 5 Å. The value of 7 kcal/mole obtained indicates a weak van der Waals interaction between the dye and the semiconductor.[1,22] Because the surface is nearly atomically flat, the area occupied for each molecule can be approximated to be about 350 $Å^2$ from the surface dye concentration at monolayer coverage. This number is much larger than the molecular area of 135 $Å^2$ for a flat dye molecule[23] estimated using the van der Waals radii of the atoms or an area of 197$Å^2$ measured for MB^+ on Graphon[24]. This discrepancy can be explained as due either to a QYAP smaller than 1 or that the dye molecules are not close-packed on the surface. The

Table 3.4 Adsorption Isotherm Parameters for MB^+ adsorbed on freshly cleaved SnS_2.

	Methylene Blue/ Unetched SnS_2
K (μM^{-1})	0.163 ± 0.008*
C_m (Molecules/cm^2)	(2.84 ± 0.04) E+13
C_mK (Å)	(7.69 ± 0.49) E+5
ΔH (Kcal/mole)	-7.04 ± 0.04
$IPCE_{max}$	0.341 %
Area/Molecule	3.52 $Å^2$

* The error listed for each parameter is the fitting uncertainty.

positive charge associated with the dyes studied may preclude close-packing due to Coulomb repulsion forces. Above, we estimated that the QYAP, using the dye sensitized IPCE and dye surface absorbance, was more than 44% for MB^+ on smooth SnS_2. Taking this factor into account results in the minimum surface area occupied by each dye molecule to be 155 $Å^2$, very close to the close-packing value. Again the error involved in the absorbance measurement and the assumption that the dry coverage is equal to the coverage in solution does not allow us to state unequivocally if the QYAP is actually less than 1 for MB^+. It is also possible that the saturation coverage is less than close-packed or that all dye molecules are not injecting electrons efficiently. Because the calculated molecular area was close to the actual close-packed value and electron injection is generally efficient in dye sensitized systems, we presume that the QYAP is less than 1.

Selective Photoxidation. The selective removal of MB^+ from the surface can be explained by the established kinetic scheme for dye sensitization, i.e., when the electrode/electrolyte interface is illuminated with relatively intense excitation light (~2 mW), adsorbed MB^+ molecules are excited and electrons are transferred to the semiconductor conduction band. The adsorbed dye molecules are photoxidized at a much faster rate than they can be regenerated when there is no regenerating agent in solution. If the excitation and electron injection are fast enough, the photocurrent can be completely diminished, as we observe for the system reported here. When the laser is turned off, we observe the photocurrent signal recover. This can be attributed to desorption of the oxidized

dye (MB^+) and readsorption by MB^+ from solution. Another explanation could be electron transfer from MB^+ molecules in solution to the oxidized dye molecules on the surface. Because the recovery time of the sensitization current after MB^+ photoxidation (45 minutes) is found to be close to the time for adsorption equilibrium to be established (~30 minutes) the rate limiting step must be related to the adsorption of MB^+. As mentioned in the experimental section, the time to establish the adsorption/desorption equilibrium for CV^+ is much shorter than a minute compared to about 30 minutes for MB^+. Therefore, a possible reason that we only observe depletion of MB^+ with irradiation at either wavelength is that the desorption and readsorption of CV^{2+}, the oxidized form of CV^+, is diffusion controlled while MB^+ has much slower adsorption kinetics.

At this point we cannot rule out that excited CV^{+*} could transfer energy to a nearby adsorbed MB^+ prior to electron injection into the semiconductor conduction band or that electron transfer from a nearby MB^+ to the photoxidized CV^{2+} could occur after electron injection. If the excited state potential of the dye is approximated by its reduction potential[22] (Table 3.3) then the excited state potential for CV^+ would be about 45 mV more negative than that of MB^+. This would allow for excited state electron transfer from CV^{+*} to MB^+. The oxidation potential of CV^+ is also more positive by 200 mV (Table 3.3) than the oxidation potential of MB^+, so dark electron transfer from MB^+ to CV^{2+} would also be possible. Either of these electron transfer events could induce the selective photoxidation of MB^+ when both dyes are on the surface.

To further probe the photobleaching process, we performed an additional "hole burning" experiment using only CV^+ on the electrode in the absence of H_2Q. For this experiment, the sensitization signal recovered approximately 30 seconds after the laser was turned off. Thus, it appears that the kinetics for regenerating adsorbed CV^+ is fast enough, that even with 2 mW (beam diameter of about 5 mm) of laser power no depletion of the dye from the surface was observed in the experimental time scale (total of 1 minute in this case). Further "hole burning" experiments were performed with only MB^+ on the surface and in solution; these studies resulted in the same fast depletion (~1 minute) and slow recovery (>30 minutes).

Impedance and Photocurrent Voltage Measurements. The effects of solution composition on the flat band potential and the shape of the current voltage curve were studied with impedance and photocurrent voltage techniques, respectively. Impedance measurements, Figure 3.8, show the flat band potential (E_{FB}) shifted to more positive potentials when H_2Q was added to solution and then shifted to even more positive potentials after the subsequent addition of MB^+. It is possible that both H_2Q and MB^+ cause slight negative shifts due to their adsorption on the SnS_2 surface, or that they quench some near-edge surface states. These shifts will likely affect the driving force for both electron injection and recombination events in the dye sensitization process. Further work should focus on the SnS_2 response when AZB^+, OX^+ and CV^+ are each individually added to solution. If larger shifts are generated by OX^+ and

CV^+ addition, then the faster recombination could be justified because the $CV^{+/2+}$ potential could be closer to the SnS_2 conduction band edge.

Photocurrent voltage curves, Figure 3.5 and Figure 3.6, show the photoelectrochemical behavior of H_2Q, MB^+, CV^+ and SnS_2 in an electrolyte solution. The photocurrent voltage curve resulting from 514 nm excitation with H_2Q in solution, Figure 3.5, was assumed to arise from SnS_2 band gap excitation. When MB^+ was added to the regenerator/electrolyte solution, a 10 mV negative $E_{1/2}$ shift was observed in the photocurrent voltage curve for 514 nm excitation. This second curve had a much slower increase in the photocurrent than the previous one, which was most likely due to electron capture resulting from both MB^+ electron injection and SnS_2 band gap excitation. The MB^+ sensitized photocurrent voltage curve, resulting from 689 nm excitation, had a $E_{1/2}$ that was 70 mV more negative than the SnS_2 band gap illumination curve. This may be due to both the energetically favorable driving force for electron injection from MB^+ into the SnS_2 conduction band and the fact that SnS_2 has an indirect band gap transition. Due to the indirect band gap transition of SnS_2, band gap excitation results in carriers outside of the space charge region so a larger field is required to capture more electrons.[25] This agrees with the reported fast electron injection rates from the dye excited state into the SnS_2 conduction band.[15,26] The MB^+ sensitized photocurrent voltage curve at 689 nm also shows a much weaker photocurrent response compared to that for SnS_2 band gap excitation at 514 nm, which agrees with all previous IPCE results.

Comparing the MB^+ and CV^+ sensitized photocurrent curves, Figure 3.6, reveals that CV^+ has both a lower IPCE, as observed previously, and a $E_{1/2}$ that is 70 mV more negative. From these results, electron injection from CV^+ was energetically more favorable, but the subsequent electron escape in the SnS_2 conduction band was less favorable than for MB^+. In addition, the CV^+ photocurrent curve increases with a steeper slope than for MB^+, indicating that non-geminate recombination and recombination with centers other than the parent-type dye molecules occurred less frequently. Geminate recombination may account for the low IPCE. This agrees with the kinetic results of Lanzafame et al.[15] for oxazine on SnS_2 where an electron injection rate of 40±20 fs was measured and the back electron transfer rate was 1-10 ps. Further work by Xu et al.[26] on SnS_2 determined both that the electron lifetime in the conduction band was shorter than 60 fs and that surface states may be involved in the back reaction. This implies that favorable electron injection into the semiconductor conduction band does not necessarily dictate a high IPCE.

The Effects of Surface Composition on the Dye Sensitized IPCE. Dye sensitization results for MB^+, AZB^+, OX^+ and CV^+ were analyzed to further understand dye sensitization of SnS_2 electrodes. The different photoresponses suggest that the individual dyes may have distinct adsorption behavior, electronic recombination losses, or a combination of both. The adsorption behavior and the electronic recombination processes were evaluated with IPCE measurements of SnS_2 with various carrier concentrations, SnS_2 soaked in

dodecanethiol solution and SnS_2 annealed in a sulfur atmosphere, as well as with adsorption studies and photocurrent voltage curves.

In order to study both the effects of the electric field gradient and the concentration of surface chloride related dye adsorption sites on the dye sensitized IPCE, SnS_2 single crystals were grown with carrier concentrations ranging from $4x10^{15}$ to $1.09x10^{18}$ cm^{-3} (Table 3.2 and Chapter 2.) The SnS_2 carrier concentration will affect the space charge width and dopant atoms near the surface may also provide binding sites with different adsorption energies for dye molecules. There was, however, no strong correlation between carrier concentration and the photosensitization signal for MB^+, AZB^+, OX^+ and CV^+. This indicates that the dopant atoms near the SnS_2 surface do not provide different binding sites for dye molecules. In addition, it appears that carrier concentrations in the region of $1x10^{15}$ - 10^{18} cm^{-3} do not play a pivotal role in the dye sensitization quantum efficiency.

The dye sensitized IPCEs on SnS_2 with varying carrier concentrations were also analyzed in terms of the one dimensional Onsager model for dye sensitized charge injection into semiconductors developed by Spitler[27] (Chapter 1.) This model takes into account current originating in the bulk of the semiconductor that can overcome the surface potential barrier and reach the oxidized dye or other acceptor at the surface. This current reflects the product of the bulk electron concentration in the conduction band and its thermal velocity. Analysis of the data from photoaction spectra (Table 3.2) shows that there was no

significant correlation between the carrier concentration and the dye sensitization quantum efficiency, in the range mentioned above. This agrees with Spitler's work[27] reporting that the current voltage curves depend weakly on thermalization distance, although he assumed that the ratio of the rate of electron recombination compared to the rate of escape was small (0.07). When the rate of electron recombination becomes very large, the thermalization length affects the photocurrent voltage curves as may be the case for our system.[27] It is possible that the effects of the carrier concentration on the dye sensitized IPCEs were not detected because of the large potential barrier applied, as photoaction spectra were measured at a bias of 0.7 V vs Ag/AgCl. In addition, Spitler[27] used semiconductors with carrier concentrations of 10^{18} cm^{-3} while we used SnS_2 with $6.4x10^{16}$ cm^{-3} Cl^-.

Another study involved annealing SnS_2 samples in an atmosphere of sulfur to fill in sulfur vacancies or defect sites that may be present on the van der Waals surfaces. Annealing may also reduce the effects of strain and damage in the crystal that result from breaking up the large crystal boules obtained from the Bridgman growth to construct SnS_2 electrodes. Results diagrammed in Figure 3.12 show that annealing enhanced the dye sensitized IPCE for MB^+, AZB^+ and OX^+, while producing conflicting results for CV^+. Annealed samples with lower carrier concentrations, $2.3x10^{17}$ cm^{-3} Cl^-, yielded a four fold enhancement of the AZB^+ sensitized IPCE, a three-and-a-half fold enhancement for MB^+ and a two fold enhancement for OX^+. However, the CV^+ sensitized

IPCE for annealed samples yielded a slight increase for the $2.3x10^{17}$ cm^{-3} Cl^- samples or a three fold decrease for the $4.2x10^{17}$ cm^{-3} Cl^- samples.

The three-and-a-half fold enhancement of the MB^+ IPCE after annealing is possible, although the QYAP was calculated to be 44%, due to experimental error, an increased dye surface concentration and a decreased number of both traps and recombination centers. If vacancies and defect sites act as traps and recombination centers, then a decrease in the number of sites would potentially enhance the dye sensitized IPCE as seen for MB^+, AZB^+ and OX^+. The increased dye sensitized IPCE may also be due to an increase in the dye surface concentration if the adsorption orientation was altered. The dyes all have similar molecular structures, as shown in Figure 3.2, although CV^+ is slightly larger with an additional benzene ring. The decreased CV^+ signal after annealing may also be attributed to the destruction of favorable dye adsorption sites for CV^+.

Both the annealing and carrier concentration studies revealed similar trends in the maximum dye sensitized IPCE signal for MB^+, AZB^+, OX^+ and CV^+. Of these four dyes MB^+ always has the largest sensitized IPCE followed by AZB^+. Whether the OX^+ or CV^+ IPCE is larger varies depending on the system but they are never larger than MB^+ or AZB^+. To explain the trends in the IPCEs of the four dyes studied, we focus on several dye characteristics, including the dye excited state lifetimes, and dye oxidation potentials and dye reduction potentials, which are assumed to be within 50-100 mV of the potential of the dye excited state[30]. The first oxidation and reduction potentials for the four dyes[7] are

diagrammed in Figure 3.13. The SnS_2 potential energy levels were estimated[31,32] using the flat band potential determined from the Mott-Schottky plots (Figure 3.8). Work by the groups of Grätzel[33], Willig[13,34], Nozik[35] and Miller[15,26] revealed that electron injection from an excited dye molecule into the conduction band of a semiconductor occurred on time scales on the order of fs. The electron injection for OX^+ into SnS_2 was on the order of 40±20 fs[15] and less than 10 ps[14] for CV^+ on SnS_2. Thus, the dye sensitization efficiency was presumably not limited by this step. Furthermore, it was also shown (Table 3.3) that OX^+ had an IPCE lower than both MB^+ and AZB^+, although it also had the most negative reduction potential. However, the four dyes investigated all had first reduction potentials more negative than the conduction band edge. Thus, it was presumed that there was not a significant correlation between the dye reduction potential and the dye sensitized IPCE, assuming the dye first reduction potential was more negative than the conduction band edge. This was supported by photoelectrochemical results. For example, Figure 3.6 shows that CV^+ has a weaker sensitized photocurrent signal but a more negative $E_{1/2}$ than MB^+. The dye oxidation potential, however, showed a slight correlation with the dye sensitized IPCE. Both MB^+ and AZB^+ have larger sensitized IPCEs and oxidation potentials more negative than OX^+ and CV^+. These results contradicted work on SnS_2 by Parkinson[7], which showed the opposite trend for organic dyes with oxidation potentials ranging from approximately 0.2 - 1.4 V vs Ag/AgCl. However our study only used dyes within a limited range of oxidation potentials, 1.15 - 1.35 V

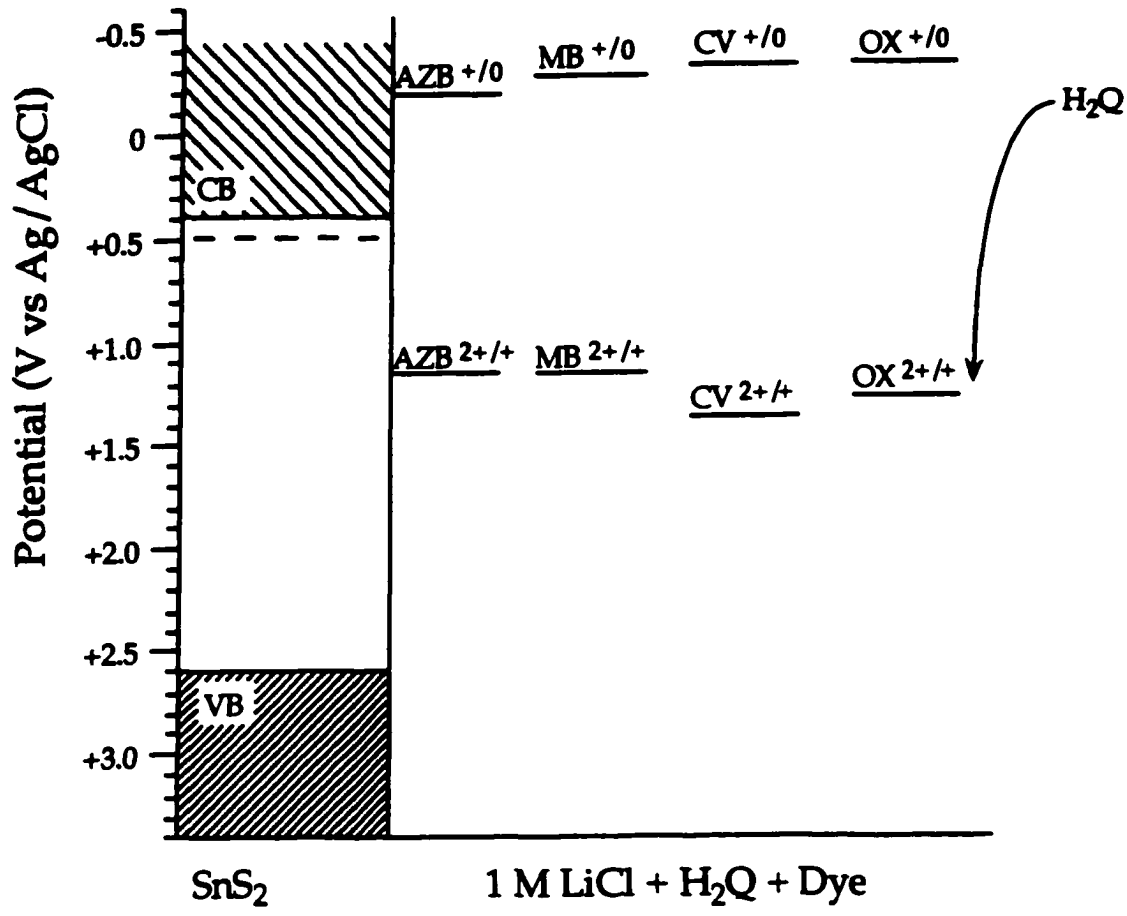

Figure 3.13. Diagram of the potential energy levels of SnS_2, H_2Q and the first oxidation and reduction potentials of AZB^+, MB^+, CV^+ and OX^+ vs Ag/AgCl. The dye energy levels should all be positioned at the SnS_2 surface, however this was not possible for the diagram.

vs Ag/AgCl, and there was a substantial degree of scatter over this potential range in the work by Parkinson[7]. In addition, two anomalies were noticed in our results. First, the OX^+ oxidation potential is more negative than for CV^+, although the OX^+ sensitized IPCE was not always larger than for CV^+. Second, the oxidation potentials of MB^+ and AZB^+ are nearly identical although MB^+ had a higher sensitized IPCE. This disparity in the dye IPCEs indicates that more than one factor influences the sensitization efficiency. Trends in the IPCEs may reflect both different recombination pathways and differences in adsorption behavior.

CONCLUSION

We have further investigated the fundamentals of the dye sensitization processes with the two-dimensional metal dichalcogenide semiconductor, SnS_2. Experimental evidence showed that both CV^+ and MB^+ have higher sensitization photocurrents near edges and defects. We are not certain if the edge provides special (stronger) binding sites for the dye molecules or allow the dye molecules to intercalate between the layers through the exfoliated cross-sectional surface on the edge. Nevertheless, increasing the surface area and/or the interaction between the dye and the surface by creating more active sites will be expected to increase the dye sensitized quantum yields.

It was also shown that the regeneration of photoxidized dye molecules (MB^+ and CV^+) on the SnS_2 surface occurred either through electron self

exchange or the adsorption/desorption process in the absence of reduction by an externally added regenerating agent. These studies showed that MB^+ and CV^+ have different adsorption/desorption kinetics as well as excited state properties. The selective photoxidation of MB^+ from the surface when both dyes were present was attributed to the slower adsorption/desorption kinetics of MB^+ compared to CV^+. No conclusive evidence for electron or energy transfer between the two simultaneously adsorbed dyes was found. Modeling the adsorption isotherm using a Langmuir isotherm for MB^+ on the van der Waals surface of SnS_2 yielded a reasonable value for the area occupied by each dye molecule.

Analysis of the dye sensitization efficiencies for MB^+, AZB^+, CV^+ and OX^+ showed that IPCE values for these dyes were unaffected by the SnS_2 carrier concentration when using Cl^- as a dopant within a range of $1x10^{16}$ - $1x10^{18}$ cm^{-3}. Preliminary work with different dopant atoms (Se and As) also showed no significant changes in the dye sensitized IPCEs. It was also determined that of the dyes studied, MB^+ had the greatest IPCE, followed by AZB^+ and then CV^+ and/or OX^+. Analysis of the data revealed that there was no evidence of a correlation between the reduction potential and the dye sensitized IPCE as CV^+ and OX^+ both had a greater driving force for electron injection than MB^+ and AZB^+ but lower sensitized IPCEs. In addition, MB^+ and AZB^+ have similar oxidation potentials and reduction potentials that are both more negative than the conduction band edge, but the IPCE of MB^+ was greater than that for AZB^+.

This was explained by recombination loses and different adsorption behavior due to special binding sites or the formation of three-dimensional dye islands. An additional dye characteristic that may affect the dye sensitization process is the higher quantum yield for triplet state formation by MB^+ and AZB^+ compared to OX^+ and CV^+.[9,10,16]

A correlation between the SnS_2 sulfur composition and the dye sensitized IPCE was established through annealing experiments. The enhanced dye sensitized IPCE observed after annealing may be attributed to a decrease in the number of traps that are pathways for recombination. Both the differences in the degree of dye sensitization enhancement and the decrease in the CV^+ efficiency may be due to the different potentials for injected electrons around the oxidized dyes that allow for different recombination probabilities for injected electrons at van der Waal and defect sites. These defect sites or vacancies that influence the recombination losses and, thus, the dye sensitized IPCE, may be sulfur sites adjacent to the surface as both thiol addition and variations in the carrier concentration did not greatly influence the dye efficiency, while annealing SnS_2 samples did.

Photocurrent voltage curves and impedance measurements showed that recombination affects the sensitization IPCE of the dyes. Impedance measurements revealed that the flat band potential shifted to more positive potentials upon adsorption of H_2Q and MB^+, which may affect the driving force for recombination. Photocurrent voltage curves revealed that CV^+ had a more

negative $E_{1/2}$ than MB^+ but a lower dye sensitized IPCE. This indicated that while electron injection into the SnS_2 conduction band was energetically more favorable for CV^+ than MB^+, recombination losses were also more favorable for CV^+. Photocurrent voltage curves also showed a slow rise with increasing applied potential that is indicative of a competition between electron escape and recombination. This agrees with the observations from the dye sensitized IPCE studies where CV^+ and OX^+ had a greater driving force but a smaller sensitization efficiency than MB^+. In addition, time resolved measurements by Miller and coworkers[15,26] support these observations as electron injection rates into the SnS_2 conduction band for OX^+ on SnS_2 were on the order of fs while the back electron transfer for OX^+ was 1-10 ps and the electron lifetime in the conduction band was less than 60 fs. Thus, the electron escape process would have to be extremely fast to compete with these injection and recombination rates.

The following chapter continues with this work through the analysis of photoelectrochemically etched SnS_2 surfaces. Future work should include additional adsorption isotherm measurements utilizing the procedure by Spitler[36] and STM studies to determine the actual structure of the adsorbed dyes. Time resolved measurements are also necessary as it is difficult to deduce an injection-recombination potential diagram solely on the basis of stationary current measurements.

REFERENCES

1 Gerischer, H. *Photochem. Photobiol.* **16,** 241 (1972).

2 Memming, R. *Photochem. Photobiol* **16,** 325 (1972).

3 Kay, A. and Grätzel, M. *J. Phys. Chem.* **97,** 6272 (1993).

4 Enea, O.; Moser, J. and Grätzel, M. *J. Electroanal. Chem.* **259,** 59 (1989).

5 Vlachopoulos, N.; Liska, P.; Augustynski, J. and Grätzel, M. *J. Am. Chem. Soc.* **110,** 1216 (1988).

6 Spitler, M. and Parkinson, B. A. *Langmuir* **2,** 549 (1986).

7 Parkinson, B. A. *Langmuir* **4,** 967 (1988).

8 Parkinson, B. A., In *Electrochem. Soc. Proc.* **160** 88 (1988).

9 Asimov, M. M.; Gavrilenko, V. N. and Rubinov, A. N. *J. of Luminescence* **46,** 243 (1990).

10 Kreller, D. I. and Kamat, P. V. *J. Phys. Chem.* **95,** 4406 (1991).

11 Blanchard, G. J. *Chem. Phys.* **138,** 365 (1989).

12 Kamat, P. V. *J. Chem. Soc., Faraday Trans. 1* **81,** 509 (1985).

13 Eichberger, R. and Willig, F. *Chem. Phys.* **141,** 159 (1990).

14 Willig, F.; Eichberger, R.; Sundaresan, N. S. and Parkinson, B. A. *J. Am. Chem. Soc.* **112,** 2702 (1990).

15 Lanzafame, J. M.; Miller, R. J. D.; Muenter, A. A. and Parkinson, B. A. *J. Phys. Chem.* **96,** 2820 (1992).

16 Danziger, R. M.; Bar-Eli, K. H. and Weiss, K. *J. Phys. Chem.* **71,** 2633 (1967).

17 Natoli, L. M.; Ryan, M. A. and Spitler, M. T. *J. Phys. Chem.* **96,** 2820 (1985).

18 Sonntag, L. P. and Spitler, M. T. *J. Phys. Chem.* **89,** 1453 (1985).

19 Parkinson, B. A. , unpublished results.

20 Spitler, M. T. *J. Phys. Chem.* **90,** 2156 (1986).

21 Günther, E. and Moisar, E. *J. Photograph. Sci.* **13,** 280 (1965).

22 Spitler, M. T. and Calvin, M. *J. Chem. Phys.* **66,** 4294 (1977).

23 Kipling, J. J. and Wilson, R. B. *J. Appl. Chem.* **10,** 109 (1960).

24 Graham, D. *J. Phys. Chem.* **59,** 896 (1959).

25 Tan, M. X.; Laibinis, P. E.; Nguyen, S. T.; Kesselman, J. M.; Stanton, C. E. and Lewis, N. S., In *Progress in Inorganic Chemistry,* Vol. 41, Karlin, K. D., Ed. (John Wiley & Sons, Inc, New York, 1994), pp. 21.

26 Xu, S.; Miller, C. C.; Dol, S. J.; Gao, Y.; Mantell, D. A.; Mason, M. G.; Muenter, A. A.; Sharp, L. I.; Parkinson, B. A. and MIller, R. J. D. *Chem. Phys. Lett.* **272,** 209 (1997).

27 Spitler, M. T. *J. Electroanal. Chem.* **228,** 69 (1987).

28 Misran, M.; Matthews, D.; Valente, P. and Hope, A. *Aust. J. Chem.* **47,** 209 (1994).

29 Sagara, T. and Niki, K. *Langmuir* **9,** 831 (1993).

30 Ryan, M. A. and Spitler, M. T. *Journal of Imaging Science* **33,** 46 (1989).

31 Morrison, S. R. *Electrochemistry at Semiconductor and Oxidized Metal Electrodes* (Plenum Press, New York, 1980).

32 Finklea, H. O., In *Studies in Physical and Theoretical Chemistry,* Vol. 55, Finklea, H. O., Ed. (Plenum, New York, 1988), pp. 1.

33 Tachibana, Y.; Moser, J. E.; Grätzel, M.; Klug, D. R. and Durrant, J. R. *J. Phys. Chem.* **100,** 20056 (1996).

34 Hannappel, T.; Burfeindt, B.; Storck, W. and Willig, F. *J. Phys. Chem. B.* **101,** 6799 (1997).

35 Ellingson, R. J.; Asbury, J. B.; Ferrere, S.; Ghosh, H. N.; Sprague, J. R.; Lian, T. and Nozik, A. *J. Phys. Chem. B* **102,** 6455 (1998).

36 Spitler, M. T. and Calvin, M. *J. Chem. Phys.* **67**, 5193 (1977).

CHAPTER 4

Increasing the Dye Sensitization Efficiency of SnS_2 Photoanodes through Photoelectrochemical Etching

INTRODUCTION

Dye sensitization is the phenomenon underlying both the photographic process and photoelectrochemical solar cells and is based on the interaction of dye molecules adsorbed on and interacting with surfaces. Recent improvements in the quantum efficiency for the sensitization of semiconductor electrodes have provided hope that dye sensitization may be of use for increasing the efficiency of photoelectrochemical solar energy conversion processes.

The increases in sensitization efficiency have progressed on two fronts. The first, pioneered by Grätzel and coworkers[1] uses high surface area TiO_2 electrodes that have their surfaces modified with covalently bonded chromophores to extend the wavelength response of TiO_2 into the visible region of the spectrum. They have achieved impressive incident photon to current efficiency (IPCE) of greater than 80% at some wavelengths.[2-4] The other front uses two-dimensional chalcogenides as the semiconductor substrate.[5-7] These materials have shown large dye sensitized quantum yields per absorbed photon

(QYAP up to 80%) at some wavelengths. The high yields have been attributed to the lack of trapping sites for photogenerated carriers on the surface.[5,7] However, the total yield (IPCE) is rather low for this system because of the low light absorption by a monolayer of dye on the very flat surface.

In Chapter 3, we reported that larger IPCEs for dye sensitization can be measured near the step edges of a freshly cleaved electrode and that sensitization yields are reduced for singlet dyes on more defect free SnS_2 surfaces. Two factors that may contribute to this effect are: 1), an increased surface area resulting from the surface roughness, and 2), stronger binding sites for the dye molecules, which affords stronger electronic coupling to the semiconductor, due to the exposure of the non-van der Waals surfaces. Modification of the electrode surface to expose more edge sites might be expected to increase the dye adsorption and consequently improve the overall incident photon to current efficiency (IPCE). One of the problems, however, is the possible creation of more trapping sites for the photogenerated carriers, which could decrease the QYAP, and thus limit the overall IPCE. Chemically etching the van der Waals surface of the electrode could produce more edge sites in a controlled fashion. However, the layered materials, by their nature, are very anisotropic. Thus layered materials would be expected to have a faster rate of the etching reaction along the layers rather than perpendicular to the layers, resulting in the sequential peeling off of layers instead of exposing more cross-sectional area. Therefore, a driving force for reaction perpendicular to the layers has to be introduced.

It has been shown by Tenne et al.[8] that photoelectrochemical etching (PEC etching or photoetching) of some layered semiconductors (such as WSe_2) creates hexagonal etch pits exposing non-van der Waals surfaces. Furthermore, they postulate that the number of recombination centers on the surfaces was reduced after PEC etching resulting in enhanced band gap photoresponses.[9-14] In the work presented here, we have used a similar PEC etching technique to that used by Tenne et al.[15] to study the dependence of the ZnSe and CdS photoetching morphology on the irradiation wavelength. The dye sensitized photocurrent response and the band gap photocurrent response on the PEC etched surfaces are investigated and compared to unetched surfaces.

The adsorption isotherms for MB^+ and CV^+, the HCl photoetching and the photocurrent stability experiments were carried out by Xiumei Dou, a former post doctoral fellow in the Parkinson research group. Chapter 4 focuses on photoetching studies. Overall, PEC etching is shown to increase the dye sensitized IPCE for the organic dyes studied, the conditions for PEC etching are analyzed to improve the dye sensitization efficiency and the factors that contribute to this enhancement are also studied.

EXPERIMENTAL METHODS AND MATERIALS

The photoelectrochemical etching of various single crystal SnS_2 electrodes was carried out in a three electrode cell in 1 M HCl, 5 M NaOH or *aqua regia*, using a platinum counter electrode and an SCE reference electrode. During

illumination, the semiconductor electrode was maintained under a reverse bias (0.7-1.0 V vs SCE). PEC etching was a result of photogenerated holes oxidizing the SnS_2.[16-18] The anodic decomposition of SnS_2 in 1 M HCl resulted in a soluble $SnCl_6^{2-}$ species and elemental sulfur (Equation 4.1). In 5 M NaOH, anodic decomposition produced stannate (SnO_3^{2-}) and unidentified soluble sulfur species, presumably, sulfite or sulfate (Equation 4.2).

$$6\,Cl^- + SnS_2 + 4\,h^+ \rightarrow SnCl_6^{2-} + 2\,S \qquad (4.1)$$

$$18\,OH^- + SnS_2 + 12\,h^+ \rightarrow SnO_3^{2-} + 2\,SO_3^{2-} + 9\,H_2O \qquad (4.2)$$

The electrodes PEC etched in 1 M HCl were treated with CS_2 after PEC etching to remove the residual sulfur from the surface. The PEC etching potential was controlled with a PAR 174A or 173 potentiostat and the total charge was recorded by an Electrosynthesis Corporation Model 680 digital coulometer or a PAR 175 coulometer. Three sources of illumination were used for PEC etching: first, the focused full output of an Oriel 6137 150-W xenon lamp outfitted with or without a water filter and sometimes coupled with an exposure mask; second, the white light output of an Oriel 77503 fiber optic illuminator, and third, the 488 or the 514 nm line of an Ion Technology Model 400 air cooled argon ion (Ar^+) laser. The photocurrent was primarily responsible for the etching of cleaved surfaces because passage of a similar number of coulombs of dark current had a negligible effect on the surface. Both the xenon lamp and the fiber optic illuminator beams irradiated the entire surface of the electrode. Because the light intensities of the two white light sources were fairly large (~ 10 mW m^{-2}), the

dark current was negligible compared to the photocurrent. When PEC etching the entire electrode, the extent of etching was monitored by the total charge passed through the electrode. For some of the PEC etching experiments in NaOH, the electrode was exposed to light from the arc lamp filtered through a step wedge exposure mask to simultaneously investigate the effect of many different exposures. The step wedge mask varied from transparent to about 1% of full exposure. The relative exposure of each wedge was determined with a diode laser by measuring the power in and the power out at 680 nm. The extent of PEC etching with the Ar^+ laser was monitored by recording both the total charge passed and the time of photoetching. This was necessary as the Ar^+ laser light beam illuminated only an area of approximately 1 mm^2, a small portion of the sample surface, and the dark current from the entire surface was comparable to the photocurrent.

The photoelectrochemical measurements were performed as described in Chapter 3. All of these experiments used a 1 M LiCl in methanol electrolyte solution. The SnS_2 single crystals were grown with the Bridgman method as described in Chapter 2. Scanning electron microscope (SEM) micrographs of PEC etched surfaces were performed with a Philips 505 SEM equipped with an energy dispersion spectrometer (EDS). The electron beam energy was 15-20 keV. The surface morphology of both cleaved and lightly photoetched SnS_2 were studied with Atomic Force Microscopy (AFM). A Digital Nanoscope III AFM was used to image the SnS_2 surfaces using triangular silicon noncontact Ultralevers with a

spring constant of 18 N/m from Park Scientific Instruments.

RESULTS

SEM of Photoetched Surfaces. PEC etching of SnS_2 electrodes with a xenon lamp in 1 M HCl resulted in uniform matte dark-gray surfaces after washing with CS_2. Figures 4.1a and b show SEM micrographs of both undoped and chloride-doped electrodes, respectively, prepared with the same PEC etching condition in HCl (2.6 C/cm^2). The micrographs show ring-like structures approximately 1.5 μm wide on the roughened surfaces. The density per unit surface area of the ring like structures was larger in the doped versus the undoped sample. This agrees with observations on WSe_2 by Tenne et al.[17] where an increase in the number of PEC etch pits was observed on samples with higher dopant concentrations. The SnS_2 surfaces photoetched with a xenon lamp in 5 M NaOH were also uniform, matte and dark gray to light yellow in color, but unlike the HCl photoetched surfaces, the EDS analysis showed no sign of excess sulfur on the surface after PEC etching and, thus, CS_2 treatment was unnecessary. Figures 4.1c and d show the SEM micrographs of chloride-doped SnS_2 for two different photoetching conditions in 5 M NaOH. They show different porous "network" structures compared to the ring like structures (Figures 4.1a and b) with pores of a few microns in width. The more extensively photoetched surfaces, shown in Figure 4.1d, had deeper pores than the other photoetched surfaces shown. Figure 4.1e shows an edge view of the NaOH photoetched

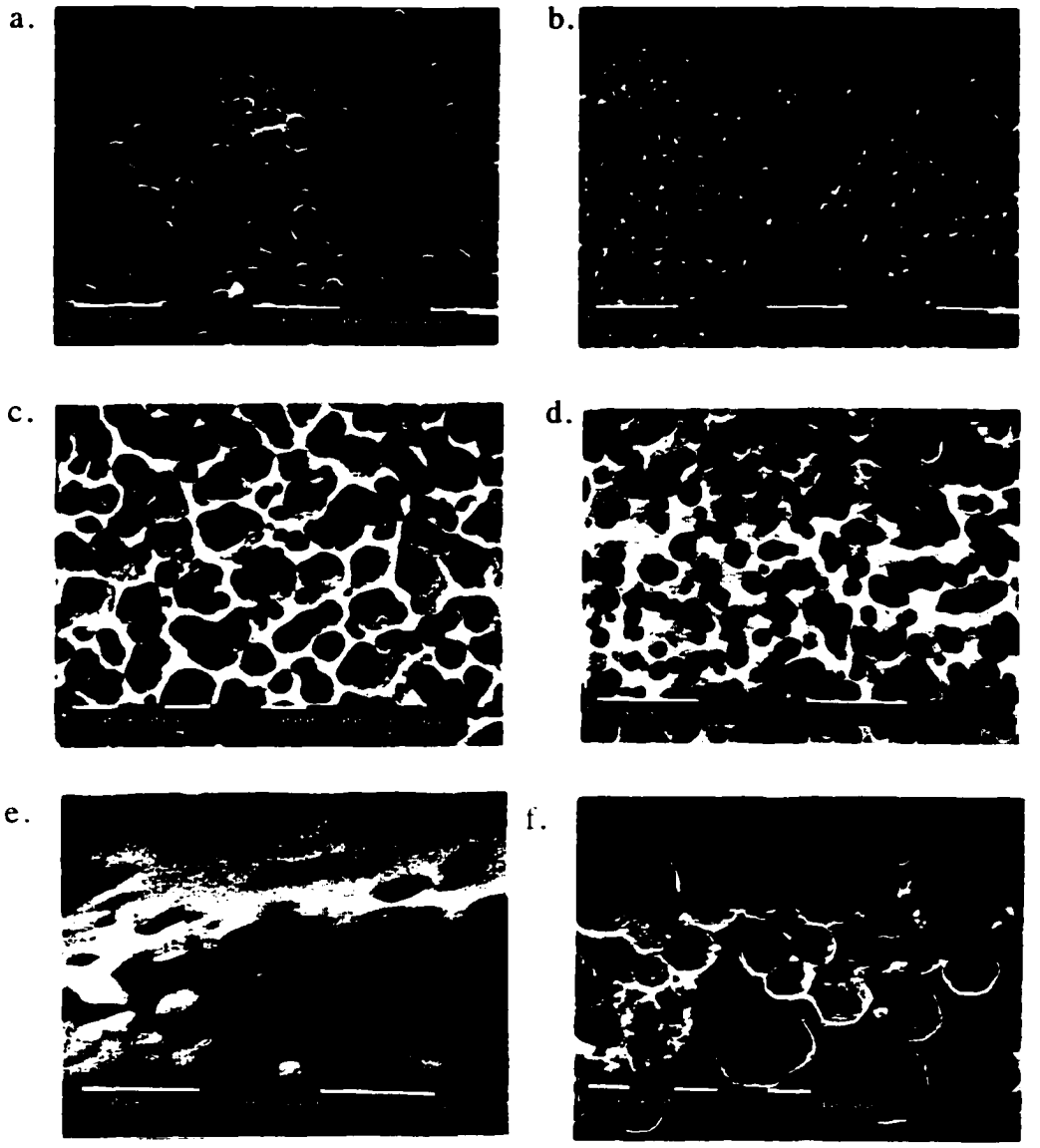

Figure 4.1. Scanning electron microscope (SEM) micrographs of SnS_2 surfaces photoetched with a xenon lamp. Unless otherwise indicated the SnS_2 had 8.0×10^{16} Cl^- atoms/cm^3. The magnification, 1200x - 4580x, is indicated in each micrograph. The energy of the electron beam was 15 - 20 keV. a) Unintentionally doped SnS_2 photoetched in 1 M HCl with 2.6 C/cm^2 of total charge passed. The PEC etching potential was 1.0 V vs SCE. b) SnS_2 photoetched under the same conditions as in (a). c) SnS_2 photoetched in 5 M NaOH with 14 C/cm^2 of total charge passed and a PEC etching potential of 0.7 V vs SCE. d) SnS_2 photoetched in 5 M NaOH with 31 C/cm^2 of total charge passed at a PEC etching potential of 2.0 V vs SCE. e) Cross sectional view of the SnS_2 electrode in (d). f) SnS_2 chemically etched in *aqua regia* for 21 hours.

surface from 4.1d. The edge view reveals posts of unetched material with many gaps due to missing layers between unetched layers. This "parking garage" structure results in a large increase in the areas of both edge sites and van der Waals surfaces.

Immersing SnS_2 in *aqua regia* for 21 hours resulted in very shallow hexagonal etch pits as shown in Figure 4.1f. We presume that attack from chemical oxidants in solution produced shallow etch pits due to the preferential attack at edge sites and the difficulty of nucleating a pit on an unetched layer. This behavior is in contrast to photogenerated oxidants (holes in the valence band) that produced photoetch pits deep into the material, presumably due to the oxidant being produced deep in the material from the penetration depth of the light. Absorption coefficient measurements of SnS_2[19] showed that the average light penetration depth was 0.1 μm at a wavelength of 400 nm, 1 μm at 480 nm, 10 μm at 530 nm, and 100 μm at 570 nm.

Improved Dye Sensitized IPCE. Tin disulfide electrodes photoetched with a xenon lamp in 1 M HCl showed a large improvement in the dye sensitized photocurrent response as shown in the photocurrent spectra in Figure 4.2. This figure also shows the photocurrent spectrum on unetched surfaces (cleaved surface of the same electrode) for comparison. The photocurrent was measured under the same conditions for both photoetched and unetched surfaces. Because cresyl violet (CV^+) had a smaller sensitized photocurrent than methylene blue (MB^+), photocurrent spectra taken when the SnS_2 electrode was either

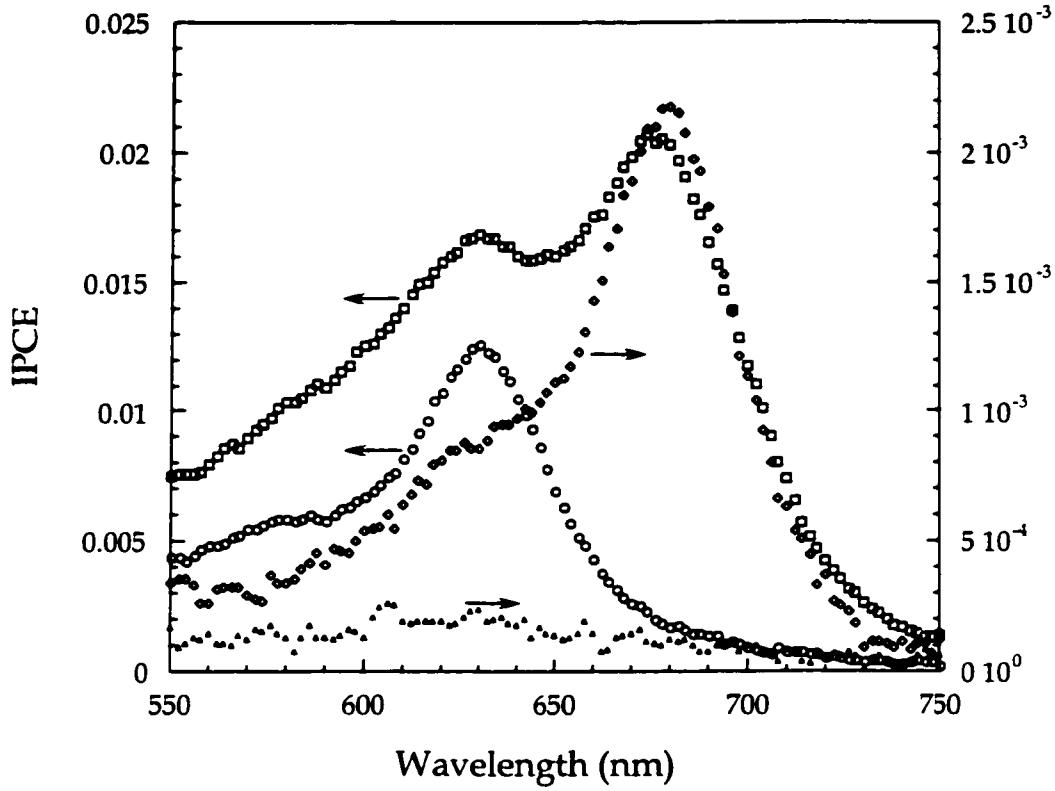

Figure 4.2. Photoaction spectra of CV^+ (5 μM) and a solution of both CV^+ and MB^+ (5 μM each) on a SnS_2 electrode ($8.0x10^{16}$ Cl^- atoms/cm^3) at two different surface conditions, photoetched and cleaved. The photoaction spectrum with both MB^+ and CV^+ was achieved by adding MB^+ to the CV^+/regenerator/electrolyte solution, after the CV^+ photoaction spectrum was measured. Photoaction spectra were first measured for the photoetched SnS_2 electrode in a solution of CV^+ (circles) and then in a solution of both CV^+ and MB^+ (squares). The electrode was then cleaved and photoaction spectra taken in the same manner (triangles and diamonds, respectively). The photoetching was carried out in 1 M HCl with a xenon lamp and the SnS_2 electrode biased 1.0 V vs SCE with 1 C/cm^2 of total charge passed. The photoaction spectra were taken in 1 M LiCl/methanol solution with 30 mM H_2Q as regenerator and the electrode was biased 0.7 V vs Ag/AgCl .

photoetched or cleaved were first measured for 5 μM CV^+. Then an equal amount of MB^+ was added to solution and the photocurrent response with both dyes present in solution was measured. The regenerating agent in the solution was 10 mM hydroquinone (H_2Q) and the total charge passed during PEC etching was 1 C/cm^2. Because the anodic decomposition reaction in acidic solution was predicted to involve 4 h^+ (Equation 4.1), the total charge passed in photoetching was determined to be equivalent to a 1 μm thickness of SnS_2. The photocurrent incident photon to current efficiency was calculated as the ratio of the photocurrent to the photon flux at each wavelength. These experiments demonstrate that, in this case, the sensitized photocurrent yield increases by an order of magnitude after PEC etching.

Increasing the amount of charge passed when photoetching SnS_2 in HCl or NaOH yielded greater dye sensitized and band gap photoresponses for SnS_2 electrodes. Figure 4.3 shows the IPCE spectra for MB^+ before and after photoetching SnS_2 (8.0×10^{16} Cl^- atoms/cm^3) with a xenon lamp in two different solutions, 1 M HCl (~ 2 C/cm^2 of charge passed in 7 minutes of illumination) and 5 M NaOH (~14 C/cm^2 of charge passed in 20 minutes of illumination). The resulting photoaction spectra in Figure 4.3, show the dye sensitized photocurrent onsets at 550 nm and reaches a maximum yield at about 680 nm. The band gap transition IPCE for SnS_2 increased roughly a factor of three after HCl photoetching and a factor of five after NaOH photoetching. The dye sensitized IPCE for SnS_2 increased about twenty fold after HCl photoetching and thirty fold

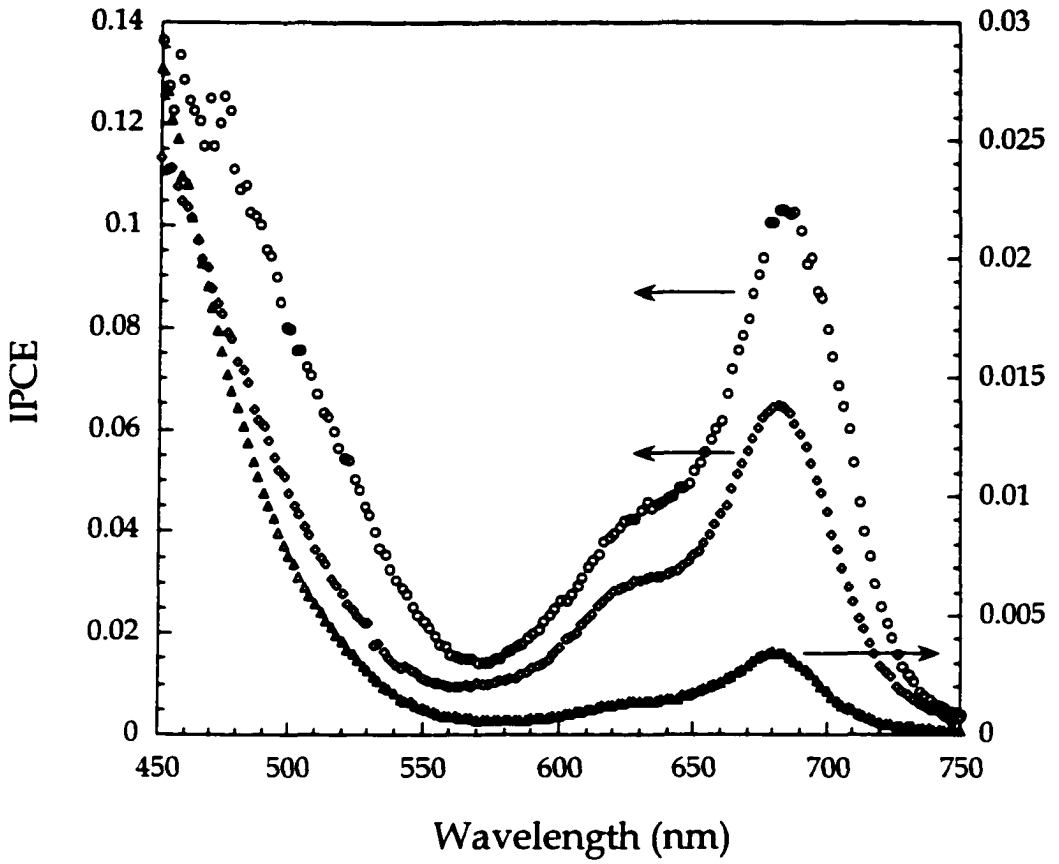

Figure 4.3. Photoaction spectra before and after PEC etching for SnS_2 ($8.0x10^{16}$ Cl^- atoms/cm^3). Circles represents the IPCE after photoetching in 5 M NaOH, diamonds represent the IPCE after photoetching in 1 M HCl and triangles represent the IPCE before photoetching. The 30 mM H_2Q/electrolyte solution contained 10 μM MB^+ and the electrode potential was biased 0.7 V vs Ag/AgCl. The SnS_2 surface photoetched in 1 M HCl was biased 1 V vs SCE with approximately 2 C/cm^2 of total charge passed. While the SnS_2 surface photoetched in 5 M NaOH was biased 0.7 V vs SCE with approximately 14 C/cm^2 passed.

for NaOH photoetching. The high MB^+ IPCE of 14%, for the NaOH photoetched electrode was measured near the electrode edge while the center of the electrode yielded a MB^+ IPCE of 8.4%. The SEM of the surface of the SnS_2 electrode on which the high IPCE was measured is shown in Figure 4.1c. The greater extent of photoetching (31 C/cm^2 in 5 M NaOH) for the surface displayed in Figure 4.1d resulted in a lower MB^+ IPCE at both the electrode edge (7.2%) and center (1.7%). The difference in the MB^+ IPCE at the edge vs the center of the SnS_2 crystal may be due to a greater degree of photoetching where the crystal has been strained and damaged by cutting. Sensitization yields on SnS_2 surfaces chemically etched in *aqua regia* showed no enhancements over unetched surfaces and, thus, further experiments with this etchant were discontinued.

In order to optimize the dye sensitized photocurrent enhancement, the relationship between the magnitude of sensitized photocurrent and the extent of photoetching in both HCl and NaOH was studied. Two dyes, MB^+ and CV^+, were used to monitor the enhanced dye sensitized IPCE. The PEC etching for this study was carried out with the 488 nm illumination from an Ar^+ laser. The small illumination area allowed several photoetching experiments to be carried out on the same cleaved surface. The laser was directed, sequentially, onto isolated areas of the electrode for different periods of time. This allowed the sensitized photocurrent response to be analyzed as a function of the extent of photoetching on a freshly cleaved, single SnS_2 (8.0×10^{16} Cl^- atoms/cm^3) cleavage surface. Note that the photoetching time is not necessarily linearly proportional

to the extent of PEC etching when using the arc lamp because both the dark current and the photocurrent can change throughout the photoetching process. This is not the case when photoetching with the Ar^+ laser because the photocurrent generated from photoetching such a small area of the electrode was low in comparison to the dark current, therefore the time instead of the integrated photocurrent was used as an indicator of the extent of PEC etching. After photoetching in HCl with the electrode biased 0.7 V vs SCE, the electrode was rinsed and transferred into an electrolyte solution containing CV^+ and H_2Q. The CV^+ sensitized photocurrent was then monitored at 632.8 nm using a He-Ne laser that has a spot size comparable to the Ar^+ laser. The NaOH photoetched SnS_2 electrode was rinsed and transferred to a new electrolyte solution containing MB^+ and H_2Q. Then the MB^+ sensitized photocurrent was monitored with 680 nm light from a tungsten-halogen lamp selected through a monochromator as described in the experimental section in Chapter 3. The results of these measurements are shown in Figure 4.4a for HCl and CV^+ and 4.4b for NaOH and MB^+. The sensitized photocurrent in Figures 4.4a and b reach a maximum around 120 seconds of photoetching. The CV^+ sensitized photocurrent decreases more slowly than the MB^+ sensitized photocurrent. The MB^+ sensitized photocurrent maximum at 120 seconds corresponds to an IPCE of approximately 4%.

The effect of the extent of photoetching in NaOH and the resulting dye sensitized quantum efficiency was further studied by altering the light exposure

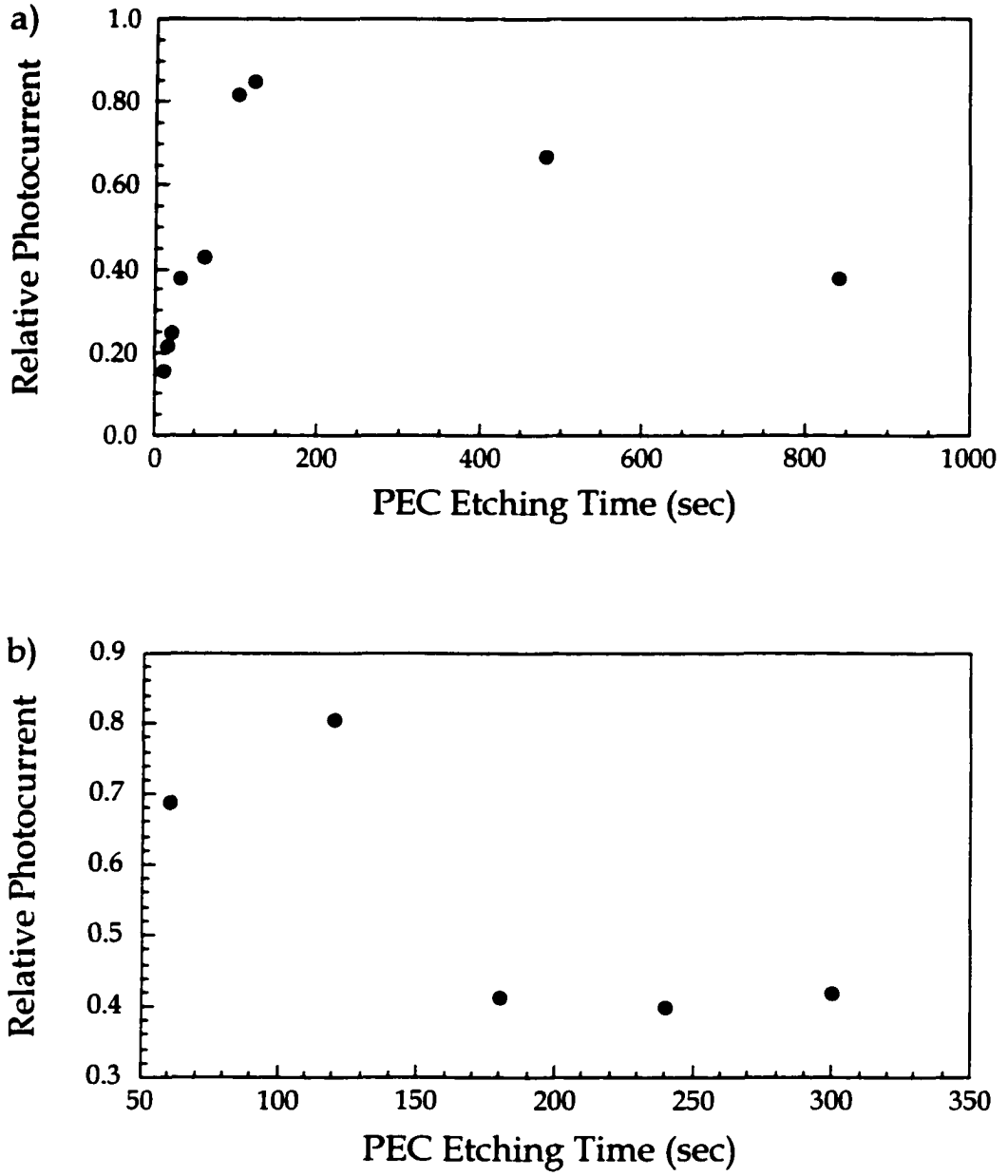

Figure 4.4. Relative photocurrent as a function of PEC etching time for SnS_2, biased 0.7 V vs Ag/AgCl, with dye sensitized photocurrent measured in a 30 mM H_2Q electrolyte solution for a) CV^+ (10 μM), probed with a He-Ne laser and b) MB^+ (10 μM) measured with 680 nm light from a tungsten-halogen lamp. Photoetching was carried out on SnS_2 electrodes (8.0×10^{16} Cl-atoms/cm^3) with 488 nm illumination from an Ar^+ laser at a) 2 mW in 1 M HCl with SnS_2 biased 1 V vs SCE and b) 0.85 mW in 5 M NaOH with SnS_2 biased 0.7 V vs SCE.

on the surface from a xenon lamp using a step wedge neutral density filter as an alternative to the laser spot technique. Similar to the Ar^+ laser photoetching experiments, there appeared to be an optimum extent of photoetching required to maximize the dye sensitized IPCE as shown in Figure 4.5a. A maximum band gap IPCE was also observed for these experiments as shown in Figure 4.5b. In contrast to the Ar^+ laser experiments, the actual extent of charge passed per cm^2 for each step wedge was not determined due to the nature of the experiment and thus, only the total charge was measured. Comparing Figure 4.5a and b reveals that the photoresponse for both the band gap and the dye sensitized IPCE reach a maximum at a relative exposure of approximately 0.2 to 0.4 for the SnS_2 electrode ($8.0x10^{16}$ Cl^- atoms/cm^3) photoetched with 7.11 C/cm^2 and 9.13 C/cm^2 of total charge passed. Figure 4.5b shows that the band gap IPCE increased by a factor of 3 and 5 for the SnS_2 electrodes photoetched with 7.11 C/cm^2 and 9.13 C/cm^2, respectively. Figure 4.5a shows that the dye sensitized IPCE increased by a factor of 5.5 and 15 for the SnS_2 electrodes photoetched with 7.11 C/cm^2 and 9.13 C/cm^2, respectively. Figure 4.6 shows the ratio of the dye sensitized IPCE to the band gap IPCE for both photoetched SnS_2 surfaces showing that the ratio also reaches a maximum between a relative exposure of 0.2 to 0.4.

In an effort to further analyze the relationship between photoetching and the corresponding IPCE increases, a series of photoetching studies were carried out where the total charge passed was less than 1 mC/cm^2. Because the anodic

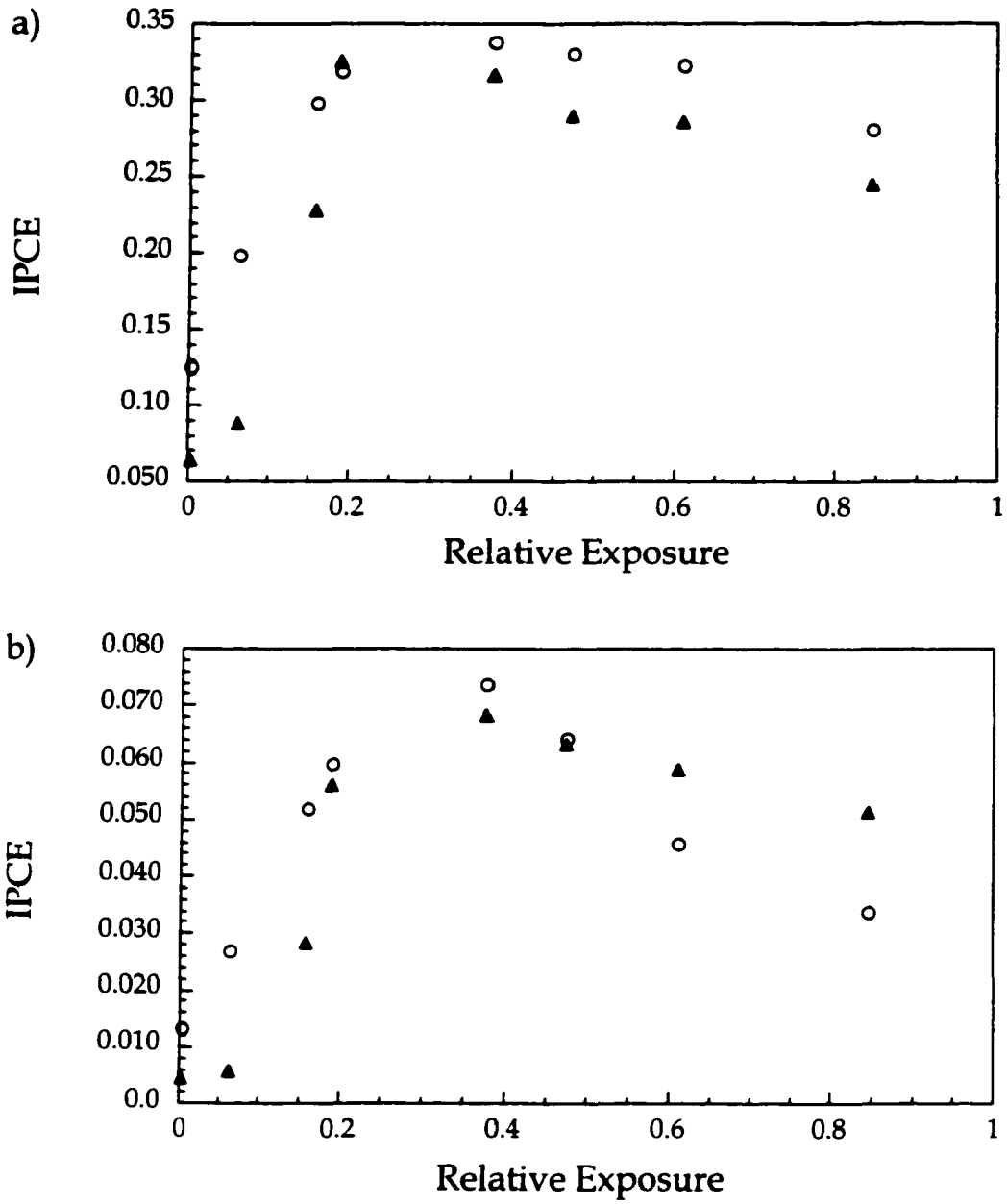

Figure 4.5. IPCE as a function of exposure (charge passed) for photoetched SnS_2 ($8.0x10^{16}$ Cl^- atoms/cm^3) sensitized with MB^+ in a regenerator/electrolyte solution, biased 0.7 V vs Ag/AgCl. SnS_2, biased at 0.7 V vs SCE, was photoetched in 5 M NaOH with a xenon lamp passing through a step wedge neutral density filter. The total charge passed was 7.11 C/cm^2 (open circles) and 9.13 C/cm^2 (solid triangles). a) Dye sensitized signal was monitored at 680 nm and b) the indirect band gap transition of SnS_2 was monitored at 450 nm.

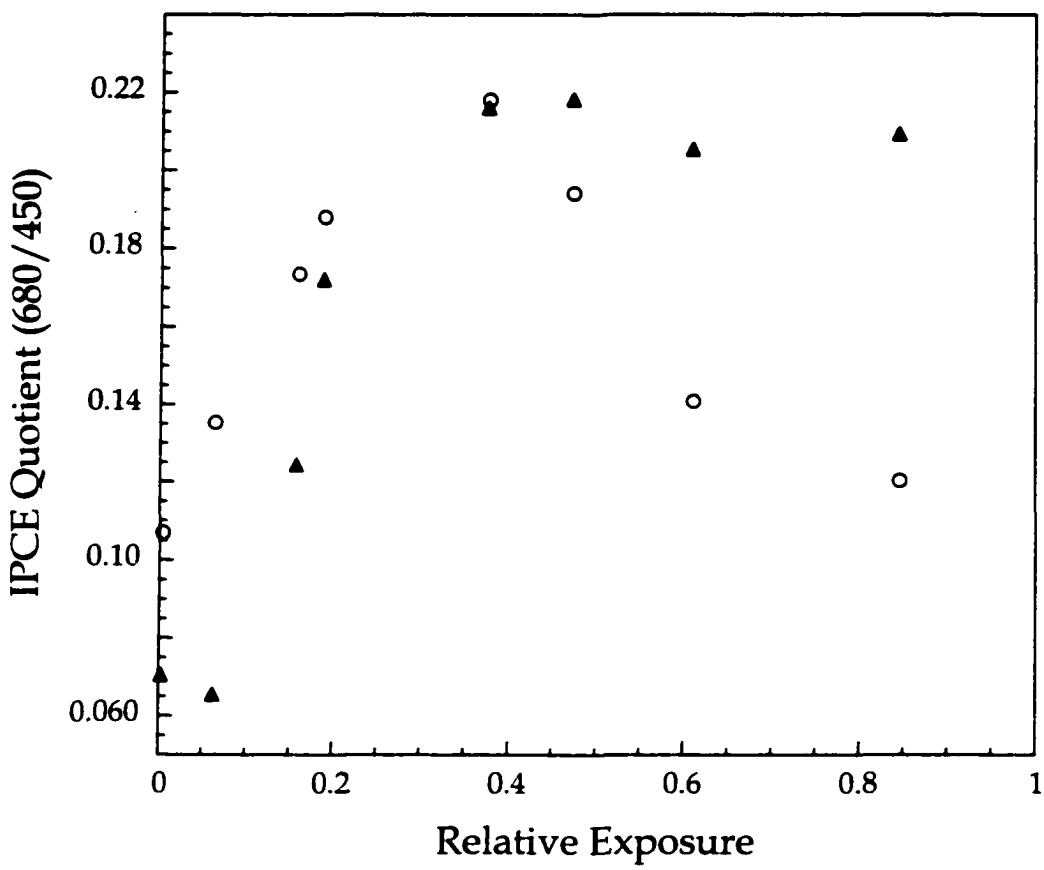

Figure 4.6 The ratio of the MB^+ IPCE (680 nm) to the band gap IPCE (450 nm), from Figures 4.5a and b, at various relative photoetching exposures. Open circles represent the ratio of the IPCE of 680 nm to 450 nm for SnS_2 photoetched passing a total charge of 7.11 C/cm^2 and solid triangles represent the 680/450 ratio with 9.13 C/cm^2 of total charge passed.

photodecomposition reaction in a basic solution was predicted to involve 8-12 h^+ and a layer of SnS_2 is known to be 5.89 Å thick, the amount of charge per unit area required to remove one monolayer of SnS_2 was determined to be approximately 1.41 mC/cm^2. The IPCEs associated with MB^+, CV^+ and AZB^+ at their absorption maxima and the IPCE associated with SnS_2 at its band gap excitation wavelength (460nm) are reported in Figure 4.7a, Figure 4.7b and Figure 4.8a for SnS_2 electrodes with 0 - 3 monolayer equivalents of SnS_2 removed. The SnS_2 electrodes were doped with $4.2x10^{17}$ Cl^- atoms/cm^3 and sensitized with MB^+ in Figure 4.7a, doped with $3.7x10^{17}$ Cl^- atoms/cm^3 and sensitized with CV^+ in Figure 4.7b and doped with $7.3x10^{16}$ Cl^- atoms/cm^3 and sensitized with AZB^+, Figure 4.8a. The electrodes were photoetched with a xenon lamp in 5 M NaOH. These plots show an initial rise in the IPCE for both the band gap and dye sensitized responses. There was an increase in the dye sensitized IPCE for MB^+ from $1.8x10^{-3}$ to $1.5x10^{-2}$ (eight fold), for CV^+ from $1.9x10^{-4}$ to $4.5x10^{-4}$ (two fold) and for AZB^+ from $3.1x10^{-4}$ to $1.0x10^{-3}$ (three fold). The band gap IPCE increased from 0.029 to 0.054 (two fold) for the photoetched SnS_2 in Figure 4.7a and less than two fold for the photoetched SnS_2 in Figures 4.7b and 4.8a.

Photoetching of additional monolayers was carried out on SnS_2 ($7.3x10^{16}$ Cl^- atoms/cm^3) in NaOH. The resulting IPCE associated with the AZB^+ sensitization (at 680 nm) and the IPCE associated with band gap excitation (at 460 nm) are shown in Figure 4.8b. When the extent of photoetching increased past the equivalent of more than one monolayer, as shown in Figure 4.8a, the dye

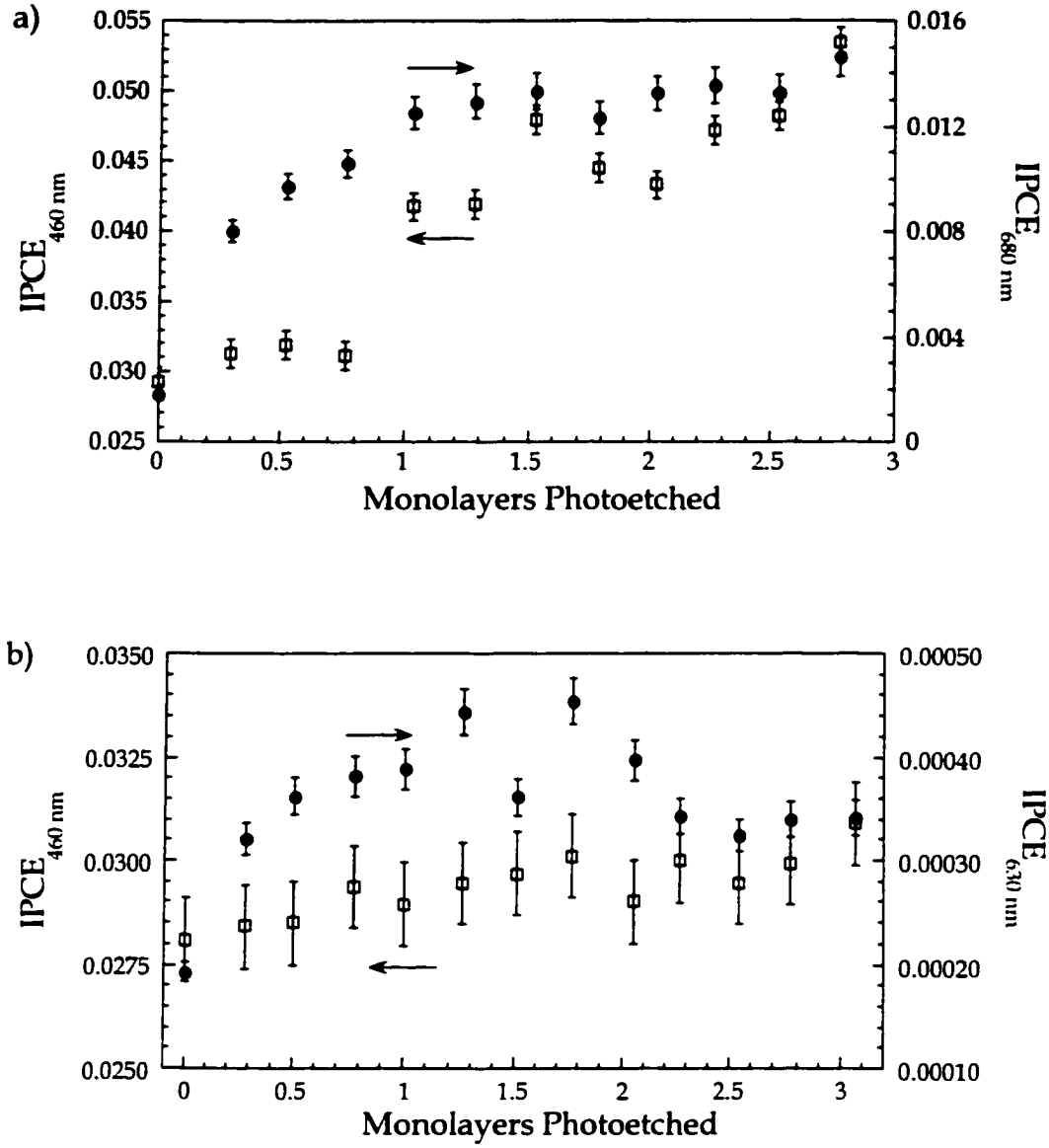

Figure 4.7. Band gap and dye sensitized IPCEs as a function of the number of SnS_2 monolayer equivalents photoetched for two different samples. Photoaction spectra were taken with the electrodes biased 0.7 V vs Ag/AgCl in a solution of 30 mM H_2Q/electrolyte and 7μM dye where a) MB^+ and b) CV^+. The SnS_2 electrodes were photoetched in 5 M NaOH with a xenon lamp and biased 0.7 V vs SCE. One monolayer equivalent represents 1.41 mC/cm^2. The SnS_2 carrier concentrations were a) 4.2×10^{17} Cl^- atoms/cm^3 and b) 3.7×10^{17} Cl^- atoms/cm^3.

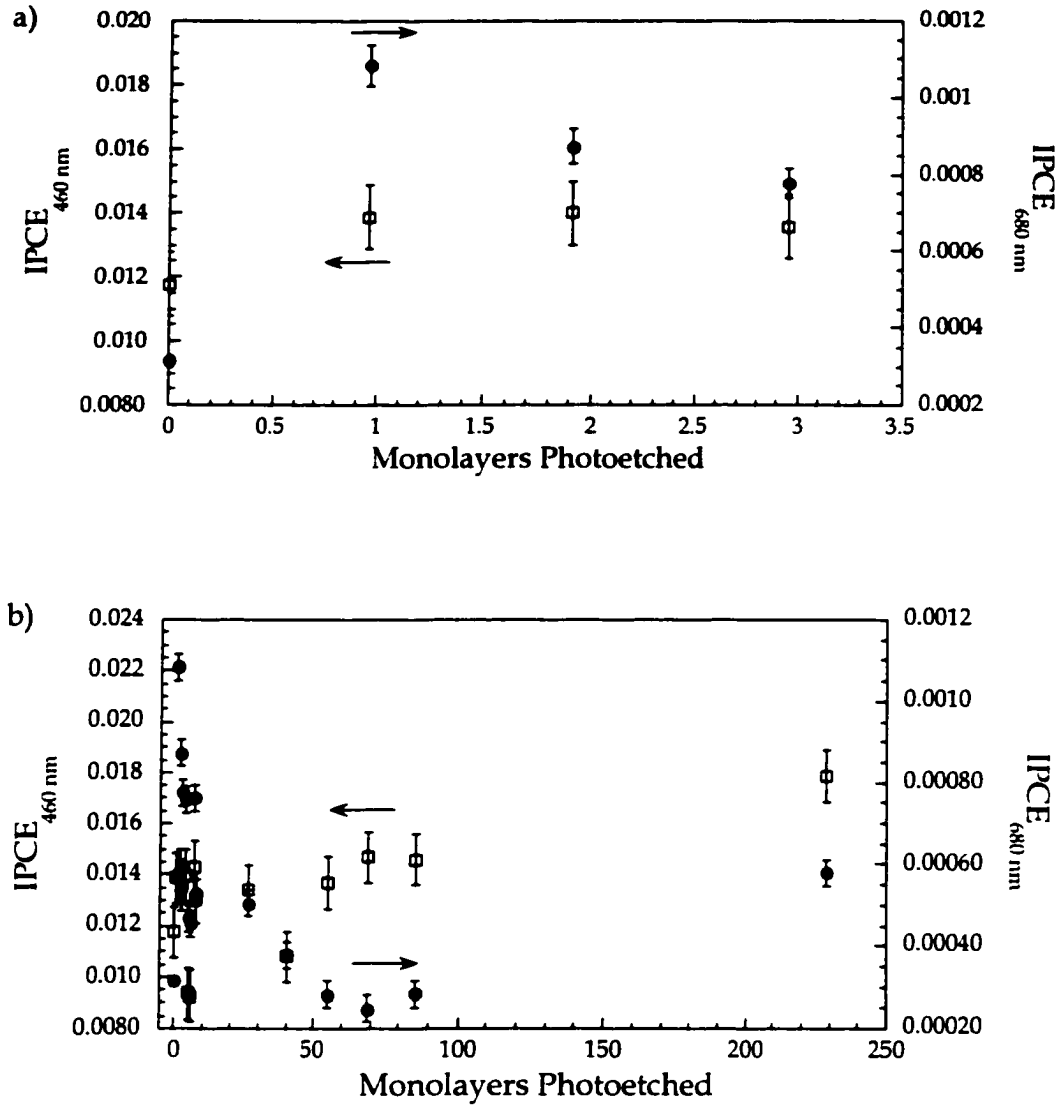

Figure 4.8 Dye sensitized and band gap IPCE as a function of SnS_2 ($7.3x10^{16}$ Cl^- atoms/cm^3) monolayer equivalents photoetched. The plot in (a) shows the first three monolayer equivalents removed for the electrode in (b). Photoaction spectra of the SnS_2 electrodes were taken in a solution of 7μM AZB^+ and 30 mM H_2Q/electrolyte with the electrodes biased 0.7 V vs Ag/AgCl. The SnS_2 electrodes were photoetched with a xenon lamp in 5 M NaOH and biased 0.7 V vs SCE. One monolayer equivalent represents 1.41 mC/cm^2.

sensitized IPCE decreased until reaching the equivalent of 70 monolayers, after which, there was an increase in the dye sensitized IPCE. This was in contrast to the band gap IPCE, which continued to increase with further photoetching.

An Atomic Force Microscope (AFM) was used to image the surface of SnS_2 ($5.7x10^{16}$ Se atoms/cm^3) freshly cleaved, after immersion in 5 M NaOH (5 min) and after photoetching a single monolayer (1.51 C/cm^2). The SnS_2 surface was photoetched in 5 M NaOH with a xenon lamp and the electrode biased 0.7 V vs SCE. The SnS_2 surface is shown freshly cleaved in Figure 4.9, after immersion in NaOH in Figure 4.10 and after photoetching in Figure 4.11. These Figures show that the photoetched surface has the greatest surface roughness. Because a layer of SnS_2 was known to be 5.89 Å and the doping density was determined through Mott-Schottky and Hall measurements, there were approximately 250 dopant atoms in the surface layer of the scanned area ($1.35x10^{-9}$ cm^2) in Figure 4.11b. Counting the number of etch pits that are represented by dark spots on the surface in Figure 4.11b, revealed there was a loose correlation between the surface concentration (number of sites per surface area) of PEC etch pits and the surface concentration of dopant atoms on the SnS_2 surface.

The relationship between the carrier concentration, the extent of photoetching and the dye sensitized IPCE was also studied. Tin disulfide electrodes with three different chloride dopant concentrations; $3.2x10^{16}$ cm^{-3}, $7.3x10^{16}$ cm^{-3} and $3.7x10^{17}$ cm^{-3}, were photoetched in 5 M NaOH with a xenon lamp with the semiconductor electrodes biased at 0.7 V vs SCE. The total charge

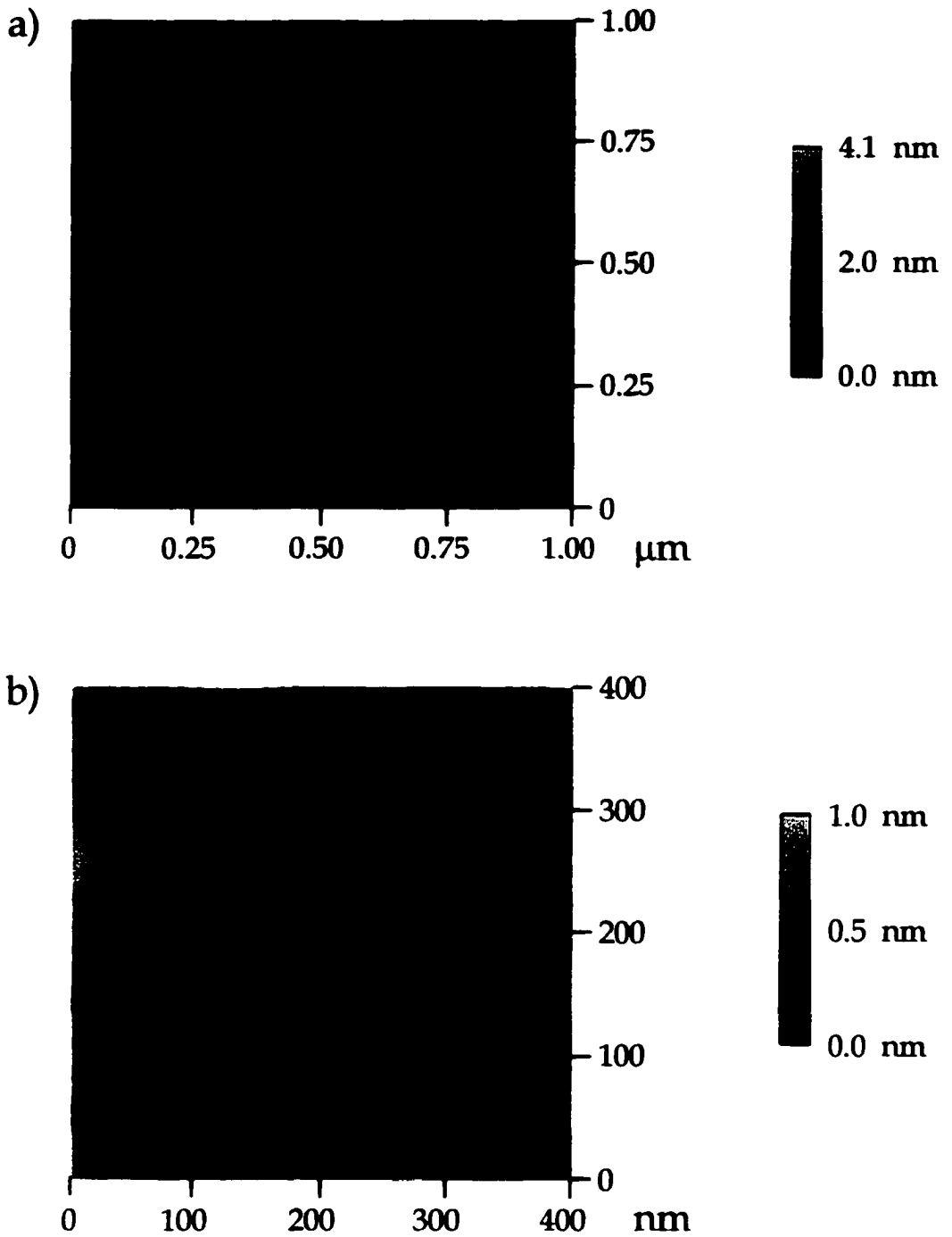

Figure 4.9. Images of an unetched SnS_2 ($5.7x10^{16}$ Se atoms/cm^3) surface taken with constant height Tapping AFM.

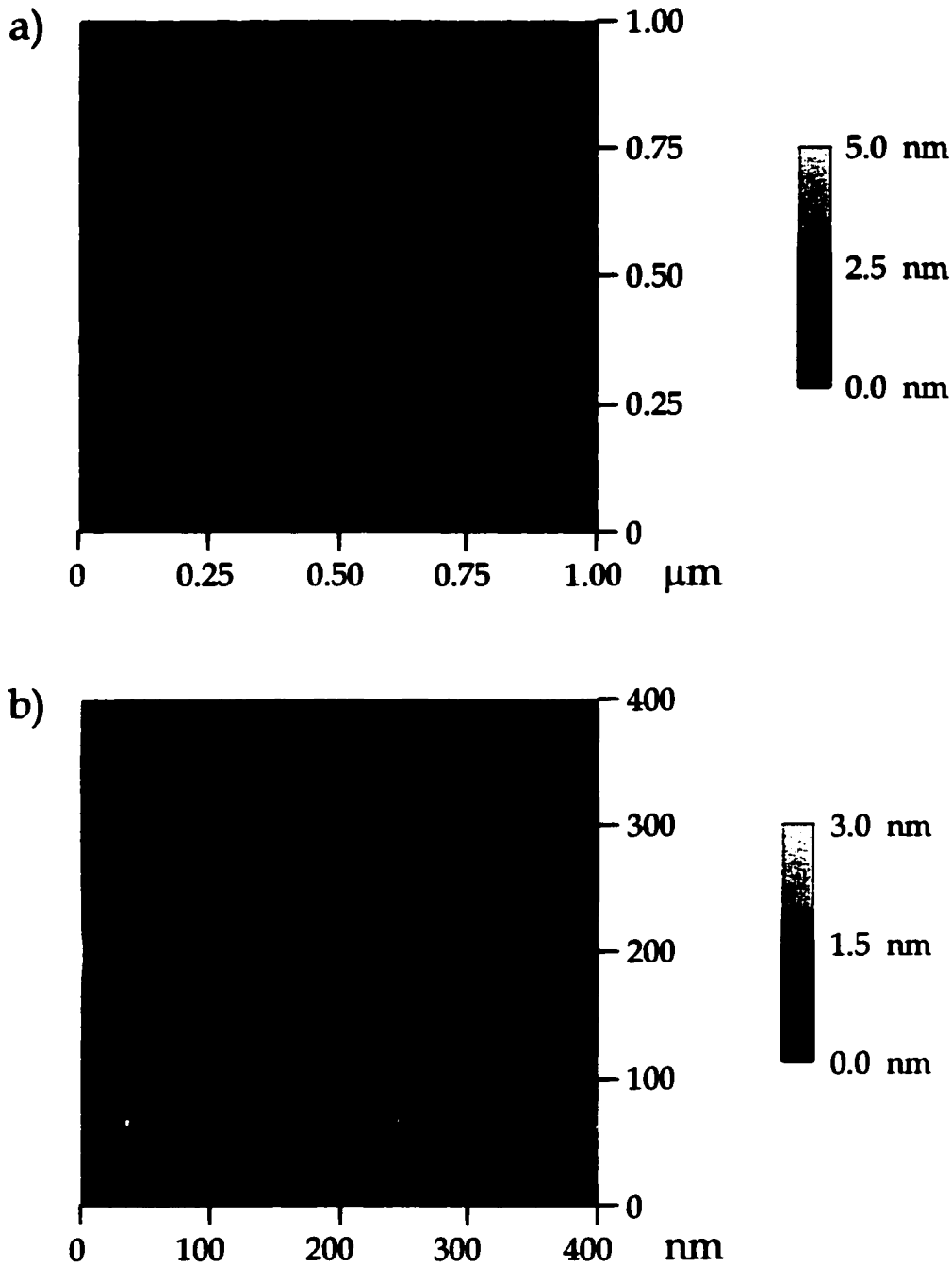

Figure 4.10. Constant height Tapping AFM images of SnS_2 (5.7×10^{16} Se atoms/cm^3) immersed in 5 M NaOH for 5 minutes and then rinsed with water.

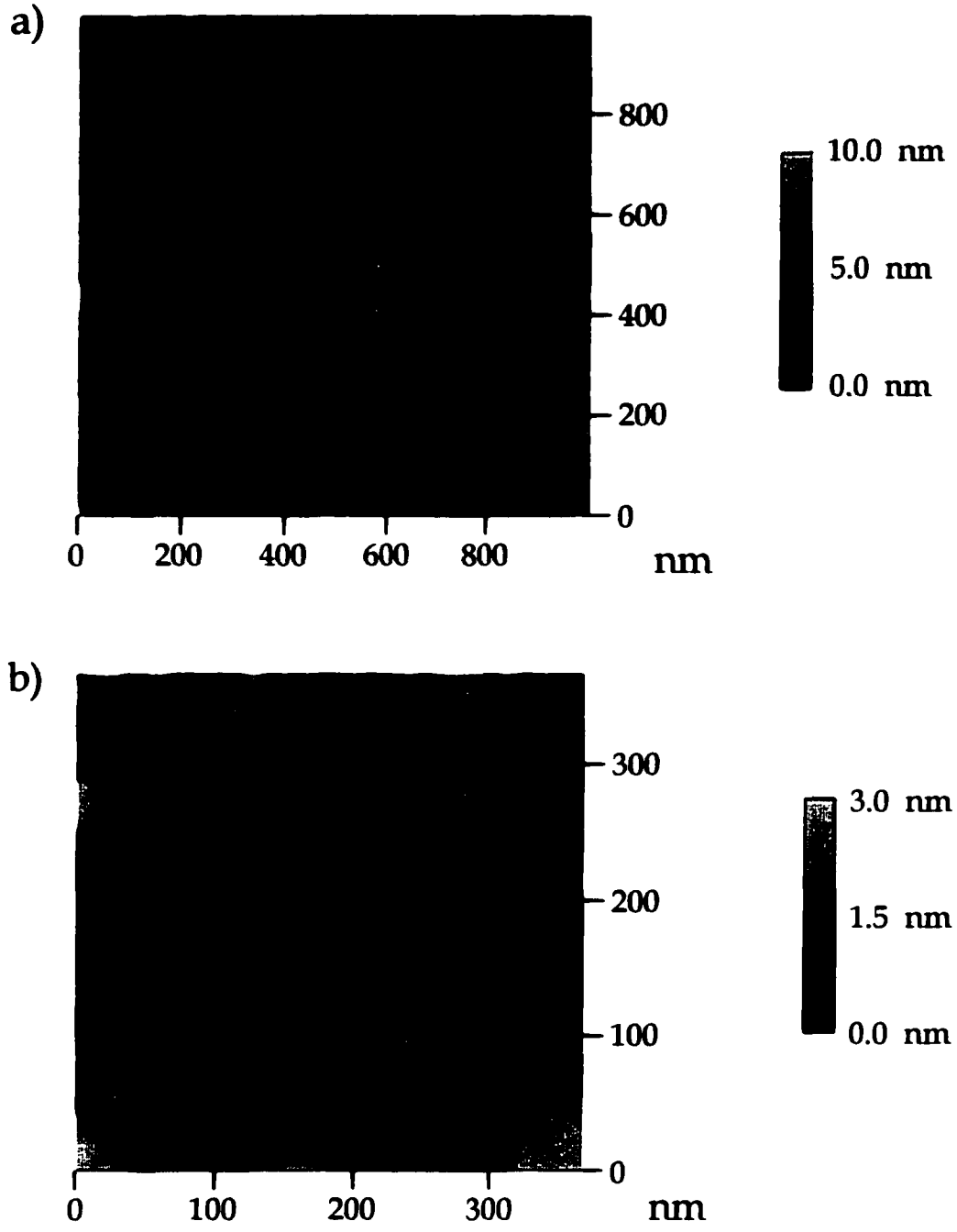

Figure 4.11 Constant height Tapping AFM images of photoetched SnS_2 ($5.7x10^{16}$ Se atoms/cm^3) with the equivalent charge passed to remove one monolayer. The SnS_2 surface was photoetched in 5 M NaOH with a xenon lamp and 1.51 mC/cm^2 of charge was passed with the electrode biased 0.7 V vs SCE. The area scanned was $1.35x10^{-9}$ cm^2.

passed was varied from 0.01 C/cm^2 to 1.5 C/cm^2 (7 to 1068 monolayer equivalents) and the resulting dye sensitized IPCE for MB^+ was measured; the results are shown in Figure 4.12. The dye sensitized IPCE increased as the amount of total charge passed in photoetching increased for the SnS_2 electrodes of all carrier concentrations. Tin disulfide with a carrier concentration of $7.3x10^{16}$ cm^{-3} showed the largest dye sensitized IPCE increase with photoetching, which was about a sixteen fold increase. The smallest dye sensitized IPCE was observed for SnS_2 with a carrier concentration of $3.2x10^{16}$ cm^{-3}. There appears to be a distinct correlation between the dye sensitized IPCE and extent of photoetching for a particular SnS_2 carrier concentration.

Adsorption Isotherms for CV^+ and MB^+. Isotherms for the adsorption of two dyes, MB^+ and CV^+, on photoetched and unetched SnS_2 surfaces were measured by consecutive additions of a dye/methanol stock solution to the background electrolyte containing 10 mM hydroquinone. Again, as discussed in the previous chapter, the sensitization yield was assumed to be proportional to the dye coverage. The sensitized photocurrent was monitored at 680 nm for MB^+ and 630 nm for CV^+ after addition of each aliquot of dye. An equilibration time of 5 minutes was allotted for the unetched SnS_2 samples as longer equilibrium times resulted in insignificant increases in the photocurrent. The equilibration time for MB^+ adsorption on photoetched SnS_2 surfaces depended on the surface morphology, as controlled by the PEC etching conditions. In some instances MB^+ took up to 2 hours to equilibrate on photoetched SnS_2 surfaces. However,

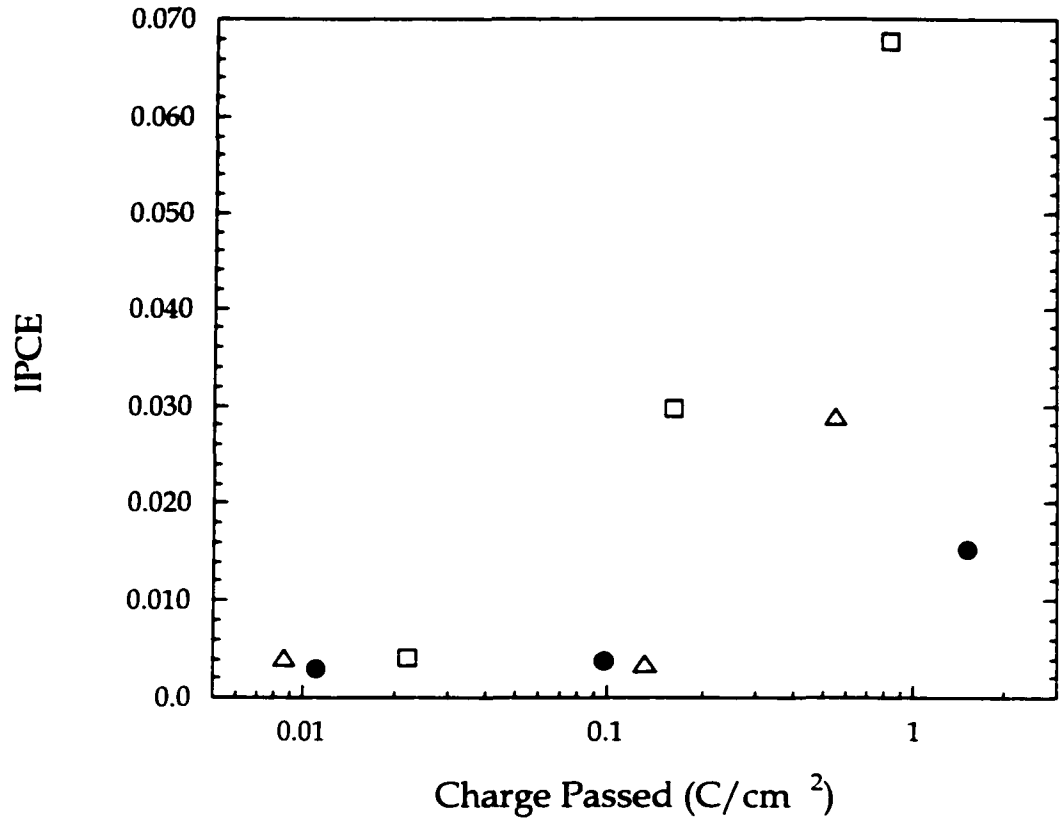

Figure 4.12. The IPCE of MB^+ as a function of the anodic charge passed for photoetched SnS_2 electrodes with three different carrier concentrations; solid circles represent $3.2x10^{16}$ Cl^- atoms/cm^3, squares represent $7.3x10^{16}$ Cl^- atoms/cm^3 and triangles represent $3.7x10^{17}$ Cl^- atoms/cm^3. Photocurrent measurements were carried out in 7 μM MB^+ in a H_2Q/electrolyte solution with the SnS_2 electrodes biased 0.7 V vs Ag/AgCl. SnS_2 electrodes were photoetched in 5 M NaOH with a xenon lamp and biased 0.7 V vs SCE.

only small signal increases were observed after 10 minutes of equilibration for the PEC etched SnS_2 in this experiment. Because the adsorption kinetics were faster for CV^+ than MB^+, the adsorption of CV^+ was monitored after 5 minutes of stirring for each dye aliquot and after 10 minutes for MB^+ on photoetched SnS_2. The hydroquinone concentration was increased to 30 mM for the photoetched surfaces because the photocurrent as a function of hydroquinone concentration did not increase above this concentration as will be discussed below. For unetched surfaces this was unnecessary, because the photocurrent signal was unaffected by the same increase in hydroquinone concentration. The results of the incident photon to current efficiency as a function of dye solution concentration are shown in Figure 4.13. The results for CV^+ on unetched surfaces were not shown because the IPCE signal was difficult to detect, as discussed in the previous chapter. Figure 4.13 shows that the adsorption of MB^+ was stronger than CV^+ on photoetched surfaces.

Stability of the Sensitized Photocurrent. The time dependence of the IPCE for MB^+ sensitization on a photoetched SnS_2 surface (4.3 C/cm^2) is shown in Figure 4.14 for various light intensities (light intensity of the laser was varied using neutral density filters as the laser used in this study was not sophisticated enough to allow for direct current control). The IPCE at the absorption maximum (680 nm) was initially greater than 4% but the efficiency decreased with time. Figure 4.14 shows the decay of the IPCE signal with time, which occurred even in the presence of regenerator (30 mM H_2Q). It required about

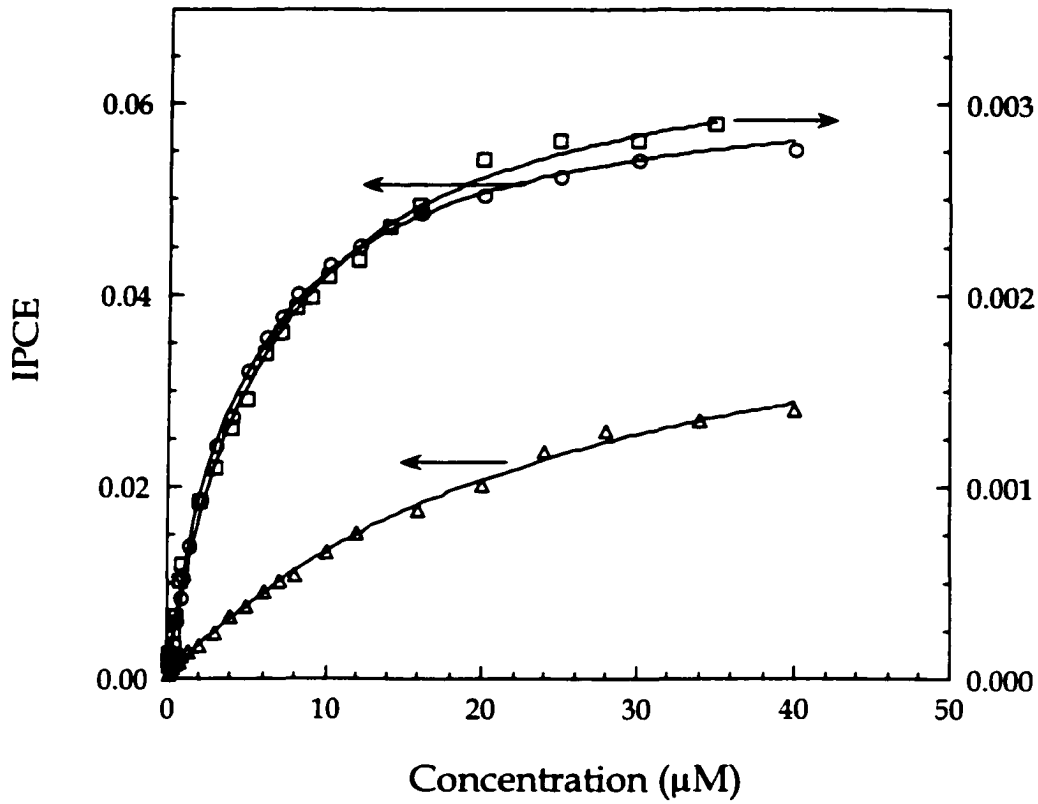

Figure 4.13. Adsorption isotherms of MB^+ and CV^+ sensitized IPCE on SnS_2 ($8.0x10^{16}$ Cl^- atoms/cm^3) as a function of dye solution concentration. The dye photoresponse was measured with the monochromator set at 680 nm for MB^+ and 632 nm for CV^+. The solution concentration of hydroquinone was 30 mM for the photoetched SnS_2 and 10 mM for the unetched SnS_2. The electrode potential was 0.7 V vs Ag/AgCl. Squares represent MB^+ on the unetched SnS_2 surface, circles are MB^+ on the photoetched SnS_2 surface and triangles are CV^+ on the photoetched SnS_2 surface. The solid lines are the theoretical fits using a Langmuir isotherm. Photoetching was carried out in 1 M HCl with a xenon lamp and 2.28 C/cm^2 of total charge passed with the electrode biased 1 V vs SCE.

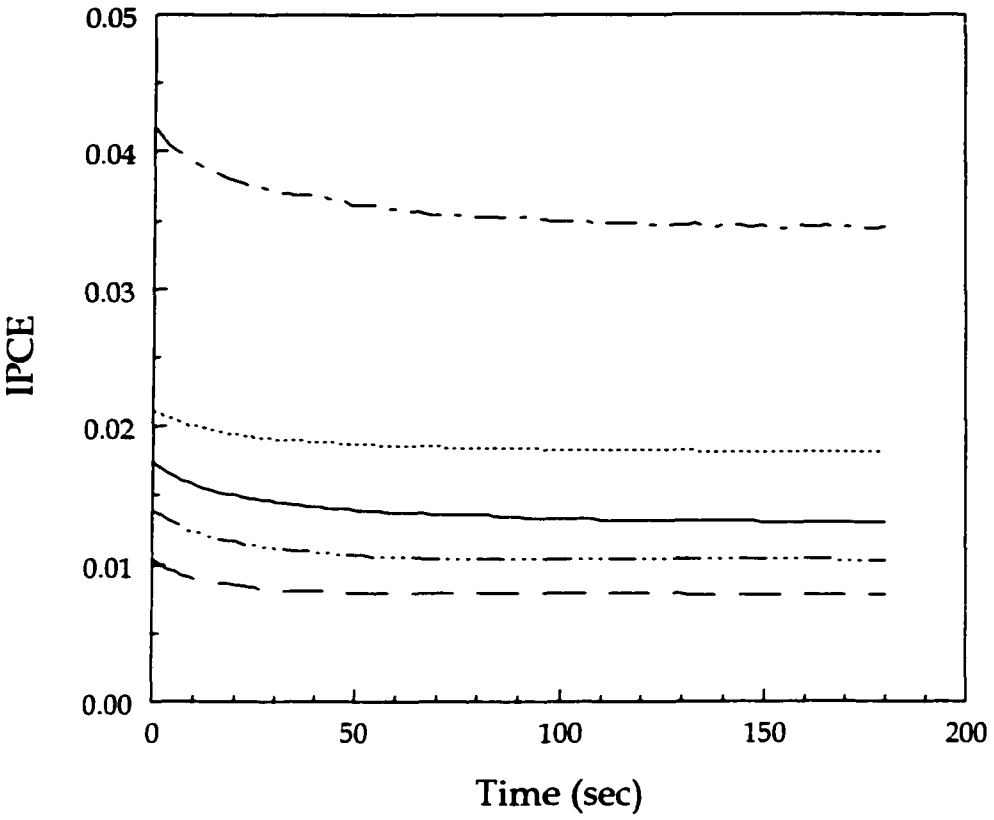

Figure 4.14. The time dependence of MB^+ sensitized IPCE on a PEC etched SnS_2 electrode (8.0×10^{17} Cl^- atoms/cm^3). The photocurrent was measured in an electrolyte solution containing 10 μM MB^+ and 30 mM hydroquinone with a 689 nm diode laser (18 mW). Various neutral density filters were used to modify the light intensity; 24 μW (— -), 185 μW (·····), 2 mW (—), 6.3 mW (— ···) and 18 mW (— —). The electrode potential for the IPCE measurements was 0.7 V vs Ag/AgCl. The SnS_2 electrode was photoetched in 1 M HCl with a xenon lamp and biased 1 V vs SCE with 4.3 C/cm^2 of total charge passed.

60 seconds to establish a "photostationary state" for the IPCE measurements. Unetched surfaces did not show a decay in the sensitized photocurrent on the same time scale. This decay suggested that continued illumination caused a decrease in the number of adsorbed photoactive dye molecules by either desorption or photoxidation without regeneration by the reducing agent.

The IPCE for the photostationary state also decreased with increasing light intensities. Note that due to the time resolution of these experiments (measurements were recorded within 500 ms with the naked eye) and the rapid decay initially, it was not possible to obtain an accurate reading at zero seconds. Although the initial IPCEs appear smaller at the higher light intensities in Figure 4.14, the true initial values were similar. Stirring the electrolyte solution while measuring the photocurrent slowed the decay time and increased the photocurrent signal of the photostationary state by about 40%. This suggested that at least some part of the decay was controlled by the diffusion of regenerator into the porous structures on the surface. Less deeply photoetched surfaces exhibited a smaller decay of the dye sensitized photocurrent at higher light intensities that was consistent with the mass transport of regenerator being responsible for some portion of the decay with time.

DISCUSSION

Dye Adsorption on Photoetched Surfaces. The photoaction spectra shown in Figure 4.2 revealed that there was no detectable shift in the MB^+ sensitization

maximum after photoetching. There was also no observable shift in the sensitization maximum as the dye surface coverage increased during the adsorption isotherm studies. The lack of an appreciable shift (< 5 nm) before and after etching indicates that the majority of adsorbed dye molecules occupy similar adsorption sites. If this is true, the assumption that the incident photon to current efficiency was linearly proportional to the surface dye concentration was validated and these curves can be viewed as dye adsorption isotherms when no aggregates are present. Note that a minority of special dye adsorption sites will not influence the isotherm. Because the quantum yield per absorbed photon was assumed to be unity, the adsorption isotherm curves (Figure 4.13) were fitted to the following Langmuir type isotherm derived in the previous chapter:

$$IPCE = C_m KsC/(KC + 1), \qquad (4.3)$$

in which K was the adsorption coefficient (μM^{-1}), s was the known molecular light absorption cross section for the dyes at a given wavelength (the IPCE was measured at 630 nm for CV^+ and 680 nm for MB^+) in cm^2/molecule, C was the solution dye concentration (μM), and C_m was the surface dye concentration at monolayer coverage in molecules/cm^2. Note that the area (C_m) refers to the geometric area and that a larger value of C_m for the photoetched surfaces implies a surface roughness factor instead of dye aggregation or dense packing. The fitted results are plotted as the solid line in Figure 4.13 for each of the three cases; MB^+ on unetched surface, MB^+ on photoetched surface, and CV^+ on photoetched surface.

The "isotherms" in Figure 4.13 appear to conform to Langmuir type adsorption. The Langmuir isotherm model assumes that the heat of adsorption, ΔH_{ads}, is independent of the surface coverage. The Langmuir isotherm also presumes that MB^+ and CV^+ both adsorb non-preferentially onto equivalent surface adsorption sites. Fits to Langmuir isotherms, however, do not guarantee that the dyes do not interact or are not adsorbing as islands instead of onto random equivalent sites.[20] The fitting parameters for the dye adsorption isotherms, summarized in Table 4.1, show the adsorption coefficient (K) is lower for CV^+ on photoetched SnS_2 surfaces than for MB^+ on either etched or unetched surfaces, which agrees with the observations from Chapter 3. The adsorption coefficient, which is physically a measure of the binding strength between the adsorbate and the surface, is also slightly larger for MB^+ on photoetched surfaces compared to unetched surfaces. When the surface was photoetched, CV^+ adsorbed onto the surface with a surface monolayer concentration, C_m, of 3.91×10^{14} molecules/cm^2. The monolayer surface concentration for MB^+ on photoetched surfaces was 5.19×10^{14} molecules/cm^2, a twenty fold increase over unetched surfaces. This can be explained as the result of a twenty fold increase in the surface area after photoetching. Comparing the monolayer surface dye concentration for CV^+ and MB^+ showed there was approximately 25% more MB^+ adsorbed on the same photoetched surface. This is not surprising given the larger area a CV^+ molecule will occupy on the surface due to its larger ring structure.

Table 4.1. Adsorption Isotherm Parameters for dyes adsorbed on unetched and etched SnS_2.

	Methylene Blue/ Unetched	Methylene Blue/ Etched	Cresyl Violet/ Etched
K (μM^{-1})	0.163 ± 0.008*	0.198 ± 0.007	0.0399 ± 0.0022
C_m (Molecules/cm^2)	(2.84 ± 0.04) E+13	(5.19 ± 0.06) E+14	(3.91 ± 0.11) E+14
C_mK (Å)	(7.69 ± 0.49) E+5	(1.70 ± 0.13) E+7	(2.58 ± 0.21) E+6
ΔH (Kcal/mole)	- 7.04 ± 0.04	- 8.86 ± 0.04	- 7.75 ± 0.05
$IPCE_{max}$	0.341 %	6.23 %	4.69 %
Area/Molecule	352 $Å^2$		

* The error listed for each parameter is the fitting uncertainty.

Mechanism of Enhanced Photocurrent. Photoelectrochemical etching of SnS_2 surfaces with over 1 C/cm^2 of total charge passed yielded an increase in the dye sensitized IPCE for MB^+ and CV^+. The MB^+ IPCE on SnS_2 increased twenty fold, from 0.35% to 7%, for MB^+ after photoelectrochemical etching in 1 M HCl with 2 C/cm^2 (Figure 4.3). The MB^+ IPCE improvement was even greater for surfaces photoetched in 5 M NaOH with a maximum of over 10% when 14 C/cm^2 were passed (Figure 4.3). CV^+ sensitization yields improved from less than 0.01% to 4.5% after photoetching in 1 M HCl (1 C/cm^2), an increase of over four hundred and fifty fold (Figure 4.2). There was also an optimal extent of photoetching where the dye sensitized IPCE reached a maximum as determined with both the laser and step wedge exposure mask experiments. Studies with the step wedge exposure mask also showed that the ratio of the dye sensitized IPCE to the band gap IPCE on the photoetched SnS_2 reached a maximum at the same relative exposure as both the dye and band gap IPCEs. This indicated that the increased IPCE for both band gap excitation and dye sensitization were probably associated with the same phenomenon.

Increases in the IPCE for band gap radiation were also observed after photoetching. Band gap photocurrent can be enhanced by three processes: a decreased number of surface recombination centers[13,21] an increased efficiency of photogenerated carrier collection[12], or an increased light collection efficiency via multiple reflections and refraction effects resulting from the roughened surface. The last effect should be especially strong if the thickness of the photoetched film

is smaller than the absorption length. From the absorption coefficient of SnS_2[19], the absorption lengths at 450 nm and 550 nm are 0.3 μm and 100 μm, respectively. The etched film, used to obtain the adsorption isotherms, was roughly 10 μm thick. Therefore, the light propagation effect should be negligible at 450 nm where the band gap photocurrent becomes significant. Thus, we believe that a decreased number of recombination centers and/or an increased collection efficiency of the photogenerated carriers were the most likely contributors to the band gap photocurrent yield enhancement. We believe the major factor in increasing the band gap IPCE was the increased collection efficiency of carriers that diffused parallel to rather than perpendicular to the layers to arrive at the electrolyte interface in the channels of the photoetched structures. There will also be more carriers created in or near a space charge region because every surface exposed to the electrolyte, even deep within the sample, will produce a space charge layer.

After photoetching, the dye sensitized photocurrent yields increased relatively more than the band gap photocurrent yields. Because the quantum yield per absorbed photon was high for MB^+ sensitization before photoetching, the major limitation appeared to be light absorption by a monolayer of dye. The dye sensitization IPCE enhancement is, therefore, explained by an increased surface area produced by photoetching. The "parking garage" structure of the photoetched SnS_2 layers, Figure 4.1e, provided an increase in the van der Waals surface area for dye adsorption. Both the similar shape of the adsorption

isotherms and the heats of adsorption on photoetched and unetched surfaces (Figure 4.13 and Table 4.1) for MB^+ indicate that the dye was adsorbed on similar sites before and after photoetching. The slightly higher heat of adsorption on the PEC etched surface reflects an increase in the number of dye binding sites that have a higher dye adsorption energy.

A decrease in both the dye sensitized and the band gap IPCEs was observed for deep photoetched SnS_2 as shown in Figures 4.4, 4.5 and 4.6. The decrease occurred after a maximum in both the band gap and dye sensitized IPCEs was reached with an optimal extent of photoetching. After reaching this maximum in the IPCEs, further photoetching resulted in a lower surface area for SnS_2, which in turn resulted in lower IPCEs both for the dye-sensitization and band gap excitations. The decrease in the dye sensitized IPCE resulted from a less efficient light collection efficiency (smaller photoactive interface), while the decrease in the band gap IPCE resulted from a decreased efficiency of the photogenerated carrier collection (*vide supra*).

As shown in Figures 4.7a and b, an enhanced band gap and dye sensitized IPCE was also observed when removing the first three monolayer equivalents of SnS_2 by photoetching in 5 M NaOH. There was one exception, a slight decrease in the dye sensitized IPCE for AZB^+ on photoetched SnS_2 was observed after removing more than 1 monolayer equivalent (Figure 4.8), but the efficiency improved with further photoetching. The increase in both the dye sensitized and the band gap IPCEs is explained by a decrease in recombination centers on the

SnS_2 surface due to PEC etching. Decreasing the number of recombination centers on the semiconductor surface should yield improved photoresponses for both the band gap and dye sensitized excitations. The recombination centers may be ionized (shallow) donor impurities from near the semiconductor surface. The recombination centers are most likely not dislocations and surface steps as the SnS_2 surfaces were presumed to be atomically flat. The decreased IPCE of AZB^+ is attributed to a decrease in the number of special sites for dye adsorption. These special adsorption sites appeared to be linked to sulfur vacancies as discussed in Chapter 3. An increased surface area resulting from further photoetching compensates for this decrease in the number of special adsorption sites. Thus, the AZB^+ IPCE increased when photoetching 225 monolayer equivalents of SnS_2. The dye sensitized IPCE increased more for MB^+ (eight fold) than for AZB^+ (three fold) or CV^+ (two fold), in agreement with results from the previous chapter on unetched SnS_2.

AFM images reinforced the conclusion that the enhanced dye sensitized IPCE resulted from an increased surface area. Both the immersed and photoetched SnS_2 surfaces showed an increase in the surface roughness. Immersing SnS_2 electrodes in NaOH for approximately 5 minutes yielded an enhanced dye sensitized IPCE that was equivalent to the yield obtained on surfaces photoetching in NaOH where an equivalent of a quarter of a monolayer of SnS_2 was removed. The AFM images showed a substantial roughening of the surface was obtained when a single layer of SnS_2 was removed through

photoetching, which may be linked to the carrier concentration. A correlation between the carrier concentration and the extent of photoetching was observed when the degree of photoetching was compared to the resulting dye sensitized IPCE for SnS_2 with three different carrier concentrations. The greatest dye sensitized IPCE occurred for photoetched SnS_2 with a carrier concentration of $7.3x10^{16}$ Cl^- atoms/cm^3.

Dye Sensitization Kinetics on Photoetched Surfaces. A kinetic scheme for the dye sensitization process on a large band gap semiconductor is shown below. Some aspects of this process were shown in Figure 3.1 of the previous chapter.

$D_{ad} + h\upsilon \longrightarrow D^*_{ad}$	k_{ex}	excitation rate
$D^*_{ad} \longrightarrow D_{ad}$	$k_r + k_{nr}$	total quenching rate
$D^*_{ad} \longrightarrow D^+_{ad} + e_{surface}$	k_{inj}	injection rate
$e_{surface} \longrightarrow e_{trap}$	k_{trap}	trapping rate
$e_{trap} \longrightarrow e_{bulk}$	k_{es}	escape rate
$D^+_{ad} + e_{trap} \longrightarrow D_{ad}$	$k_{r'}$	recombination rate
$D^+_{ad} + R \longrightarrow D_{ad} + O^+$	k_{reg}	regeneration rate
$D_{ad} \longrightarrow D_{sol}$	k_{des}	dye desorption rate
$D_{sol} \longrightarrow D_{ad}$	k_{ads}	dye adsorption rate
$D^+_{ad} \longrightarrow D^+_{sol}$	$k_{des'}$	oxidized dye desorption rate

Generally, the dye molecules absorb photons (k_{ex}) and inject electrons into the semiconductor conduction band (k_{inj}). The electron may be trapped near the surface (k_{trap}) and can either be swept to the bulk (k_{es}) by the electric field in the space charge layer or recombine with oxidized dye ($k_{r'}$). Processes that compete

with the electron injection are the emissive (k_r) and radiationless decay (k_{en}) of the photoexcited dye molecules. Because several investigators have reported that k_{inj} was much faster than k_r and k_{nr} for dye sensitization of layered semiconductors, these slower processes have been neglected.[22-24]

Dye adsorption/desorption kinetics were also considered along with the processes described above because the electrode was immersed in a dye/electrolyte solution. Desorption of oxidized dye was the only process considered as there was no bulk concentration of oxidized dye. The regeneration of the photoxidized dye molecules generally occurs through the reduction by an externally added regenerating agent (k_{reg}). The oxidized dye was presumed to desorb ($k_{des'}$) and be replaced by the adsorption of unoxidized dye molecules from solution or perform an electron self-exchange reaction between the solution and adsorbed dye when the photon flux was high, the reduction was slow or the regenerating agent was either absent or at low concentration.

Photocurrent Decay. The surface concentration of the dye [D_{ad}] for MB^+ on SnS_2 was shown to be dependent on the photocurrent when the photoetched electrode was held at both a constant potential and illumination intensity. Therefore any photocurrent decay was a direct reflection of the time dependence of [D_{ad}]. This photocurrent decay may have occurred because the rate of regeneration (k_{reg}) of the photoxidized dye was slower than the excitation rate (k_{ex}). As previously mentioned, the dye sensitized photocurrent did not decay on unetched surfaces during the time of the experiment (180 sec) when

regenerator was present in solution and the light intensity was below 18 mW. The photocurrent decay on photoetched surfaces, Figure 4.14, implies that the regeneration of photoxidized dye was slower on photoetched than on unetched surfaces. Stirring the solution decreased the rate of decay by diminishing the concentration polarization of the regenerating agent. This implied that the regeneration of the photoxidized dye by H_2Q was at least partly diffusion-controlled on photoetched surfaces. This was reasonable, considering that photoetching created channels, which impeded the diffusion of H_2Q and, thereby, slowed the regeneration process for dyes adsorbed deep into the photoetched structures.

Figure 4.14 also showed a decrease in the steady-state IPCE with increasing intensity of illumination. This suggested that either the number of photoactive dye molecules decreased at high light intensities due to desorption of photoxidized dye, or there was an increase in the concentration polarization of regenerator at high light intensities. Figure 4.15 shows a compilation of data for the IPCEs of MB^+ as a function of light intensity on a photoetched surface that was immersed in a dye solution for either 5 minutes or 2 hours prior to recording the sensitized photocurrent. The MB^+ IPCE dropped considerably upon illumination with higher light intensities regardless of the immersion time. This drop in the IPCE at higher light intensities was also consistent with mass transport limitations for regenerating agent and dye in the porous photoetched structures.

CONCLUSION

The photoetching studies reported in this chapter, showed that an increased IPCE was associated with roughening the SnS_2 surface. After photoetching in either HCl or NaOH the semiconductor surfaces were covered with μm-sized pores, although the microstructure of the two surfaces are markedly different. Surface roughness was also observed with the AFM for lightly photoetched surfaces, 1.41 mC/cm^2 of charge passed. The dye sensitized photocurrent at the dye absorption maximum was dramatically increased by photoetching. The MB^+ IPCE increased from 0.35% on unetched van der Waals surfaces to over 10% on the SnS_2 surfaces photoetched with at least 1 C/cm^2. While the CV^+ IPCE increased from less than 0.01% to over 4% after photoetching with at least 1 C/cm^2. Photocurrent decay and IPCE losses at high light intensities were attributed to the concentration polarization of the regenerating agent and un-oxidized dye within the pores of the PEC etched surface. Increases in the dye sensitized IPCE were also detected when only a few monolayers of SnS_2 were photoetched. As seen in the previous chapter, MB^+ yielded the highest dye sensitized IPCE followed by AZB^+ and then CV^+ with increases that were eight fold, three fold and two fold, respectively for SnS_2 where 3 monolayer equivalents were removed via photoetching. Tin disulfide electrodes were shown to have an optimum degree of photoetching, in regards to both band gap and dye sensitization IPCEs. Furthermore, the ratio of the dye sensitization IPCE to the band gap IPCE reached a maximum at this optimal

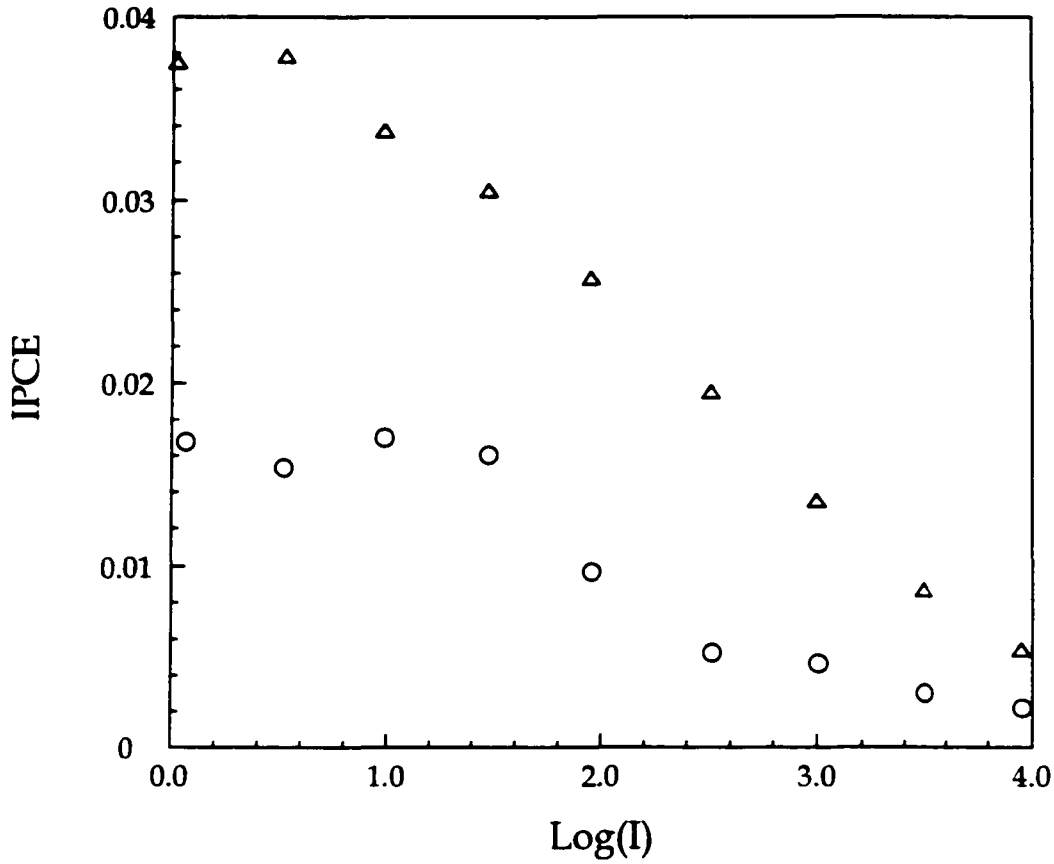

Figure 4.15. MB^+ sensitized IPCE at 689 nm (diode laser) as a function of incident light intensity. The electrode was immersed in a 15 μM MB^+ solution prior to dye sensitized photocurrent measurements. Circles represent a 5 minute immersions time and triangles a 2 hour immersion time. The photocurrent was measured after irradiating the SnS_2 surface with 689 nm light for 180 sec under the same conditions as listed in Figure 4.14. The light intensity was varied using neutral density filters. The SnS_2 electrode (8.0×10^{17} Cl^- atoms/cm^3) was etched in 1 M HCl at 1 V vs SCE with a xenon lamp and 1.5 C/cm^2 of total charge passed.

extent of photoetching. This indicated that the improved dye sensitized IPCE and band gap IPCE were affected by the phenomena; a decreased number of recombination centers and/or an increased collection efficiency of the photogenerated carriers.

The photocurrent-dye concentration dependence, which was related to the adsorption isotherm, showed Langmuir behavior on both photoetched and non-etched surfaces for MB^+ and on the photoetched surface for CV^+. The increased surface area on photoetched surfaces accounts for the MB^+ sensitized IPCE enhancement, which implies that the surface roughness factor was greater than 20. Neither MB^+ or CV^+ exhibited a shift in their λ_{max}, which indicated that the adsorption sites for these dyes were not altered by PEC etching.

PEC etching appeared to be affected by the carrier concentration. A correlation between the carrier concentration and the surface roughness was observed for lightly etched SnS_2 with AFM. There was also a correlation between the MB^+ sensitized IPCE and the extent of photoetching, which showed a dependence on the SnS_2 carrier concentration. When a similar amount of charge was passed during PEC etching, SnS_2 with $7.3x10^{16}$ Cl^- atoms/cm^3 exhibited a greater MB^+ IPCE enhancement over that on SnS_2 with carrier concentrations of $3.2x10^{16}$ Cl^- atoms/cm^3 and $3.7x10^{17}$ Cl^- atoms/cm^3. Therefore, the semiconductor properties as well as the photoetching parameters appeared to play a role in increasing the IPCE.

The work on PEC etched SnS_2 in this chapter shows that photoetching

increased the semiconductor surface area and enhanced the dye sensitized, as well as the band gap, IPCE for MB^+, CV^+ and AZB^+. In addition, the extent of PEC etching appeared to be affected by the carrier concentration. Increasing the surface area, however, was not the sole factor for the increase in the dye sensitization IPCE as the extent of the increase varied for the dyes mentioned above. There was also an increase in the binding strength of MB^+ after PEC etching. Thus, the enhanced dye sensitized IPCE was affected by more than just an increase in the surface area. It is possible that PEC etching decreases the number of recombination pathways, which could enhance the IPCEs of the dye molecules studied. Furthermore, the adsorption behavior of the dye appeared to be affected by PEC etching as evidenced by the increased binding strengths of MB^+, which may aid in enhancing the dye sensitized IPCE. Overall, PEC etching was shown to increase the dye sensitized IPCE for the organic dyes studied, the conditions for PEC etching were analyzed to improve the dye sensitization efficiency and the factors that contribute to this enhancement were studied.

SUMMARY AND FUTURE WORK

In this dissertation, the dye sensitization process for single crystal SnS_2 photoanodes was investigated for an array of organic dyes on both cleaved and PEC etched surfaces. Research on the growth of single crystal SnS_2 used in these investigations was discussed in Chapter 2. Analysis of the dye sensitization process on cleaved SnS_2 was covered in Chapter 3 and showed that both the

adsorption behavior of the dye and recombination losses affected the dye sensitization efficiency. Chapter 4 then dealt with work on PEC etched SnS_2 with considerable efforts aimed at improving the sensitization efficiencies of several organic dyes. A further discussion of the work included in these chapters follows.

The physical quality and electrical properties of the semiconductor substrate, single crystal SnS_2, used in the dye sensitization experiments of this dissertation were investigated in Chapter 2. The growth of single crystal SnS_2 with various carrier concentrations and different dopant elements has been accomplished. The ability to accurately characterize the electronic properties of the single crystal SnS_2 has also been established through Hall and Mott-Schottky measurements. The carrier concentration was shown to be uniform throughout the middle section of the SnS_2 single crystals. Analysis of the photocurrent data revealed that a direct correlation exists between the carrier concentration, the minority carrier concentration and the band-gap IPCE, which was in agreement with theoretical principles of semiconductor physics.

Investigation of the dye sensitization process on cleaved SnS_2 in Chapter 3 included the measurement of an adsorption isotherm. This work showed that MB^+ exhibited Langmuir type adsorption behavior. Analysis of the Langmuir type adsorption isotherm yielded a reasonable value for the area occupied by an individual dye molecule and predicted the formation of monolayer surface coverage on freshly cleaved SnS_2. Dyes appeared to be in a "flat" orientation with respect to the semiconductor surface and exhibited weak van der Waals

interactions as determined from the heat of adsorption calculations. However, the adsorption isotherm data may require reanalysis under the auspices of dye-island formation.

Further work in Chapter 3 on the dye sensitization process dealt with the adsorption behavior of dyes and involved studies of photoxidation and dye sensitization efficiencies for SnS_2 with carrier concentrations ranging from $1x10^{16}$ - $1x10^{18}$ cm^{-3} Cl^-. Photoxidation studies with MB^+ and CV^+ showed that these dyes exhibited both different excited state properties and distinct adsorption behavior with CV^+ displaying significantly faster rates of adsorption and desorption. It was also shown that the regeneration of photoxidized dye molecules (MB^+ and CV^+) on the SnS_2 surface occurred through either electron self exchange or the adsorption/desorption process when reduction by an externally added regenerating agent was not done. Analysis of the dye sensitization efficiencies for MB^+, AZB^+, CV^+ and OX^+ showed that IPCE values for these dyes were unaffected by the SnS_2 carrier concentration. However, the photoaction spectra showed that MB^+ had the greatest IPCE, followed by AZB^+ and then CV^+ and/or OX^+. In addition, MB^+ and AZB^+ have similar oxidation potentials and reduction potentials that are more negative than the conduction band edge, but the IPCE of MB^+ is greater than that of AZB^+. This was explained by recombination loses and different adsorption behavior due to special binding sites or the formation of three-dimensional dye islands. An additional dye characteristic, that may affect the dye sensitization process, is the higher quantum yield for triplet state

formation by MB^+ and AZB^+ compared to OX^+ and CV^+.[25-27]

Recombination also appeared to influence the dye sensitization process as determined through quantum measurements from both photoaction spectra and photocurrent-voltage curves. The identity of the recombination centers was probed by thiol addition and trying to change the S content of the SnS_2 surface by annealing in S vapor as presented in Chapter 3. Photoaction spectra showed that the dye sensitization efficiencies of MB^+, AZB^+, CV^+ and OX^+ were affected by recombination, as mentioned previously. In addition, impedance measurements revealed that the flat band potential shifted to more positive potentials upon adsorption of H_2Q and MB^+, which may affect the driving force for recombination. Photocurrent voltage curves for MB^+ and CV^+ also demonstrated that while a positive driving force may be necessary for electron injection the magnitude of this driving force did not appear to affect the dye efficiency. These results were in agreement with the femtosecond electron injection rates[23,24] into the SnS_2 conduction band measured for OX^+, which indicated that this step in the dye sensitization process was not limiting the overall dye sensitization efficiency. The photocurrent voltage curves also showed a slow rise with increasingly positive applied potential that is indicative of a competition between electron escape and recombination. Work by Miller supports these results as the electron escape process would have to be extremely fast to compete with the injection[24] and recombination rates[28] reported for OX^+. Furthermore, enhanced dye sensitized IPCEs from annealing were attributed to a decrease in the number of

traps that are pathways for recombination. These defect sites or vacancies that influence the recombination losses and, thus, the dye sensitized IPCE, may be sulfur sites adjacent to the surface as both thiol addition and variations in the carrier concentration did not greatly influence the dye efficiency, while annealing SnS_2 samples did.

Chapter 4 focused on photoetching studies and showed that an increased IPCE was associated with roughening the SnS_2 surface. This was observed even for lightly photoetched surfaces, with less than 1.41 mC/cm^2 of charge passed. Photoetched SnS_2, with > 1 C/cm^2 of charge passed, exhibited similar trends compared to unetched SnS_2 with MB^+ having a greater dye sensitization efficiency than CV^+. In the light etching studies, where AZB^+ was used, the trend continued with MB^+ yielding the greatest IPCE, followed by AZB^+ and then CV^+. Increasing the surface area, however, was not the sole factor for the increase in the dye sensitization IPCE as the extent of the increase varied for the dyes mentioned above.

Adsorption isotherms for MB^+ and CV^+ showed Langmuir behavior on photoetched SnS_2 surfaces. PEC etching did not appear to affect the adsorption sites for either MB^+ or CV^+. The MB^+ IPCE enhancement from PEC etching correlated to a surface roughness factor of greater than 20. Further analysis of the MB^+ adsorption isotherms indicated that PEC etching influences the binding strength of the dye as the heat of adsorption was slightly greater for MB^+ on photoetched versus unetched SnS_2.

An optimum degree of photoetching for SnS_2 electrodes was observed in regards to the dye sensitized IPCE, the band gap IPCE and their ratio as reported in Chapter 4. This indicated that the improved dye sensitized IPCE and band gap IPCE were affected by the same phenomena; a decreased number of recombination centers and/or an increased collection efficiency of the photogenerated carriers. In addition, the relationship between the MB^+ sensitized IPCE and the extent of photoetching showed a dependence on the SnS_2 carrier concentration. A correlation between the SnS_2 carrier concentration and the surface roughness was also observed with AFM. Overall, PEC etching was shown to increase the dye sensitized IPCE for the organic dyes studied, the conditions for PEC etching were analyzed to improve the dye sensitization efficiency and the factors that contribute to this enhancement were studied.

Future studies should include an analysis of dye surface morphology with AFM, further work on the dye surface coverage, determination of the charge injection rates of MB^+ and AZB^+ and an investigation of SnS_2 surface states. A more in-depth discussion of the proposed future studies follows.

Dye Surface Morphology. The dye surface morphology on SnS_2 should be studied in air with atomic force microscopy (AFM) and correlated with the dye photoresponse for the same sample. These studies should provide additional information on the surface coverage obtained on SnS_2 with adsorbed organic dyes. Similar studies by Parkinson[29] showed that squaraine dyes on SnS_2 form two distinct morphologies of dye aggregates that yielded different

photoresponses and appeared to be the result of the specific intramolecular interactions of the dye aggregates. Two adsorption methods were used in order to obtain the different dye aggregate morphologies; soaking the SnS_2 electrode or applying a drop of solution to the SnS_2 electrode and allowing the solvent to evaporate.

These studies should focus on the four organic dyes highlighted in Chapter 3; MB^+, CV^+, AZB^+ and OX^+. The AFM experiments should be carried out as described in the paper by Parkinson[29]. It should be possible to image both MB^+ and OX^+ adsorbed on SnS_2 with the AFM as both dyes are known to adhere to the SnS_2 surface when removed from solution as evidenced from the UV-Vis spectra measured in air on dry SnS_2 in Chapter 3. It is presumed that AZB^+ will also adhere to the surface, being a acridine dye with a similar structure to both MB^+ and OX^+. The fast adsorption and desorption rates for CV^+ make it less viable for AFM studies; UV-Vis absorption spectra on dry SnS_2 were not measurable for this dye on as reported in Chapter 3. Results with CV^+ might be obtained if a cold bath was utilized when soaking the SnS_2 sample in the dye solution in order to decrease the rate of desorption. The procedure for soaking the electrodes should follow that used for the UV-Vis adsorption spectra measurements in Chapter 3. For the drop technique, the same solution used for the soaking method should be applied to a freshly cleaved piece of SnS_2. The size of the drop should be such that an equivalent of one monolayer is administered. Photoaction spectra can also be obtained for the samples following the procedure

detailed in the paper by Parkinson[29]. Unlike the squaraine dyes used by Parkinson[29], the organic dyes (MB^+, AZB^+, OX^+ and CV^+) are soluble water so instead a insoluble solvent such as tetraethylammonium perchlorate (THF), dichloromethane or chloroform should be used with a suitable electrolyte such as tetrabutyl ammonium hexafluorophosphate ($TBAPF_6$). Results from these studies may aid in determining whether monolayer coverage or dye-islands are formed on the SnS_2 surface. Information about the intermolecular interactions that affect this system may also be determined.

Dye Surface Coverage. Information on the dye surface coverage may also be ascertained from studies with a photoelectrochemical quartz crystal microbalance (PEQCM). This technique can be used to directly measure the amount of dye adsorbed on a SnS_2 surface. If simultaneous photoaction measurements can be made, direct correlation between dye adsorption and dye sensitization should be possible. These studies should allow us to determine if the photoelectrochemical response and the number of adsorbed dye molecules reach a plateau at the same dye solution concentration. Using this technique to measure the MB^+ adsorption isotherm as a function of the dye solution concentration should confirm or refute the results in Chapter 3. This technique would also allow an adsorption isotherm to be measured for CV^+ on cleaved SnS_2. These studies, along with the results from the surface morphology section above, would enhance the understanding of dye adsorption and may determine whether dyes adsorb on the SnS_2 surface forming monolayer coverage or as 3-D dye

islands.

Quartz crystal microbalances are mass sensitive detectors based on an oscillating quartz wafer. A typical QCM consists of a quartz crystal with two gold electrodes evaporated on opposite sides of the wafer. The two electrodes are used to induce an oscillating electric field normal to the surface of the quartz wafer. The oscillation frequency of the wafer is then affected by interfacial mass changes. The change in frequency can be measured and used to calculate the mass change at the QCM surface.[30]

PEQCM measurements can be made by contacting a thin section of single crystal SnS_2 to one of the evaporated Au electrodes. Electrical contact are fabricated by evaporating Au on the backside of the SnS_2 crystal. This crystal is then mounted on one of the Au electrodes of the quartz wafer and held in place with a nonreactive polymer. The polymer covers the SnS_2 edges so only the surface of the crystal is exposed to solution. The modified quartz wafer is then clamped between two O-rings. This ensemble is placed in an electrochemical cell with an optical window for photoexcitation of adsorbed dye. Only the side of the quartz wafer with SnS_2 will be exposed to solution. Dye solutions of increasing concentration will be pumped into the cell, the mass change measured and then a photoaction spectra recorded.

Dynamics of Electron Injection by Infrared Transient Absorption. Charge injection rates for both OX^+ and CV^+ sensitized SnS_2 have been measured via time resolved fluorescence. Comparable measurements for MB^+ and AZB^+ have not

been attempted as these dyes do not fluoresce. Infrared transient absorption experiments can determine the charge injection rates of these two dyes on SnS_2. Because the IPCEs for both MB^+ and AZB^+ are significantly higher than for OX^+ and CV^+ these results will aid in discerning the differences between these dyes. Hopefully this will lead to the ability to design a more efficient dyes sensitization system.

These experiments would use femtosecond pump-probe spectroscopy to time resolve the injection of electron into SnS_2 following photoexcitation of the adsorbed dye. This can be accomplished by pumping the dye sensitized SnS_2 at the absorption maximum of the dye and probing the absorption by monitoring the injected electrons in the SnS_2 conduction band at 1-10 μm.[31] The results should be compared to an insulating substrate such as Al_2O_3.

Surface State Investigations with Ultraviolet Photoelectron Spectroscopy (UPS). The role of surface states in the dye sensitized SnS_2 system is as yet unknown. On smooth single crystal SnS_2 surfaces, which should be virtually defect free, the IPCE is low. Miller et al. measured the lifetime of electrons injected into the conduction band of SnS_2. A lifetime of ≤ 60 fs was reported for electrons in the conduction band. Because the back reaction has an upper limit of 10 ps the electron may be trapped in a surface state prior to geminate recombination.

Photoelectrochemical etching increases the IPCEs and was thought to generate surface states that might increase dye adsorption as well as trap injected

electrons and thus compete with the back electron transfer. It was recently reported by Tenne[32] that photoelectrochemical etching decreased the number of surface states. However, these studies were focused on II-VI semiconductor electrodes where the photoelectrochemical etching produced very ordered surface structures unlike those seen on SnS_2.

Further work in this area can be accomplished with UPS measurements. Because X-ray Photoelectron Spectroscopy (XPS) measurements have already been accomplished, only a monochromatic vacuum ultraviolet radiation source is required for UPS. Because UPS utilizes lower energy radiation the outer or valence electrons rather than core electrons are ejected. Thus, UPS provides information about chemical bonds between elements as well as surface states.[33] These measurements can analyze the effects of etching and the role of surface states in process of dye sensitization.

REFERENCES

1 O'Regan, B. and Grätzel, M. *Nature* **353,** 737 (1991).

2 O'Regan, B.; Moser, J.; Anderson, M. and Grätzel, M. *J. Phys. Chem.* **94,** 8720 (1990).

3 Vlachopoulos, N.; Liska, P.; McEvoy, A. and Grätzel, M. *Surf. Sci.* **189/190,** 1216 (1987).

4 Vlachopoulos, N.; Liska, P.; Augustynski, J. and Grätzel, M. *J. Am. Chem. Soc.* **110,** 1216 (1988).

5 Parkinson, B. A. *Langmuir* **4,** 967 (1988).

6 Parkinson, B. A., In *Electrochem. Soc. Proc.* **160** 88 (1988).

7 Spitler, M. and Parkinson, B. A. *Langmuir* **2,** 549 (1986).

8 Jakubowics, A.; Mahalu, D.; Wolf, M.; Wold, A. and Tenne, R. *Phys. Rev. B* **40,** 2992 (1989).

9 Ryan, M. A.; Levy-Clement, C.; Mahalu, D. and Tenne, R. *Ber. Bunsenges. Phys. Chem.* **94,** 671 (1990).

10 Margulis, L.; Mahalu, D.; Watkins, E. and Tenne, R. *Microscopy of Semiconducting Materials 1991* **117,** 767 (1991).

11 Margulis, L.; Mahalu, D.; Parkinson, B. and Tenne, R. *Scanning Microscopy* **5,** 953 (1991).

12 Nabutovsky, V. M.; Eherman, K. and Tenne, R. *J. Appl. Phys.* **73,** 2866 (1993).

13 Mahalu, D.; Jakubowicz, A.; Wold, A. and Tenne, R. *Phys. Rev. B* **38,** 1533 (1988).

14 Mahalu, D.; Margulis, L.; Wold, A. and Tenne, R. *Phys. Rev. B Cond. Matt.* **45,** 1943 (1992).

15 Tenne, R.; Marcu, V. and Prior, Y. *Appl. Phys. A* **37,** 205 (1985).

16 Katty, A.; Fotouhi, B. and Gorochov, O. *J. Electrochem. Soc.* **131,** 2806 (1984).

17 Fotouhi, B.; Katty, A. and Gorochov, O. *J. Electrochem. Soc.* **132,** 2181 (1985).

18 Fotouhi, B. and Katty, A. *Electrochimica Acta* **31,** 795 (1986).

19 Domingo, G.; Itoga, R. S. and Kannewurf, C. R. *Phys. Rev.* **143,** 536 (1966).

20 Adamson, A. W. *Physical Chemistry of Surfaces,* 5th ed. (John Wiley & Sons, Inc., New York, 1990).

21 Tenne, R. and Wold, A. *Appl. Phys. Lett.* **47,** 707 (1985).

22 Eichberger, R. and Willig, F. *Chem. Phys.* **141,** 159 (1990).

23 Willig, F.; Eichberger, R.; Sundaresan, N. S. and Parkinson, B. A. *J. Am. Chem. Soc.* **112,** 2702 (1990).

24 Lanzafame, J. M.; Miller, R. J. D.; Muenter, A. A. and Parkinson, B. A. *J. Phys. Chem.* **96,** 2820 (1992).

25 Asimov, M. M.; Gavrilenko, V. N. and Rubinov, A. N. *J. of Luminescence* **46,** 243 (1990).

26 Danziger, R. M.; Bar-Eli, K. H. and Weiss, K. *J. Phys. Chem.* **71,** 2633 (1967).

27 Kreller, D. I. and Kamat, P. V. *J. Phys. Chem.* **95,** 4406 (1991).

28 Xu, S.; Miller, C. C.; Dol, S. J.; Gao, Y.; Mantell, D. A.; Mason, M. G.; Muenter, A. A.; Sharp, L. I.; Parkinson, B. A. and MIller, R. J. D. *Chem. Phys. Lett.* **272,** 209 (1997).

29 Takeda, N. and Parkinson, B. A. *Electrochimica Acta* **45,** 4559 (2000).

30 Buttry, D. A. and Deakin, M. R. *An. Chem.* **61,** 1147A (1989).

31 Ellingson, R. J.; Asbury, J. B.; Ferrere, S.; Ghosh, H. N.; Sprague, J. R.; Lian, T. and Nozik, A. *J. Phys. Chem. B* **102,** 6455 (1998).

32 Tenne, R., In *Semiconductor Micromachining, Volume 1. Fundamental Electrochemistry and Physics,* Vol. 1, Campbell, S. A. and Lewerenz, H. J., Eds. (John Wiley & Sons Ltd., New York, 1998).

33 Hüfner, S. *Photoelectron Spectroscopy* Cardona, M., Fulde, P., and Queisser,

H.-J., Eds., Solid State Sciences (Springer-Verlag, Berlin, 1996).